EPSC2018

TP7/SB20 abstracts

13 Sep 2018 15:36:18

EPSC Abstracts
Vol. 12, EPSC2018-8, 2018
European Planetary Science Congress 2018

Regolith mixing by impacts: Lateral diffusion of basin melt

Tiantian. Liu (1,2), Greg. Michael (2), Juliane Engelmann (2,3), Kai Wünneman (2,3) and Jürgen Oberst (1,4)
(1) Institute of Geodesy and Geoinformation Science, Technical University Berlin, 10623 Berlin, Germany (tiantian.liu@tu-berlin.de), (2) Planetary Sciences and Remote Sensing, Freie Universitaet Berlin, Malteser Strasse 74-100, 12249 Berlin, Germany, (3) Museum für Naturkunde, Leibniz Institute for Evolution and Biodiversity Science, 10115 Berlin, Germany, (4) Institute of Planetary Research, German Aerospace Center (DLR), 12489 Berlin, Germany.

1. Introduction

Impact cratering has been the primary process to alter the distribution of lunar highland materials since the formation of a crust. The impact history is recorded in the radiogenic clocks of produced impact melt which are accessible to study in lunar samples. However, emplaced impact melt is exposed to a long-time gardening process (i.e. re-melting, excavation, burial, and re-excavation) by the subsequent impacts resulting in a complex spatial distribution. To investigate the diffusion behavior of impact melt, a model tracing the evolving distribution of melt laterally and by depth within a narrow band is built by means of a Monte Carlo approach. The lateral melt diffusion for three mid- to late-forming basins (Serenitatis, Crisium, and Imbrium) are obtained based on the model.

2. Method

A band passing along the great circle is chosen for modelling. By dividing the band into cells, the ejecta volume and the portion of unheated and melted materials are recorded laterally and by depth, tracking the age of the newly-generated impact melt with progressing model time, *t*. There are three key aspects when modelling:

Distribution of impact events: A minimum (D_{min}) and maximum (D_{max}) crater diameter, is chosen as 5 and 300 km, respectively. By using the Monte Carlo method, the diameter of craters, *D*, is generated, the size-frequency distribution of which statistically conforms to the standard production function (PF) larger than D_{min} [1]. The corresponding impact centre of each event is randomly distributed along the great circle. The average time to the next impact event larger than D_{min} in diameter, that is impact rate, is calculated from the chronology function (CF) [2], PF, and *t* [3].

Excavating and melting processes: The excavation depth for each simulated crater, d_{exc}, is $D_t/10$, where D_t is the diameter of the transient crater [4]. D_t is related to *D* as follows: for simple craters, $D_t = 0.8D$ [4]; for complex craters, $D_t = (D D_Q^{0.13}/1.17)^{1/1.13}$ [5], where D_Q is the simple-complex transition diameter, and taken as 21 km [6]. The corresponding volume of the excavated materials, V_{exc}, having a torus-like shape is estimated to be 1/3 of a disc with d_{exc} in thickness and D_t in diameter. For the conservation of mass, the excavation unit is assumed to be a cuboid with 1/3 D_t in length and d_{exc} in thickness located at the crater centre. The volume of each penetrated layer is diminished. The total volume of the generated impact melt with a reset age as *t* is: $V_{melt} = cD_t^d$, where c and d are taken as 1.4×10^{-4} and 3.85, respectively [7].

Distribution of melt materials: The distribution of impact melt has not been well quantified [8, 9]. Recently, the relationship between the melt proportion in ejecta and the distance from crater center was found by the means of numerical modelling using the iSALE shock-physics code [10]. It was found that ~75% of the generated impact melt stays within the crater and the remainder is ejected. About 85% of the ejected materials are deposited within five radii from crater centre (consists of an ejecta blanket and a transition to a patchy ejecta zone). We assume that ejecta material in patchy transition zones is also continually distributed with thin thickness. Only the melt within five radii from the crater center is therefore traced. In addition, it showed that melt fraction is linearly increasing with distance from impact center. By assuming a continual distribution of melt in ejecta as a layer, the thickness of impact melt, δ_m, was obtained: $\delta_m(r) = A_m r^{-2}$. A_m is recalculated for craters with different size. To conserve V_{melt}, the integrated melt volume within five radii is taken to be exactly 25% of V_{exc}. The thickness of ejecta layer decreases with distance from crater centre, *r*: $\delta(r) = Ar^{-3}$ [4], where A is varied for the craters with different *D* to conserve mass similar as A_m described above.

To conserve the mass, we take instead that all the excavated materials on the band are transported along the great circle instead of spread radially. It may be considered as compensating the ejecta produced by

craters outside the band that the model does not record.

3. Results

The generated impact melt is depleted by re-melting, spread to more distant locations by excavation, and buried by the overlaying ejecta of subsequent impacts.

The great circle through the mid- to late-forming Imbrium, Crisium, and Serenitatis basin is chosen to investigate the lateral diffusion of melt from the giant basin-forming events. The plausible ages for the three basins are calculated to be 4.13, 4.09, and 3.88 Ga, respectively, based on N20 [11]. The present-day distribution of impact melt by depth for three basins (Figure 1) shows that the initially generated melt is destroyed and redistributed by the subsequent impact events: the older the basin, the less the remaining melt. In addition, the ejecta materials from both Crisium and Imbrium basin cover the Serenitatis melt burying it to the greater depth. Some of the buried melt was re-excavated to shallow layers subjecting to the further gardening. Furthermore, it shows that the local gardening by the lesser-scaled impact events after the formation of basins strongly mixed the basin melt in the near-surface resulting in an irregular distribution which has significant consequence for scooped samples at the landing sites

The quantitative abundance of basin melt at Apollo-Luna sampling sites is estimated and compared with the radiometric datings (Figure 2). For the relatively young Imbrium and Crisium melt, the simulated results are consistent with the radiometric datings. The older Serenitatis melt at the near-surface is strongly dependent on the subsequent impact events. Its content is only statistically predictable at specific sites.

4. Discussions and Conclusions

In spite of the high impact flux, the lateral transportation efficiency of impact melt by impact gardening is not high as expected. The great volume of melt generated by the giant basin-forming events survives until the present day, which is consistent with the radiometric datings from highland samples. If the estimated basin age is close to the true value, it thus supports the nearby basin origin explanation for the grouped isotopic datings around 3.9–4.0 Ga of Apollo-Luna highlands samples rather than the cataclysm scenario. Understanding the diffusion of impact melt is helpful for interpretation of radiometric dating of lunar samples and may predict likely findings of differently-aged melt in future sampling work like the Chinese Change'E-4 (CE-4).

Acknowledge: The work was supported by the German Research Foundation (DFG) SFB TRR-170-1 TP A4.

References: [1] Michael G. et al. (2016) Icarus, 277, 279–285. [2] Neukum G. (1983) Univ. of Munich, 1–186. [3] Michael G. et al. (2017) Icarus, 302, 80–103. [4] Melosh H. (1989) Oxford Univ. [5] McKinnon W. et al. (1997) Venus II: Geology, Geophysics, Atmosphere, and Solar Wind Environment, 969. [6] Pike R. (1977) LPSC, 8, 3427–3436. [7] Cintala M. and Grieve R. (1998) MPS, 33(4), 889–912. [8] Stöffler D. et al. (1975) JGR, 80(29), 4062–4077. [9] Wünnemann K. et al. (2016) MPS, 51(10), 1762–1794. [10] Wünnemann K. et al. (2006), Icarus, 180(2), 514–527. [11] Fassett C.I. et al. (2012) JGR: Planet, 117(2), 1–12.

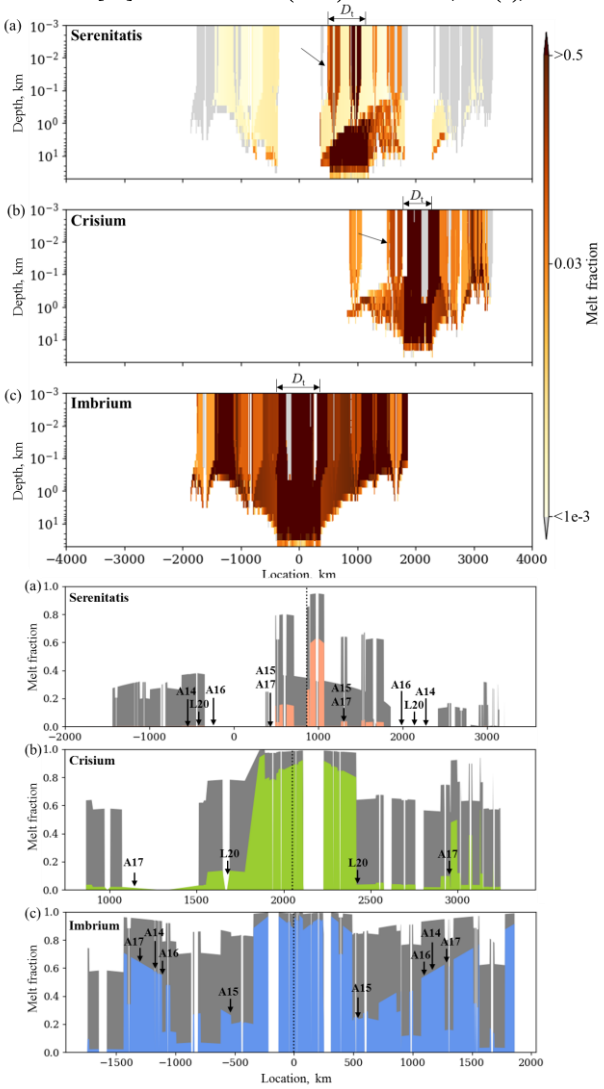

Figure 1 (up). Present-day distribution of the melt from Serenitatis (a), Crisium (b), and Imbrium (c) basin. Figure 2 (down) Average fraction of melt from Serenitatis (a), Crisium (b), and Imbrium (c) basin in the top 0.1 m.

EPSC Abstracts
Vol. 12, EPSC2018-96, 2018
European Planetary Science Congress 2018

Experimental Investigation of the Formation of Complex Craters

E. Martellato (1), K. Wünnemann (1,2), M.A. Dörfler (3), B. Schuster (3), and T. Kenkmann (3)
(1) Museum für Naturkunde, Leibniz Institute for Evolution and Biodiversity Science, Berlin, Germany, (2) Institute of Geological Sciences, Freie Universität, Berlin, Germany, (3) Institute of Earth and Environmental Sciences, Geology, Albert-Ludwigs-University Freiburg, Germany (email: elena.martellato@mfn.berlin)

Abstract

Complex crater formation is a poorly understood mechanism because standard material models fail to explain the gravity-driven collapse at the observed size-range of a bowl-shaped transient crater into a flat-floored crater structure with a central peak or ring and terraced rim. One of the suggested mechanisms, the Acoustic Fluidization (AF) model [1], assumes that heavily fractured rocks surrounding the transient crater are temporarily softened by an acoustic field in the wake of an expanding shock wave generated upon impact. The AF has been successfully employed in a number of studies of complex crater formation [2, 3], however, there is no clear relationship between model parameters and observables. In this study, we present results of laboratory experiments aiming at relating the AF parameters to observables such as the grain size, average wave length of the acoustic field and its decay time τ relative to the crater formation time.

1. Introduction

A hypervelocity impact [4] relies on the collision of a cosmic body with a planetary surface. The initial cavity resulting from shock-induced excavation flow (the so-called transient crater) is unstable in the given gravity field and undergoes modification. The subsequent collapse depends on the gravity field and target properties such as strength, composition, and layering, in addition to the crater size. When the crater diameter is larger than some critical threshold diameter D_{sc} characteristic of a planet (e.g., D_{sc}~15 km on the Moon), the transient cavity undergoes a distinct modification process, which includes uplift of the crater floor and underlying strata to form central peaks or peak rings, and failure of the rim into wide zones of stepped terraces. Such a collapse requires a stress field in excess of the failure strength of rocks to allow for plastic material flow.

1.1 Acoustic Fluidization

One current model invoked to explain such a collapse is the so-called Acoustic Fluidization (AF) model [1]. It is based on the assumption that the target is heavily fractured and described by a time-varying Bingham fluid. The system of rock debris (constant block size) is excited by acoustic waves in the wake of an expanding shock wave generated upon impact. The overburden pressure in heavily fractured material at some depth in the vicinity of the crater fluctuates due to the high-pressure amplitude, high-frequency, random acoustic waves. In the phase of temporary relieve of the overburden pressure, the frictional resistance between fragments is reduced so that the fragments may easily shear against one another. The Block Model (BM) [5] is a simplification of AF model that has been implemented in the iSALE shock physics code (http://www.isale-code.de). BM is described by two parameters: the kinematic viscosity of the fluidized region η, and the decay time of the block vibrations τ [5]. Theory suggests that both the viscosity η and the decay time τ are functions of the density ρ, block size h of the fragmented sub-crater rock mass, and period T of the block oscillation. In turn it has been suggested [5] that the block length parameter h can be scaled by a quantity describing the transient cavity depth.

This study aims at a better understanding of the mechanics of complex crater formation, by coupling the BM parameters in relation to observables. Here, we present preliminary results of a series of analogue laboratory experiments, where we tested the material properties of acoustically excited granular targets, and the development of the complex morphology.

2. Method

The fluidization of the target was induced by an external artificial source, since the natural generation of acoustic noise behind the shock wave is not

possible at small scales, where the fluidization time is short relative to the time of crater collapse. Two different devices were adopted to test material fluidization. In the first experimental setup (at the Institut für Geo- und Umweltnaturwissenschaften, Albert-Ludwigs-Universität Freiburg), the device was a subwoofer coupled to the bottom of the target, see also [6]. The target was a box of fine-grained material placed on top of two supports. Part of the setup was: (i) a 6.35 *mm* spring-driven air gun mounted perpendicular to the target surface accelerating plastic (density=1.4 g/cm^3) projectiles to velocities as high as 180.4±3.73 *m/s*; (ii) headlights, and (iii) two LaVision Imager sCMOS cameras.

In the second experimental setup (at the Museum für Naturkunde Berlin), the external device was an electro dynamical exciter for stimulating bending waves on plates and was attached to the bottom of the target. The target was cylinder of fine-grained material, which was suspended and attached to a tripod through a system of springs. This system was designed in order to increase the number of degree of freedom of the material movement caused by the external source. A viscosimeter (rotational viscosimeter PCE-RVI 2, V1-R) was used to measure the variation of the viscosity as a function of frequency and amplitude.

3. Results

In the first setup configuration, we conducted a number of shots while varying the target grain size (~100-800 μm), and the frequency of the acoustic wave (50-500 *Hz*). The wavelength of the external acoustic wave is modulated to match the size of the particles. Particle displacements and strain of the collapse are analysed through the Matlab tool "PIVlab" [7, 8, 9]. Figure 1 shows a cross section of the final stage of crater formation of a shot on a quarter space setup geometry, where the target is composed of glass beads (150-250 μm).

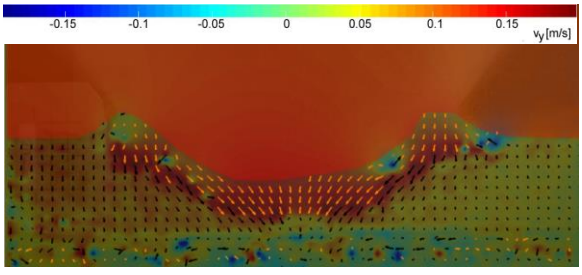

Figure 1: Particle displacement analysis for the shot of a plastic 6.35 *mm* projectile into a 150-250 μm glass beads target fluidized with frequency of 100 *Hz*.

In the second setup configuration, we performed a systematic measurement of the target material viscosity, varying systematically and independently frequency (Figure 2) and amplitude of the induced acoustic field, as well as the fine-grained material type (quartzsand: 100-500 μm; glass beads: 90-150 μm). The viscosity is the average of 5 minutes of acquisition. The curve trends of the two target materials have a minimum at ~ 60-100 *Hz*.

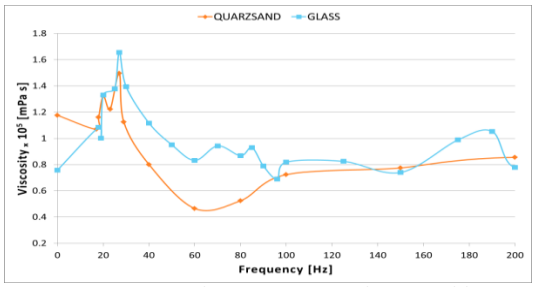

Figure 2: Comparison of the viscosity as a function of frequency of the external source, for quartzsand and glass beads. An amplitude of 2.3 V was used for the systematic frequency variation.

4. Summary and Conclusions

We observe that the highest fluidization of the target material is achieved for low frequencies (100-200 *Hz*) in both experimental setups. The frequency range is in accordance with [6]. They found that 80 *Hz* was the most effective frequency in fluidizing glass target material. So far, no central peak was observed in shot experiments. The next shot campaign will be carried out with the second experimental setup.

Acknowledgements

This project has received funding from the European Union's Horizon 2020 research and innovation programme under the Marie Skłodowska-Curie grant agreement No 709122.

References

[1] Melosh, H.J.: Journal of Geophysical Research, Vol. 84, pp. 7513-7520, 1979.

[2] Bray, V.J. et al.: Meteoritics & Planetary Science, Vol. 43, pp. 1979-1992, 2008.

[3] Collins, G.S. et al.: Meteoritics & Planetary Science, Vol. 43, pp. 1955-1977, 2008.

[4] Melosh, H.J.: Impact Cratering: a geological process, Oxford Univ., 1989.

[5] Wünnemann, K. and Ivanov, B.A.: Planetary and Space Science, Vol. 51, pp. 831-845, 2003.

[6] Dörfler, M. and Kenkmann, T. 49th LPSC, abstract #1484, 2018.

[7] Thielicke, W. and Stamhuis, E.J.: Journal of Open Research Software, Vol. 2, pp. e3, 2014.

[8] Thielicke W. and Stamhuis EJ.: PIVlab-Time-Resolved Digital Particle Image Velocimetry Tool for MATLAB, Figshare, 2014.

[9] Thielicke, W.: The Flapping Flight of Birds - Analysis and Application. PhD Thesis, 2014.

EPSC Abstracts
Vol. 12, EPSC2018-102-9, 2018
European Planetary Science Congress 2018

Misleading projectile determination by Cr/Ni and Ni/Co ratios of Australasian microtektites and impact melt rocks

Gerhard Schmidt
Institute of Earth Science, Ruprecht-Karls-University Heidelberg, Germany (gerhard.schmidt@geow.uni-heidelberg.de)

Abstract

The identification of meteoritic material in melt rocks from impact craters needs significantly elevated abundances of elements depleted in the Earth's crust and enriched in meteorites. Inter-element ratios of Ni, Co, Cr, and Au are not reliable and misleading for projectile identification in terrestrial impactites. The reasons are (1) high abundances in the Earth crust and (2) mobilisation by secondary processes. The refractory highly siderophile elements Os, Ru, Ir, and Rh (PGE) are abundant in most meteorites but depleted in crustal rocks, less mobile and therefore most reliable elements for projectile identification. Magmatic iron projectiles can be distinguished from non-magmatic iron meteorites by their subchondritic Os/Ir and suprachondritic Ru/Ir ratios (e.g. Sääksjärvi in Finland and Rochechouart in France).

1. Introduction

Approximately 190 impact craters are currently known on Earth. Impact melt rocks are potential carriers of meteoritic material. About 20 iron meteorites and 20 chondrites have been identified as projectiles. The nature of the impactor and the location that generated the Australasian tektite/microtektite strewn field (~15% of the Earth's surface) is unknown [1].

2. Projectile identification

2.1 Australasian tektite strewn field

Recently, an ordinary chondritic impactor signature in Australasian microtektites have been proposed based on variations of Ni, Co and Cr inter-element ratios with concentrations of 680, 50, and up to ~370 µg/g, respectively [2]. High Ni, Co and Cr contents in Australasian microtektites were explained by up to ~5% chondritic impactor contamination [2] corresponding to about 20 ng/g of the refractory siderophile element Ir. However, the Indonesian tektite with high Ni and Cr abundances of 428 and 311 µg/g, respectively, show enrichments of about 4 ng/g Ir [3]. A chondritic impactor contribution appears to be inconsistent with observed Ni, Co, and Cr inter-element ratios. Incidentally, the Ni/Co ratios of chondrites and iron meteorites overlap and are not reliable for projectile identification. In contradiction, the Ni-rich tektite sample exhibit broadly chondrite-relative PGE proportions, although Ru/Ir is about 10% lower [3]. Non-chondritic PGE abundances in tektites with enrichments of Rh were explained by incorporation of IC iron meteorites as impactor [4].

2.2 Sääksjärvi (Finland)

The 5 km diameter impact crater in Finland is most likely formed by a magmatic iron meteorite, based on subchondritic Os/Ir and suprachondritic Ru/Ir ratios [5]. However, detected Cr/Ni, Ni/Co and Cr/Co ratios of the melt samples are much higher than those from iron meteorites with very low Cr/Ni <<0.1 and Cr/Co << 0.1 inconsistent with an iron meteoritic projectile.

2.3 Popigai (Siberia)

Concentrations of 98 µg/g for Ni, 26 µg/g for Co, 105 µg/g for Cr, and about 1 ng/g for Ir were measured in impact melt samples from the ~ 100 km diameter Popigai impact crater in Siberia [6]. The observed Cr, Ni and Co inter-element ratios do not support a chondrite as projectile type. At least 75% Cr and ~90% Co have to be subtracted as indigenous contribution to get chondritic Cr/Ni and Cr/Co ratios, an unrealistic scenario. Around 0.2 wt.% meteoritic contamination have been identified in homogeneous impact melt samples based on PGE concentrations (except Os) [6]. An L-chondrite was identified as the most likely Popigai impactor.

2.4 Morokweng (South Africa)

Ni, Co, Cr, and Ir are enriched in melt rock samples from the 70–80 km diameter Morokweng impact structure with average values of 780 µg/g for Ni, 50 µg/g for Co, 440 µg/g for Cr, and 32 ng/g for Ir [7]. However, a chondritic impactor contribution appears

to be inconsistent with observed Ni, Co and Cr inter-element ratios. Chromium isotope data have shown that about half of the chromium in the melt rocks is of extraterrestrial origin and consistant with an ordinary chondritic source [8]. Chondrite-normalized PGE abundance pattern of the impact melt rocks are flat and indicate the presence of about 2 to 5 wt% of a chondritic projectile component [7], most likely an L or LL-chondrite [9]. Independent confirmation of the impactor type came from a 25 cm meteorite clast in the impact melt rock of the Morokweng crater [10].

2.5 Clearwater East (Canada)

The 20 km diameter Clearwater East crater is most likely formed by a chondritic projectile based on Ni, Os, Ir [11], Ru, and Rh inter-element ratios. The melt rocks have the highest fraction of extraterrestrial component of any terrestrial impact structure (~7% of a CI-component). The melt samples have high concentrations of 1039 µg/g Ni, 315 µg/g Cr, and 52 µg/g Co [11]. However, from observed Ni, Cr, and Co inter-element ratios a chondritic impactor contribution cannot be identified. At least contents of ≥55 µg/g Cr have to be subtracted from the Ni-rich melt samples to get CI chondritic Cr/Ni and Cr/Co ratios.

3. Summary and Conclusions

The refractory highly siderophile elements Os, Ru, Ir, and Rh are abundant in most meteorites but depleted in Earth's crust, less mobile by secondary processes and therefore most reliable elements for projectile identification. Rh/Ir, Os/Ir, Ru/Ir and Ni/Ir ratios are particularly suitable for distinguishing different types of meteorite projectiles. Even in the case of low meteoritic contamination of about 0.1 wt.% CI chondrite allow the discrimination of the type of impactor, if mantle derived rocks as target rocks can excluded. The identification of the projectile type is quite difficult, if not impossible, if the PGE derived from mantle rocks in impact melts. However, the Ru/Ir ratio of the Earth mantle of about 2 lies significantly above the Ru/Ir ratios of chondrite groups (Ru/Ir = 1.4 to 1.6) and thus the most reliable key ratio for identification [12].

References

[1] Schmidt, G., Zhou, L., and Wasson J. T. (1993) Iridium anomaly associated with the Australasian tektite-producing impact: Masses of the impactor and of the Australasian tektites. Geochimica et Cosmochimca Acta 57, 4851-4859.

[2] Folco, L., Glass, B.P., D'Orazio, M., and Rochette, P. (2018) Australasian microtektites: Impactor identification using Cr, Co and Ni ratios. Geochimica et Cosmochimca Acta 222, 550-568.

[3] Goderis, S., Tagle, R., Fritz, J., Bartoschewitz, R., and Artemieva, N. (2017) On the nature of the Ni-rich component in splash-form Australasian tektites. Geochimica et Cosmochimca Acta 217, 28-50.

[4] Shirai, N., Akhter R., and Ebihara, M. (2017) Platinum group elements in tektites: Identification of meteoritic components. Lunar and Planetary Science XLVIII.

[5] Schmidt, G., Palme, H., and Kratz, K.-L. (1997) Highly siderophile elements (Re, Os, Ir, Ru, Rh, Pd, Au) in impact melts from three European craters (Sääksjärvi, Mien and Dellen): clues to the nature of the impacting bodies. Geochimica et Cosmochimca Acta 61, 2977–2987.

[6] Tagle, R. and Claeys, P. (2005) An ordinary chondrite as impactor for the Popigai crater, Siberia. Geochimica et Cosmochimica Acta 69, 2877–2889.

[7] Koeberl, C., Armstrong, R.A., and Reimold, W.U. (1997) Morokweng, South Africa: A large impact structure of Jurassic–Cretaceous boundary age. Geology 25,731–734.

[8] Koeberl, C., Peucker-Ehrenbrink, B., Reimold, W.U., Shukolyukov, A., and Lugmair, G.W. (2002) Comparison of Os and chromium isotopic methods for the detection of meteoritic components in impactites: Examples from the Morokweng and Vredefort impact structures, South Africa. Geological Society of America Special Paper 356.

[9] McDonald, I., Andreoli, M.A.G., Hart, R.J., and Tredoux, M. (2001) Platinum-group elements in the Morokweng impact structure, South Africa: Evidence for the impact of a large ordinary chondrite projectile at the Jurassic–Cretaceous boundary. Geochimica et Cosmochimica Acta 65, 299–309.

[10] Maier, W.D., Andreoli M.A.G., McDonald I., Higgins M. D., Boyce A. J., Shukolyukov A., Lugmair G. W., Ashwal L. D., Gräser P., Ripley E. M., and Hart R. J. (2006) Discovery of a 25-cm asteroid clast in the giant Morokweng impact crater, South Africa. Nature 441, 203–206.

[11] Palme, H., Göbel, E., and Grieve, R. A. F. (1979) The distribution of volatile and siderophile elements in the impact melt of East Clearwater (Quebec). Proc. Lunar Planet Sci. Conf. 10th, 2465-2492.

[12] Schmidt, G. (2004) Are high-temperature fractionations in the solar nebula preserved in highly siderophile element systematics of the Earth mantle? Meteoritics and Planetary Science 39, 1995-2007.

EPSC Abstracts
Vol. 12, EPSC2018-133, 2018
European Planetary Science Congress 2018

Shock alteration of geological minerals from impact cratering experiments

K. H. Harriss[1] and M. J. Burchell[1],
[1]School of Physical Sciences, University of Kent, Canterbury, CT2 7NH, UK
k.harriss@kent.ac.uk

Abstract

Shock synthesis of individual geological minerals has been investigated to discover the individual effects of differing levels of impact generated shock. We find that due to the structure of the minerals olivine, enstatite and diopside, the minerals are altered at different peak shock pressures (6 – 183 GPa). This report gives the initial results from an on-going project which aims to investigate shock effects in many common geological minerals to help us further understand the composition of highly shock material we study today.

1. Introduction

Impact cratering has shaped the celestial bodies of the solar system to those we observe and study today. These events create a sudden and short-lived environment of high energy, temperature and shock pressure at the point of impact that the geological materials are often altered, melted or vaporized [1]. The shock effect can alter the composition and even the structure of the geological minerals as observed by [2 and 3]. By recreating these impact scenarios in a controlled laboratory environment, the effect of different shock pressures on various mineral compositions and textures can be examined to aid in the understanding of the manner in which these high peak shocked pressure events have shaped the composition of the material that dominates our solar system today. This builds upon previous work and agrees with [4] that a new shock classification system is required.

2. Method

Powdered and whole grains of common geological minerals found in chondrites, including orthopyroxene, clinopyroxene powders and olivine (peridot), were fired at speeds between 1 and 7 kms^{-1} (see table 1 for equivalent calculated shock pressures) into Al foil (1080) and Stainless Steel (304) using the Light gas gun (LGG) at the University of Kent [5]. The residues in the resulting craters were analyzed using Raman (532 nm), SEM and FEGSEM analysis and compared to the composition and structure of the un-shot minerals. Details of the shot undertaken so far are shown in Table 1. Values used for the calculation of the peak shock pressure using the planar impact approximation were taken from [6].

Table 1: Shots undertook showing the impact speed and calculated peak shock pressure.

Mineral	Target	Impact Speed range (kms^{-1})	Peak shock Pressure (GPa)
Olivine	Steel	2 – 5	30 – 108
Diopside	Al	1 – 8	9 – 183
Enstatite	Al	1 – 7	6 - 105

3. Results

The initial results show that, depending on the structure of the mineral, a significant change in the composition can occur when experiencing different shock pressures. In this report, we focus on the results of the Raman analysis

3.1 Enstatite

The enstatite used has a composition of $En_{86}Fs_{13}Wo_1$ and was supplied by Anton Kearsley. Post-impact the residues show very few peaks when analysed by Raman and many are lost in the background, one peak shows a broadening effect between 650 and 750 $cm^{-}1$. This feature is observed at all the shock pressured investigated. This suggests that shock affects the Raman signal of enstatite at a much lower shock pressure then olivine, i.e. at about 29 GPa.

3.2 Diopside

The diopside mineral investigated had a composition of $Wo_{49}En_{48}Fs_3$ from Jaipur, India supplied by M. McCanta, University of Tennessee [7]. When the

residue is compared to the Raman spectrum from the un-shot material most the major peaks are identified up to 145 GPa beyond this the peaks are lost and the carbon D and G band peaks become dominant and a broadening of the peaks around 730 cm^{-1}. The wavenumbers do vary compared with the unshot spectra but no correlation is observed between size/direction of shift and the shock pressures, this suggests that there are no observed effects up to a shock pressure of 145 GPa.

3.3 Peridot

The composition of the peridot used was $Fo_{96.}$
For impact speeds of 2.0, 3.3 and 5.3 km s^{-1} there was no significant change in the position of the main Raman peaks, denoted as P1 and P2 (Table 2). This implies that a pressure of 108 GPa is required before large olivine mineral grains (here typically 3 mm peridot) show significant structural changes. This differs from the result of [2] which investigated much finer powdered (typically 1 – 10 µm) olivine material in similar impacts.
Though the P1 and P2 peaks remain un-altered, other small peaks at 961 cm^{-1} are lost in all of the spectra of the post shot material.

Table 2: RAMAN wave number for the olivine P1 and P2 peaks of the impacted Peridot residue

Impact speed	P1 position	P2 position
2.0 km s^{-1}	823.7	855.7
3.3 km s^{-1}	823.9	855.9
5.3 km s^{-1}	822.2	854.2
Un-shot	822.2	854.2

4. Discussion

The comparisons between the shocked and un-shocked minerals show that pyroxene minerals exhibit a different structural/composition change to that of olivine. The different mineral types appear to experience a major change in structure detected by Raman analysis which is likely linked to the structure of the minerals, such as the chain and orthorhombic structure of the pyroxene and olivine respectively.

Note that samples place in the gun can subsequently show a large D and G Raman band, which is a result of contamination from the carbon within the rifle powder used in the experiments. Therefore we do not study the D and G bands in this work.

This work is ongoing and will soon include other common minerals such as feldspar (albite and anorthite), quartz and pyrite as well as detailed FEGSEM and SEM analysis of all residues. By understanding how each mineral reacts at different shock pressures the experiments can move on to shock syntheses of whole rock facies to understand the shock interaction between the different minerals at grain boundaries and other mineral interfaces.

Acknowledgements

The authors would like to thank: STFC for funding K. Harriss and the LGG. Mike Cole the experimental officer for the LGG for his help and training, Dr Molly McCanta [7], for supplying the clinopyroxene material and Anton Kearsley for supplying the orthopyroxene material.

References

[1] Stöffler, D, and F. Langenhorst. *Meteoritics & Planetary Science* 29, no. 2 (1994): 155-181.

[2] Harriss, K H., and M. J. Burchell *Meteoritics & Planetary Science* 51, no. 7 (2016): 1289-1300.

[3] Burchell, M J., N. J. Foster, A T. Kearsley, and J. A. Creighton. *Meteoritics & Planetary Science* 43, no. 1-2 (2008): 135-142.

[4] Stöffler, D., Hamann, C. and Metzler, K., Meteoritics & Planetary Science, 53(1), pp.5-49. (2018)

[5] Burchell, M J., M. Cole, J. A. M. McDonnell, and John C. Zarnecki. Measurement Science and Technology 10, no. 1 (1999): 41.

[6] Ahrens, T J., and M. L. Johnson. *Shock wave data for minerals*. American Geophysical Union, (1994).

[7] McCanta, M. C., and M. D. Dyar. *Meteoritics & Planetary Science* 52, no. 2 (2017): 320-332.

EPSC Abstracts
Vol. 12, EPSC2018-139, 2018
European Planetary Science Congress 2018

Influence of Target Properties on Ejecta Scaling Relationships

R. Luther (1,2) and K. Wünnemann (1,2)
(1) Museum für Naturkunde Berlin, Leibniz Institute for Evolution and Biodiversity Science, Germany, (2) Institute of Geological Sciences, Freie Universität Berlin, Germany. (Robert.luther@mfn-berlin.de)

Abstract

Crater scaling relationships [e.g., 1, 2] relate observables of a cratering event (e.g., crater radius, ejection velocity) with the impactor characteristics (e.g., size, impact velocity), allowing for predicting the outcome of a cratering event. We show results for scaling parameters derived from numerical experiments. We focus on the dependence of ejection dynamics from target material properties like strength and porosity.

1. Introduction

Target material properties influence the cratering process and, consequently, are reflected within the scaling parameters of scaling relationships that are used to predict the outcome of the event [e.g., 3]. In laboratory studies, it is difficult to vary individual material parameters. In contrast, numerical studies allow for a systematic analysis of the influence of target properties on the outcome of a cratering event. In this study, we analyse the ejection dynamics in numerical experiments for different target materials and present scaling parameters for ejecta scaling [cf. 4 for more details]. These scaling parameters allow for using scaling relationships to predict the outcome of different impact scenarios (gravity, impact velocity, projectile size). According to theoretical considerations scaling parameters should be consistent for different formulations of scaling relationships like ejecta scaling or crater size scaling.

2. Method

We use the iSALE shock physics code [5-7] to conduct a systematic parameter study by simulating different impact scenarios. iSALE enables to describe the resistance of rocks against deformation and the thermodynamic response to compression by different material models. We use a Drucker-Prager rheology with coefficient of frictions between 0.0 and 1.0 for non-porous targets. We vary target porosities between 0% and 42% for materials with a coefficient of friction of 0.6. All simulated materials are cohesion-free. We use the ANEOS for quartzite [8]. We determine the ejection parameters (velocity and angle) by Lagrangian tracers. Material represented by tracers is considered as ejecta when it satisfies a specific criterion: the tracer has to be above a specific height above the pre-impact surface that we chose to be one projectile radius in all simulations. Note, the ejection velocity is consistent also for somewhat larger or smaller ejection-criterion-altitudes [4]. We plot the resultant ejection velocity v_{ej} normalised by $\sqrt{gR}$ against the normalised launch distance x/R, where g and R are the gravitational acceleration and transient crater radius, respectively (Figure 1). For deriving scaling parameters K and μ based on the ejection velocities, we use the following equation [2]:

$$\frac{v_{ej}}{\sqrt{gR}} = K\left(\frac{x}{R}\right)^{-\frac{1}{\mu}}. \quad (1)$$

Using Eq. 1 requires excluding ejecta from close within the transient rim where the power law approximation fails. Therefore, we use a fixed minimum ejection velocity of ~80 m/s for all models that is high enough to exclude ejecta near the rim, and which allows for comparability between the models.

3. Results

The increase of material strength (i.e, the coefficient of friction) causes a reduction in crater size under equal impact conditions. Hence, ejection velocities in a normalised plot show a stronger decrease with ejection position for larger strength (Fig. 1 i), which correlates with the onset of ejection at larger normalised ejection positions. The increase of porosity causes a reduction of the initial ejection

velocities at small ejection positions (Fig. 1 ii). The normalised velocities at x/R=1 is about equal for all porosities. Consequently, the decrease of velocity is the greatest for non-porous target materials. The scaling parameters are given in tables Tab. 1 & 2.

Table 1: Scaling Parameters, non-porous material.

Coefficient of friction	K	μ
0.0	0.43	0.49
0.2	0.53	0.49
0.4	0.63	0.47
0.6	0.77	0.46
0.8	0.81	0.46
1.0	0.82	0.47

Table 2: Scaling Parameters, material with coefficient of friction 0.6.

porosity	K	μ
0%	0.77	0.46
10%	0.66	0.47
20%	0.62	0.49
30%	0.61	0.52
42%	0.70	0.62

i)

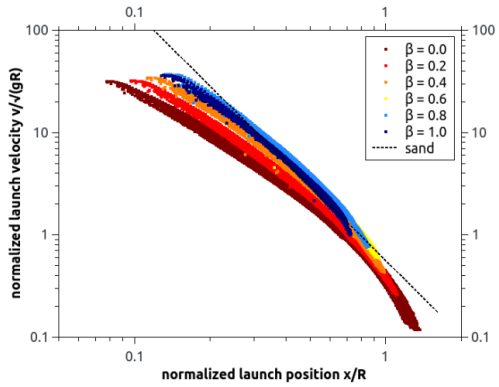

ii)

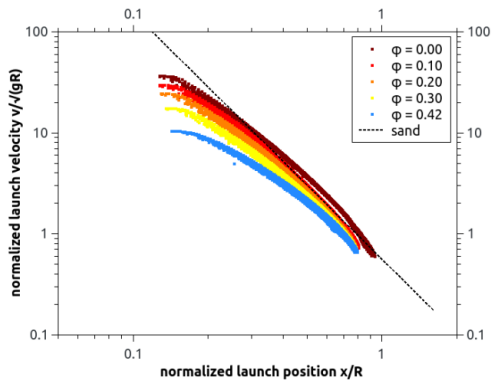

Figure 1: Ejection velocity for non-porous materials with coefficients of friction from 0.0-1.0 (i), and for targets with a coefficient of friction of 0.6 and porosities from 0-42% (ii). Impact conditions: velocity 5 km/s, projectiles radius 25 m, Earth gravity. The sand line is from [2].

4. Summary and Conclusions

We present results for scaling parameters for target materials with various strength and porosity. Target properties influence ejection velocities, and fitting Eq. 1 to our numerical ejection data yields the given scaling results. These scaling parameters deviate from results based on crater size (e.g., μ=0.41 for 42 % porosity [2] vs. μ=0.62, this study). However, our value falls into the range μ=0.5-0.66 given by [9]. Further experiments also show deviations of scaling parameters depending on the observables they are derived from [10]. This could be linked to differences in early-stage (e.g., ejection, crater growth) versus late-stage processes (e.g., crater size). Therefore, we think that care must be taken when scaling ejection characteristics, and parameters for such purposes should be chosen based on ejection studies.

Acknowledgements

This project is funded by the German Research Foundation: MEMIN FOR887 (#WU 355/6-2) and SFB-TRR170 (A4). We thank the developers of iSALE, Vimod & pySALEPlot.

References

[1] Holsapple, K.: The Scaling of Impact Processes in Planetary Sciences, Annu. Rev. Earth Planet. Sci. 21, pp. 333-373, 1993. [2] Housen, K. R. and Holsapple, K. A.: Ejecta from impact craters, Icarus 211, pp. 856-875, 2011. [3] Prieur, N.; Rolf, T.; Luther, R.; Wünnemann, K.; Xiao, Z. and Werner, S.: The effect of target properties on transient crater scaling for simple craters, J. Geophys. Res. Planets 122, 1704-1726, 2017. [4] Luther, R.; Zhu, M.-H.; Collins, G. S. and Wünnemann, K.: Effect of Target Properties and Impact Velocity on Ejecta Dynamics and Ejecta Deposition, Meteorit. & Planet. Sci., 2018 (submitted). [5] Amsden A., Ruppel, H. M., and Hirt, C. W. : Sale: A Simplified ALE Computer program for Fluid Flow at All Speeds, LANL, LA-8095, 101, 1980. [6] Collins, G. S., Melosh, H. J., and Ivanov, B. A.: Modeling damage and deformation in impact simulations, Meteorit. & Planet. Sci. 39, pp. 217-231, 2004. [7] Wünnemann, K., Collins, G. S., and Melosh, H. J.: A strain-based porosity model for use in hydrocode simulations of impacts and implications for transient crater growth in porous targets, Icarus 180, pp. 514-527, 2006. [8] Melosh, H. J: A hydrocode equation of state for SiO_2, Meteorit. & Planet. Sci. 42 (12), pp. 2079-2098, 2007. [9] Cintala, M. J.; Berthoud, L. and Hörz, F.: Ejection-velocity distributions from impacts into coarse-grained sand, Meteorit. & Planet. Sci. 34 (4), pp. 605-623, 1999. [10] Tsujido, S.; Arakawa, M.; Suzuki, A. and Yasui, M.: Ejecta velocity distribution of impact craters formed on quartz sand: Effect of projectile density on crater scaling law, Icarus, 262, pp. 79-92, 2015.

EPSC Abstracts
Vol. 12, EPSC2018-212, 2018
European Planetary Science Congress 2018

Shock-darkening in a shock-recovered ordinary chondrite? Numerical model of the experiment

J. Moreau (1), T. Kohout (1,2) and K. Wünnemann (3)
(1) Department of Geosciences and Geography, University of Helsinki, Finland, (juulia.moreau@helsinki.fi), (2) Institute of Geology, The Czech Academy of Sciences, Prague, Czech Republic, (3) Museum für Naturkunde, Leibniz Institute for Evolution and Biodiversity Science, Berlin, Germany

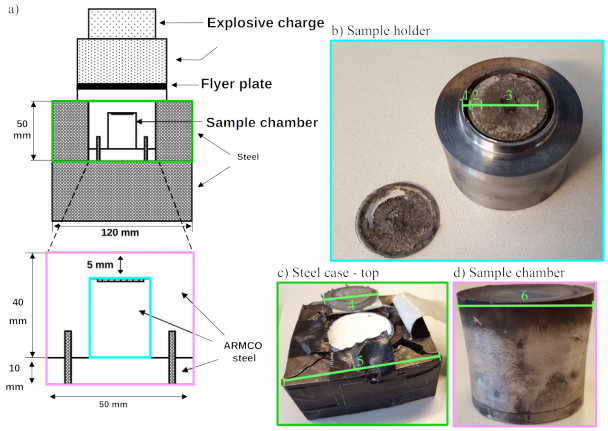

Fig. 1. a) schematic of the experiment, b) the sample holder with the shocked Chelyabinsk LL5 meteorite that are both encased in c) the steel case, top, and then in d) the sample chamber. Colored boxes link b-d) to a). The green lines and numerals respectively show 1) a shocked deformation gap between the sample and sample holder, 2) the outer light rim of the sample, 3) the darker inner sample, supposedly shock-darkened, 4) the remnant of the flyer plate, 5) the shattered steel box, and 6) the deformation effect of the shock on the sample chamber. Image a) is modified from [8] and displays the current experiment dimensions.

Abstract

Shock-darkening in ordinary chondrites is the melting of iron sulfides and metals that spread into a network of veins, rendering the lithology darker. A shock-recovery experiment was carried on the Chelyabinsk LL5 meteorite. Using the shock physics code iSALE, we observed the distribution of peak shock pressures in the sample at a pressure of 55.5 GPa in steel (to obtain 40-50 GPa in sample, the pressure range for shock-darkening). The shock-recovered meteorite showed a darkening of lithology.

1. Introduction

Shock-recovery experiments are used to shock load rock samples [1,2]. The experimental setup (Fig. 1a) allows for a reverberating shock wave to travel in the sample and, eventually, equilibrate with the pressure in steel. Shock-darkening is a shock-metamorphic process in ordinary chondrites [3,4], thus a shock-recovery experiment was carried to shock a light-lithology sample of the Chelyabinsk LL5 meteorite and we carried numerical models to understand the shock wave propagation and peak shock pressures distribution in the sample.

2. Methods

To study the shock wave propagation in the shock recovery experiment, we used the shock physics code iSALE [5]. In a mesoscale model (Fig. 2a) of a planar shock wave in 2D-cylindrical mesh made of 1000x934 cells, we studied the complex interaction of the shock wave between different phases (iron, olivine and tantalum). The sample is represented by olivine, the major silicate component of ordinary chondrites, with rock strength properties. Tantalum was used in the experiment as an hermetic foil for the sample and included in the numerical model. Iron represented the ARMCO steel case [6] and possessed equivalent strength properties in iSALE. Porosity of the (numerical) sample was 6%. Additionally, we used peak shock pressures and peak temperatures recorded in tracers in the sample to determine the pressure needed in steel [7]. The shock-recovery experiment was done at the Ernst Mach Institute, Germany.

3. Results

The shock-recovered sample, encased in the sample chamber, is shown in Fig. 1b. Pending further results, one can observe that the sample has a darkened lithology with a lighter rim. Several deformation features are displayed in Fig. 1. In addition we provide the resulting peak-shock pressures distribution from the numerical model in the sample and steel case, shown in Fig. 2b. The shock pressure in the steel was 55.5 GPa, entry pressure in sample

was ~32.8 GPa and peak pressures in sample, after reverberations, were heterogeneous and displayed a value of 47.6 GPa (s.d. 4.7 GPa).

4. Discussion & Conclusions

First, the peak shock pressures in the sample are very heterogeneous and this is due to the short pulsation time of the shock wave that decays already in the sample plate while a first reflection occurs from the bottom of the sample. The resulting distribution of pressures seen in Fig. 2b and the resulting deformation in Fig. 1b and 1d are, somehow, related. The generated pressures in the sample may have generated shock-darkening, pending further investigation.

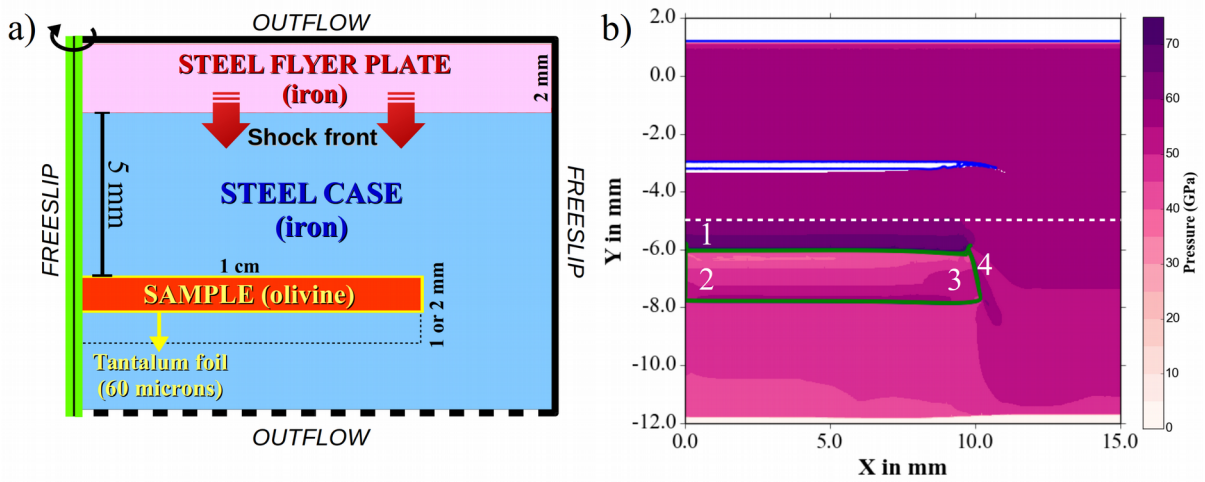

Fig. 2. a) schematic of the numerical model and b) resulting peak shock pressures in the steel and sample (green box). The shock pressure in steel was 55.5 GPa. Numerals are 1) the reflected pressures from the tantalum foil, 2) the heterogeneous distribution of pressures in the sample, 3) concentration of pressures at the edge due to complex reflections, and 4) deformation of the sample, possible explanation of a gap in the sample holder, Fig. 1b-1.

Acknowledgements

Our thanks go to the team of the Museum für Naturkunde in Berlin, Germany, for sharing their knowledge and ideas with us. The experiment was carried by Andreas Holzwarth and Hagen Aurich. This work is supported by the Academy of Finland.

References

[1] Langenhorst F., Deutsch A., 1994. Shock experiments on pre-heated alpha- and beta-quartz; I, Optical and density data. Earth and Planetary Science Letters, 125:407–420.

[2] Langenhorst F. and Hornemann U. 2005. Shock experiments on minerals: Basic physics and techniques. EMU Notes in Mineralogy, 7(15):357-387.

[3] Kohout T., Gritsevich M., Grokhovsky V. I., Yakokiev G. A., Haloda J., Halodova P., Michallik R. M., Penttilä A. and Muinonen K. 2014. Mineralogy, reflectance spectra, and physical properties of the Chelyabinsk LL5 chondrite - Insight into shock-induced changes in asteroid regoliths. Icarus 228:78–85, DOI:10.1016/j.icarus.2013.09.027.

[4] Moreau J., Kohout T. and Wünnemann K. 2017. Shock-darkening in ordinary chondrites: determination of the pressure-temperature conditions by shock physics mesoscale modeling. Meteoritics & Planetary Science, 52(11):2375-2390, DOI:10.1111/maps.12935.

[5] Wünnemann K., Collins G. and Melosh H. 2006. A strain-based porosity model for use in hydrocode simulations of impact and implication for transient crater growth in porous targets. Icarus, 180:514-527.

[6] Kohout T., Pesonen L. J., Deutsch A., Wünnemann K., Nowka D., Hornemann U. and Heikinheimo E. 2012. Shock experiments in range of 10-45 GPa with small multidomain magnetite in porous targets. Meteoritics & Planetary Science, 47:10, 1671-1680.

[7] Moreau J., Kohout T. and Wünnemann K. 2017. Shock-darkening in ordinary chondrites – Numerical calibration of shock-recovery experiments. *48th Lunar and Planetary Science Conference*, The Woodlands, Texas, USA, abstract #1558.

[8] Stöffler D., Horneck G., Ott S., Hornemann U., Cockell C. S., Moeller R., Meyer C., de Vera J.-P., Fritz J. and Artemieva N. A. 2007. Experimental evidence for the potential impact ejection of viable microorganisms rom Mars and Mars-like planets. *Icarus*, 186:585-588.

EPSC Abstracts
Vol. 12, EPSC2018-213, 2018
European Planetary Science Congress 2018

Direct quartz-coesite transformation in shocked sandstones from Kamil Crater (Egypt)

Luigi Folco (1) (luigi.folco@unipi.it), Enrico Mugnaioli (2), Maurizio Gemelli (1), Matteo Masotta (1) and Fabrizio Campanale (1)

(1) Dipartimento di Scienze della Terra, Università d Pisa, Via S. Maria 53, 56126 Pisa, Italy

(2) Istituto Italiano di Tecnologia, Center for Nanotechnology Innovation@NEST, Pisa, Italy

Abstract

We show that coesite in shocked porous sandstones forms through direct subsolidus transformation from quartz, in contrast to what suggested for crystalline quartz-bearing targets. This work documents the role of pore collapse in producing localized pressure-temperature-time gradients in shocked porous targets, as predicted by numerical models in the literature, and raises the question of the kinetics of the direct quartz-coesite transformation induced by shock.

1. Introduction

The presence of coesite in quartz-bearing target rocks experiencing shock conditions beyond the limits of the coesite stability field is a controversial issue [1, 2, 3, 4]. Coesite was identified in shocked sandstone ejecta from the 45-m-diameter, less than 5,000 years old Kamil Crater in Egypt [5, 6]. The exceptional state of preservation of Kamil Crater and, in particular, the lack of evidence for post-shock thermal overprint and alteration due to hydrothermal activity typically observed in shock metamorphic rocks from larger impact structures [e.g., 4, 7], prompted us to test current models for formation of coesite in the shocked sandstone ejecta through a combined scanning electron microscopy, Raman spectroscopy and electron diffraction microstructural study.

2. Results

The shocked sandstone studied in this work is a medium-grained quartzarenite dominated by heavily shocked, equigranular quartz grains with an average grain size of 1 mm (~78 vol%) and including accessory tourmaline and zircon [6]. Intergranular veins and pockets (up to 1 mm across) of silica glass contain microcrystalline coesite. These domains are microstructurally analogous to the so-called symplectic regions first described in the Coconino Sandstones from the Barringer Crater, USA [1]. Orientations and frequency of PDF in shocked quartz ({10-13}, 23%, and {10-12}, 14% [6]) and amount of silica glass (~22 vol%) indicate shock pressures of 20- 25 GPa [8, 9].

Intergranular symplectic regions show microstructural zoning. From the core of the quartz crystals to the core of the symplectic regions, we can distinguish a "quartz zone", a "coesite zone" and a "silica glass" zone. The quartz zone consists of PDF-bearing shocked quartz. The coesite zone, up to several tens of μm in thickness, typically consists of polycrystalline aggregates of micro-to-nanocrystals (<5 μm) coesite set in pure silica glass, i.e. lechatelierite. Coesite shows fine polysynthetic twinning parallel to the (010) plane. Polycrystalline aggregates arranged along planes that are nearly parallel to PDF of the quartz crystals in the adjacent quartz zone consists of fine coesite plus quartz intergrowths. This indicates topotactic growth of coesite at the expense of the PDF-bearing quartz crystals. Flame-like corrosion textures at the margins of the coesite aggregates indicate subsequent melting of the pre-existing crystalline silica phases. The silica glass zone consists of homogeneous lechatelierite with usually one central bubble up to several tens of μm across.

3. Discussion

Petrographic data confirm that, in porous sedimentary rocks, coesite forms locally in symplectic regions, as reported in the literature from

other impact structures (e.g., Coconino Sandstone from Barringer Crater [1]). This localization and the petrographic zoning of the symplectic regions attests to significant heterogeneity in the space-time distribution of P-T conditions within the rock. These gradients are associated with shock wave reverberations due to pore collapse in shocked porous sedimentary rocks, as derived from recent numerical simulation of shock-induced pore collapse by [10].

The most straightforward explanation for the topotactic growth of coesite at the expense of the PDF-bearing quartz crystals is direct quartz-coesite subsolidus transformation. Shock-front reverberation caused by the presence of pores and discontinuities in the shocked material could last long enough to allow the transformation of quartz into coesite. This transformation may be energetically and topologically facilitated by the ubiquitous and pervasive twinning in shocked coesite. Although such subsolidus transformation has been recently hypothesized for impact coesite in shock veins of metaquartzites from the ~300-km-diameter Paleoproterozoic Vredefort impact structure [11], this mechanism is in contrast with what proposed for crystalline targets, i.e. that coesite forms during shock unloading through crystallization from a silica shock melt [e.g. 2, 4] or subsolidus nucleation from highly densified diaplectic silica glass [3]. These differences suggests that different coesite formation mechanisms act in different targets.

4. Conclusions

Mineralogical and petrographic data from shocked Kamil Crater sandstones thus document the effective role of pore collapse in producing heterogeneous pressure-temperature-time (P-T-t) distributions in porous targets, as predicted by numerical models in the literature. This is relevant in defining of the P-T-t paths of shock metamorphic rocks, and therefore the shock classification of impactites and impact scenarios.

References

[1] Kieffer, S.W., Phakey, P.P., Christie, J.M., Shock processes in porous quartzite: transmission electron microscope observations and theory: Contribution to Mineralogy and Petrology, v. 59, p. 41–93, 1976.

[11] [2] Langenhorst, F., Nanostructures in ultrahigh-pressure metamorphic coesite and diamond: a genetic fingerprint. *Mitt. Österr. Miner. Ges*., v. 148, 401-412, 2003.

[3] Stähle, V., Altherr, R., Koch, M., and Nasdala, L., Shock induced growth and metastability of stishovite and coesite in lithic clasts from suevite of the Ries impact crater (Germany): Contributions to Mineralogy and Petrology, v. 155, p. 457–472, 2008.

[4] Fazio, A., Mansfeld, U., and Langenhorst F., Coesite in suevite from the Ries impact structure (Germany): From formation to postshock evolution: Meteoritics and Planetary Science, v. 52, p. 1437-1448, 2017.

[5] Folco. L., Di Martino, M., El Barkooky, A., D'Orazio, M., Lethy, A., Urbini, S., Nicolosi, I., Hafez, M., Cordier, C., van Ginneken, M., Zeoli, A., Radwan, A.M., El Khrepy, S., El Gabry, M., Gomaa, M., Barakat, A.A., Serra, R., El Sharkawi, M., The Kamil Crater in Egypt: Science, v. 329, p. 804.

[6] Fazio, A., Folco, L., D'Orazio, M., Frezzotti, M.L., and Cordier, C., 2014, Shock metamorphism and impact melting in small impact craters on Earth: Evidence from Kamil Crater, Egypt: Meteoritics and Planetary Science, v. 49, p. 2175–2200, 2010.

[7] Martini, J.E.J., The nature, distribution, and genesis of the coesite and stishovite associated with the pseudotachylite of the Vredefort Dome, South Africa: Earth and Planetary Science Letters, v. 103, p. 285–300, 1991.

[8] Stöffler, D., and Langenhorst, F., Shock metamorphism of quartz in nature and experiment: I. Basic observation and theory: Meteoritics and Planetary Science, v. 29, p. 155–181, 1994.

[9] Kowitz, A., Güldemeister N., Schmitt, R.T., Reimold W-U., Wünnemann, K., and Holzwarth A., Revision and recalibration of existing shock classifications for quartzose rocks using low-shock pressure (2.5–20 GPa) recovery experiments and mesoscale numerical modeling: Meteoritics and Planetary Science, v. 51, p. 1741–1761, 2016.

10] Güldemeister, N., Wünnemann K., Durr N., Hiremaier S., 2013, Propagation of impact-induced shock waves in porous sandstone using mesoscale modeling. Meteoritics and Planetary Science 48, v. 1, p. 115–133, 2013.

[11] Smyth, J.R., and Hatton, C.J., Coesite-sanidine grospydite from Roberts-Victor kimberlite: Earth and Planetary Science Letters, v. 34. p. 284–290, 1997.

EPSC Abstracts
Vol. 12, EPSC2018-224, 2018
European Planetary Science Congress 2018

Formation of impact basins on the moon - insights from numerical modeling, gravity and remote sensing data

Tomke Lompa (1), Kai Wünnemann (1) and Meng-Hua Zhu (2)
(1) Museum für Naturkunde - Leibniz Institute for Evolution and Biodiversity Science, Berlin, Germany (tomke.froechtenicht@mfn.berlin), (2) Space Science Institute, Macau University of Science and Technology, Taipa, Macau

Abstract

The surface of the Moon was shaped by large-scale impact basins. The formation of impact basins is influenced by target properties and most obviously by the size, composition (mass), and velocity of the impactor. Beside the surface expression (crater morphology) as the most obvious outcome of an impact event also the gravity field, local petrography and thermal structure have been influenced by these events ([2], [10]). Satellite gravity data from GRAIL-mission and topography datasets from LOLA-instruments provide further insights and additional constraints on the formation mechanism, crater morphology, crustal structure and ejecta thickness. Previous numerical modeling studies use different kinetic energies - based on impactor diameter, velocity, and/or mass - to match either gravity or ejecta thickness data. In this study, we aim at the development of a new numerical model that satisfies both observational constraints, including the ejecta distribution and subsurface structure based on the gravity data. In addition, we will quantify the deposition of ejecta and the production and distribution of impact melt. The resulting, improved model for Orientale will be the basis for studying all basins on the Moon.

1. Introduction

In previous studies lunar impact basins have been investigated (e.g. [2], [5], [6], [9]) to obtain a better understanding of the formation and subsequent evolution as a function of varying target conditions. Satellite data sets can be used for different approaches to get insights into the Moons interior: Gravity data from GRAIL were used for developing a crustal thickness model [7] and high-resolution topography data from LOLA leads to investigate the impact ejecta thicknesses on the Moons surface [9]. In this study, we use the Orientale basin as the benchmark for further systematic numerical modeling studies of all impact basins on the Moon. A formation model of Orientale has been developed taking the ejecta distribution into account [9]. The simulation predicts an impactor of 100 km in diameter and a velocity of 12 km/s. Alternatively, the study of Johnson et. al [3] focuses on the subsurface structure, especially in the area of the ring of Orientale. In this model, the kinetic energy is only half of the impact energy according to the model of Zhu et. al [9] and corresponds to an impactor diameter of 74 km. A lower kinetic energy results in a smaller transient crater and, thus, a smaller amount of ejected material, which results in a thinner ejecta blanket in the vicinity of Orientale.

2. Method

We use the iSALE2D shock physics code ([1], [8]) to simulate the formation of large basins. We consider Orientale Basin as a test case, using parameters from previous simulations ([6], [9]). The crust consists of gabbroic anorthosite, mantle and projectile of dunite. As Orientale is located at the boundary of the lunar highlands, we considered a 40 km and 60 km thick relatively cold crust [9]. As observational constraints we use topographic data from LOLA and Bouguer gravity from GRAIL. Furthermore, a crustal thickness model [7] is used in our model.

3. Results

In a first step we have modeled the formation of the Orientale basin consistent with observational constraints such as the present day morphometry, the gravity field, and the thickness of the ejecta deposits as a function of distance from the crater center. Our model confirms that a 100 km diameter body impacting the lunar surface at 12 km/s formed the Orientale basin [9]. The alternative model [3] with a 74 km diameter impactor has a significantly smaller transient crater and the ejecta thickness distribution does not match the observed decrease along with the distance.

Fig.1 shows a cross section through the 100 km-diameter-impactor model running from the crater center up to a radial distance of 600 km. Fig. 1(a) presents the Bouguer gravity profiles from the model (g_{model}) and the measurements from GRAIL (g_{GRAIL}). From Fig. 1(a), we find that the Bouguer gravity reaches its maximum in the center of the crater caused by mantle material that was uplifted close to the surface during the basin forming process. Low mantle densities in the craters center correspond to high temperatures in the upwelling mantle (Fig. 1(b)-(c)). The low-density crustal layer can explain lower Bouguer anomalies at distances > 350 km. The general trend of calculated Bouguer anomalies follows the shape of the GRAIL measurements. The red and green lines in Fig. 1(b)-(c) show observed topography data and the crustal thickness model based on GRAIL data. The crustal thickness model agrees with our model for distances > 350 km, where relatively little deformation occurs during the impact. However, in the central part our model significantly deviates from the crustal thickness model [7].

4. Figures

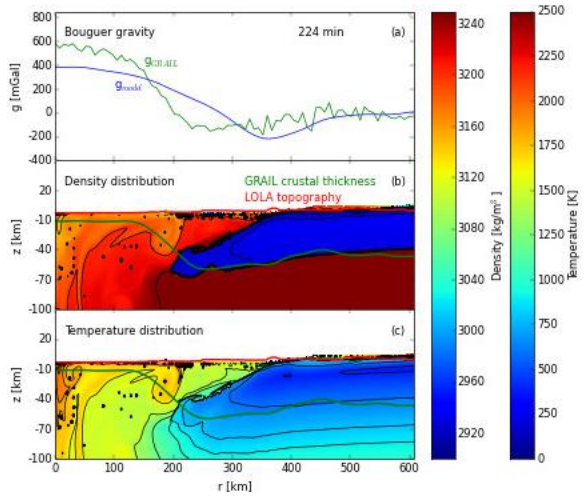

Figure 1: Profile through the Mare Orientale. (a): Bouguer gravity anomalies (b): Density distribution and (c): Temperature distribution in the target material. r: Distance from the crater center.

5. Conclusion

We consider the amount of ejecta as the best measure of transient crater size and, thus, impact energy, which rules out the low-impact-energy model. Better agreement with the gravity data for the higher-impact-energy model may be achieved by adjusting other target properties. By a extensive suite of models we will test the effect of a range of target parameters to minimize the discrepancy between model and observation constraints. In addition we will determine the thermodynamic conditions in the target material and quantify the emplacement of ejecta.

Acknowledgements

This work is part of the SFB transregio TRR 170 “Late Accretion onto terrestrial planets”, Project A “Timing of late Accretion”.

References

[1] Collins, G. S., Melosh, H. J. and Ivanov, B. A.: Modeling damage and deformation in impact simulations, Meteoritics & Planetary Science, Vol. 39, pp. 217-231, 2004.

[2] Ivanov, B., Melosh, H. and Pierazzo, E.: Basin-forming impacts: Reconnaissance modeling, Large Meteorite Impacts and Planetary Evolution IV., pp. 29-49, 2010.

[3] Johnson, B. C. et al.: Formation of the Orientale lunar multiring basin, Science, Vol. 354, pp. 441-444, 2016.

[4] Melosh, H. J. et al.: The Origin of Lunar Mascon Basins, Science, Vol. 340, pp. 1552-1555, 2013.

[5] Miljkovic, K. et al.: Asymmetric Distribution of Lunar Impact Basins Caused by Variations in Target Properties, Science, Vol. 342, pp. 724-726, 2013.

[6] Potter, R. W. K. et al.: Numerical modeling of the formation and structure of the Orientale impact basin, Journal of Geophysical Research: Planets, Vol. 118, pp. 963-979, 2013.

[7] Wieczorek, M. A. et al.: The Crust of the Moon as Seen by GRAIL, Science, Vol. 339, pp. 671-675, 2013.

[8] Wünnemann, K., Collins, G. and Melosh, H.: A strain-based porosity model for use in hydrocode simulations of impacts and implications for transient crater growth in porous targets, Icarus, Vol. 180, pp. 514-527, 2006.

[9] Zhu, M.-H., Wünnemann, K. and Potter, R. W. K.: Numerical modeling of the ejecta distribution and formation of the Orientale basin on the Moon, Journal of Geophysical Research: Planets, Vol. 120, pp. 2118-2134, 2015.

[10] Zuber, M. T. et al.: Gravity Field of the Moon from the Gravity Recovery and Interior Laboratory (GRAIL) Mission, Science, Vol. 339, pp. 668-671, 2013.

EPSC Abstracts
Vol. 12, EPSC2018-261, 2018
European Planetary Science Congress 2018

^{14}C dating of small impact craters on Earth

A. Losiak[1,2], A. Jõeleht[3], J. Plado[3], M. Szyszka[4], E.M. Wild[5], P. Steier[5]
[1]wildFIRE Lab, Hatherly Laboratories, Uni. of Exeter (a.i.losiak@exeter.ac.uk); [2]Planetary Geology Lab, Institute of Geological Sciences, Polish Academy of Sciences, Poland; 3Department of Geology, Uni. of Tartu, Estonia; [4]Institute of Geology, Adam Mickiewicz Uni. in Poznan; 5VERA Laboratory, Faculty of Physics—Isotope Research & Nuclear Physics, Uni. of Vienna.

Abstract

We suggest that the real age of Kaali impact event is 100-200 years younger than proposed in [8] and was formed 3062±19 ^{14}C yr BP or 1400-1260 cal. BCE. This new study provides a better understanding of the dating of small impact craters on Earth using ^{14}C method.

1. Introduction

Precise and accurate dating of small, recent impact craters on Earth is a challenging task. In most cases 40Ar/39Ar, K/Ar, Rb/Sr, U/Pb dating methods cannot be used because energies involved in formation of those structures are not sufficient to reset those isotopic systems [1]. Also, in a rare case of a small impact crater associated with some amount of impact melt (Kamil in Egypt [2]), the size of the measurement error that can be obtained by the methods mentioned above would make the dating practically pointless [3].

As a result, ^{14}C dating remains the main way of determining the age of small, recent impact craters on Earth. Most commonly, the organic material from within a crater is used. Those type of samples reveal only the minimum age of a structure (Macha: [4]), and the extent of the time-lag between the crater formation and dateble-material deposition remains very hard to determine. This problem is well illustrated by comparing ^{14}C ages of various craters from the same strewn fields; in case of Morasko they can differ by a couple thousand years [5]. The maximum age of a crater can be obtained by ^{14}C dating of the paleosol that is covered by proximal ejecta (Whitecourt: [6]). Dating paleosols, however, tends to be problematic because different fractions of soil may yield dissimilar ages [7], and also leaves the unknown time-lag between the obtained date and the actual crater age. The best way to date a young impact crater is to ^{14}C date an organism that was killed by the impact event, as it was recently done to determine the age of Kaali craters [8]. But as everything in life, even the best method can be tricky.

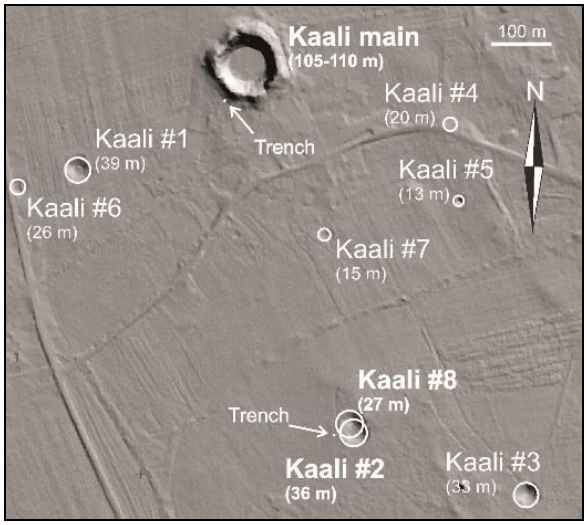

Figure 1: A map of the Kaali strewn field showing locations of two charcoal-containing trenches.

The aim of the current work is to determine the best approach towards analysis of the ^{14}C data of the charcoal found within proximal ejecta of small impact craters, based on comparison of ^{14}C ages obtained from two different structures of the Kaali strewn field.

2. Samples and methods

The first set of samples was collected in 2014 from the 5 m long and up to 1,7 m deep trench within the proximal ejecta of Kaali Main crater (110 m in diameter). They were described in detail, together with their ^{14}C ages, in [8]. The second set of samples was collected in 2016 from a 3 m long and up to 1,4 m deep trench located in the western side of the

proximal ejecta of the two partially overlaping craters: no. 2 (36 m in diameter) and 8 (27 m in diameter). The position of the trench was selected so that ejecta from both craters was expected to be encountered.

All ^{14}C dating was performed at the Vienna Environmental Research Accelerator at the University of Vienna (Austria). A description of the standard analytical method used at VERA is available in [9]. The calibrated ages (95,4% probability) are calculated using the IntCal13 atmospheric curve [10] and the calibration program OxCal v4.2.4 [11].

3. Results

We dated one sample from the Kaali double crater 2/8 (Kaali2-8_1_26). The analysis was performed twice, once using the standard ^{14}C acid-base-acid sample preparation method (lab number: VERA-6362), and once using a slightly modified version with 2xHCl step before NaOH and final HCl treatment (same as in [8] publication, VERA-6362). Both provided identical results (within error): 3036±36 ^{14}C yr BP (1410-1130 cal. BCE) and 3085±35 ^{14}C yr BP (1430-1260 cal. BCE).

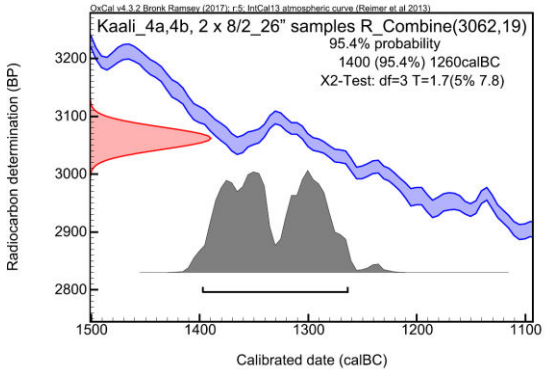

Figure 1: A plot showing an improved, calibrated age of Kaali strewn field based on new dating of sample from Kaali 2/8 craters.

4. Discussion and Conclusions

The age of the sample Kaali2-8_1_26 is 100-200 years younger than the age of Kaali Main defined as the age of the Kaali strewn field in [8] of 1530-1450 cal. BCE. This age was based on 11 different samples of charcoal spread out at a distance of couple of meters within the trench and being characterized by the same age (within error). In the data set from 2014 field season there were also two samples (4,4a and 4,4b) that were a couple hundred years younger than the rest. We previously interpreted them as somehow corrupted either in the field or – more unlikely - in the laboratory. However, the new results showed that both age estimations of Kaali2-8_1_26 are the same (within error) as samples Kaali 4,4a and Kaali 4,4b [8].

We suggest that the real age of Kaali impact event is 100-200 years younger than proposed in [8] and was formed 3062±19 ^{14}C yr BP or 1400-1260 cal. BCE (age formed by combining Kaali 4,4a, 4,4b, and both Kaali2-8_1_26 measurements). This shows that when determining the age of the impact crater, based on charcoal pieces found within its proximal ejecta: 1) when possible, it is better to base the age estimate on samples from more than one crater from the strewn field; 2) the youngest reasonable samples should be used (but obviously ones that are younger than the oldest sediment within the structure should be excluded. This allows to limit the influence of the "old wood problem" on age estimation of small impact craters.

Acknowledgements

Support for this study was provided by the Barringer Family Fund for Meteorite Impact Research in 2016 and NCN grant to AL (UMO-2013/08 /S/ST10/00586), as well as project "Kaali" founded by the Institute of Geological Sciences Polish Academy of Sciences. Work by AJ and JP is supported by the Institutional Research Funding Program (IUT20-34).

References

[1] Wartho et al. 2011 MAPS:A247. [2] Folco et al. 2011. Geology 39:179–182. [3] Jourdan et al. 2012. Elements 8:49–53. [4] Gurov and Gurova 1998. Planetary and Space Science 46:323–328. [5] Stankowski et al. 2002. Proceedings of the Estonian Academy of Sciences, Geology 51:227–240. [6] Herd et al. 2008. Geology 36:955–958. [7] Pessenda et al. 2001. Radiocarbon 43:595–601. [8] Losiak et al. 2016. MAPS 51:681–695. [9] Wild et al. 2013. Radiocarbon 55:599–607. [10] Reimer et al. Radiocarbon 55:1869–1887. [11] Ramsey and Lee 2013. Radiocarbon 55:720–730.

EPSC Abstracts
Vol. 12, EPSC2018-265, 2018
European Planetary Science Congress 2018

Constraining shock wave propagation direction from planar microstructures in quartz and feldspar

L. Pittarello (1), L. Ferrière (2), G. R. Osinski (3)
(1) University of Vienna, Austria, (2) Natural History Museum, Vienna, Austria, (3) University of Western Ontario, London, Ontario, Canada (e-mail: lidia.pittarello@univie.ac.at)

Abstract

Shock effects in minerals are heterogeneously distributed in impactites, both in intensity and frequency. However, specific crystallographic directions within minerals might be favored in developing shock-induced planar microstructures depending on their orientation with respect to the shock wave propagation. The occurrence of this relation is here proved by microstructural measurements on selected samples from terrestrial impact structures. Samples containing shocked minerals at a close distance from shatter cone striation, which permits to infer the main shock wave propagation direction, were selected. The information on shock wave propagation direction inferred from shock-induced microstructure distribution may contribute to a better understanding of impact cratering processes in general.

1. Introduction

Local shock wave scattering induced by discontinuities (e.g., mineral grain boundaries, cooling joints, inclusions, etc.) results in heterogenous distribution of shock effects in impactites. The crystallographic orientation of mineral grains can also affect the response to shock metamorphism, such as that even an apparently homogenous quartzite contain uneven frequency distribution of planar deformation features (PDFs) in quartz crystals. However, the relation between the shock wave propagation direction and the orientation of shock features at the bulk rock scale has never been investigated in detailed. Statistical measurements of PDFs in quartz are commonly used as shock barometer [1], with pressure values derived from shock recovery experiments on single crystal. This method provides reliable values only in first approximation when applied in polymineralic rocks, as the interaction between shock waves and crystals of different internal symmetry and orientation might affect the shock intensity recorded in individual phases. Nevertheless, shock pressure values obtained with this method have proven to be useful in shock attenuation studies (e.g., [2]). To address the influence of shock wave propagation direction in the development of shock features, we have investigated the orientation of shock-induced planar microstructures in quartz and feldspar grains in shatter cone sample formed in variously deformed granitoids from different terrestrial impact structures. The clear preferred orientation of the measured microstructures provides indication on the shock wave propagation direction across the different samples.

2. Methods

Shatter cones formed in granitoids recording different pre-impact tectonic deformation stages, from undeformed to strongly foliated, have been selected from Charlevoix (Canada); [3]), Keurusselkä (Finland; [4]), and Manicouagan (Canada; [5]) impact structures. Thin sections were cut normal to shatter cone surface and striation. Planar microstructures, such as PDFs in quartz, planar fractures (PFs), PDFs, and (likely shock-induced) micro-twins in feldspar [6] were measured with the Universal-stage and plotted with the program Stereo32, using as reference either the foliation (whenever present) or the long side of the thin section. For convention, the *z* direction is normal to the stereoplot and is parallel to the shatter cone striation, *x* is horizontal and sub-parallel to the shatter cone surface, and *y* is vertical (N-S). For quartz containing PDFs, the c-axis orientation was also plotted, to exclude any bias caused by pre-impact dynamic recrystallization.

3. Results

The sample from Manicouagan (WMM-102A-64C1) consists of a weakly foliated, garnet-bearing metagranite, dominated by shocked oligoclase and a few shocked quartz grains with mainly basal PDFs. Shock features in oligoclase include micro-twinning and PDFs, forming a dense network of planar microstructures. Measurements along a transect

normal to the shatter cone surface show that these planar microstructures are spread in any *x*-*y* direction but sub-parallel to *z* (Fig. 1). The sample from Charlevoix (CHA09-12-01) consists of an undeformed granitoid, mainly containing quartz, plagioclase, hornblende, and opaque minerals. Quartz exhibits up to three PDF sets and plagioclase PFs and microtwins, with local occurrence of possible PDFs. All these planar microstructures insist on planes sub-parallel to *z* (Fig. 1), whereas quartz containing PDFs shows random orientation of the c-axis for *x* and *y*, but normal to *z*. The sample from Keurusselkä (VN3) consists of a strongly foliated gneiss, with elongated quartz ribbons, sub-rounded sericitized feldspar, and partially chloritized biotite layers. Quartz grains larger than 50 µm locally contain decorated PDFs. A few feldspar grains in the groundmass exhibit micro-twinning. Despite the extended dynamic recrystallization, large quartz grains show no crystallographic preferred orientation, but those that contain PDFs have c-axis normal to *z*. Both PDFs in quartz and microtwins in feldspar develop along crystallographic planes sub-parallel to *z*. Generally, no apparent influence of the tectonic deformation history of the rocks could be observed, except for a very weak asymmetry of quartz c-axis orientation in the strongly foliated sample.

4. Discussion and conclusions

Although the formation mechanism of shatter cones is still debated [7], we can assume that the shatter cone striation represents the local propagation direction of the scattered shocked waves. Shock pulse duration is too short to determine changes in the crystallographic preferred orientation of minerals, but those with crystallographic orientation favorably oriented with respect to the shock wave propagation direction will more likely develop planar microstructures. Preliminary results in this work show that both planar microstructures in feldspar and PDFs in quartz preferentially form along crystallographic directions that are sub-parallel to the supposed shock wave propagation direction, whereas quartz grains with c-axis lying on the surface normal to the local shock wave propagation direction generally contain PDFs. Thus, the crystallographic orientation of minerals with respect to the shock wave propagation does affect the intensity and the type of shock effects. Whenever the shock wave propagation direction cannot be inferred from other features, it can be constrained by the preferred orientation of planar microstructures in feldspar and quartz grains. Further systematical work to confirm these preliminary results is currently in progress on oriented drill core samples.

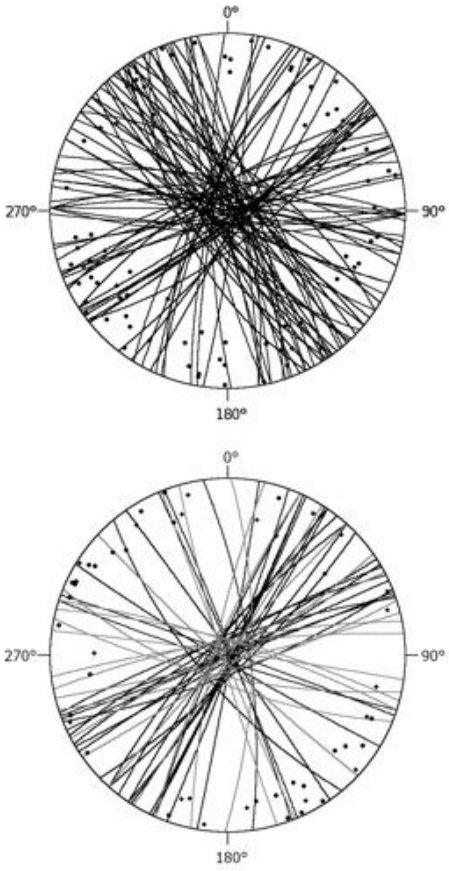

Figure 1: Stereoplot showing the poles and the corresponding great circle for 84 planar microstructures in plagioclase in the sample from Manicouagan impact structure (upper plot) and for 30 planar microstructures in plagioclase (dots and black lines) and 19 PDF sets in quartz (diamonds and gray lines) in the sample from Charlevoix impact structure. Equal angle, lower hemisphere.

References and acknowledgments

L.P. is supported by the Austrian Science Fund (FWF), project V505-N29.

[1] von Engelhardt W. & Bertsch W. 1969, Contrib Mineral Petr 20:203–234. [2] Ferrière L. et al. 2008, Science 322:1678-1681. [3] Robertson P.B. 1975, Bull Geol Soc Am 86:1630-1638. [4] Ferrière L. et al. 2010, Meteorit Planet Sci 45:434-446. [5] Spray J. G. et al. 2010, Planet Space Sci 58:538-551. [6] Pickersgill A.E. et al. 2015, Meteorit Planet Sci 50:1546-1561. [7] Baratoux D. & Reimold W.U. 2016, Meteorit Planet Sci 51:1389-1434.

EPSC Abstracts
Vol. 12, EPSC2018-292, 2018
European Planetary Science Congress 2018

Combined remote sensing analyses and landscape evolution modeling of the terrestrial Bosumtwi crater

G. Wulf (1), S. Hergarten (2), T. Kenkmann (1)
(1) Institute of Earth and Environmental Sciences (Geology), Albert-Ludwigs-University Freiburg, Germany, (2) Institute of Earth and Environmental Sciences (Near-Surface Geophysics), Albert-Ludwigs-University Freiburg, Germany. (gerwin.wulf@geologie.uni-freiburg.de)

Abstract

Based upon the terrestrial Bosumtwi crater, we get new insights into the impact crater formation process by combining remote sensing and geomorphological analyses with landscape evolution models. We prove whether the current morphology of Bosumtwi crater can be the result of erosion of a typical Martian-type or lunar-type impact crater. We suggest that a fluidized ejecta blanket with circumferential rampart lobes surrounded the pristine Bosumtwi crater and that the current morphology is the result of a weakly eroded ejecta rampart.

1. Introduction

The Bosumtwi impact crater in Ghana (06°30`N, 01°25`W) is one of the youngest and best preserved terrestrial impact craters [1]. The 1.07 Ma old impact structure has a pronounced crater rim with a diameter of 10.5 km [2]. A striking feature of the Bosumtwi impact structure is a shallow, annular moat at 7-8.5 km from the crater center directly beyond the crater rim, surrounded by a concentric topographic high at 18-20 km radial distance from the impact center [3, 4, 5]. It was suggested that preferential removal of impact ejecta could be the reason for this shallow annular depression [5]. Other explanations included an original depositional pattern as well as impact-induced concentric fracturing as causes for this annular moat [3]. Here we present preliminary results of remote sensing analyses and landscape evolution modeling and hypothesize that the peripheral morphology of Bosumtwi crater results from a fluidized ejecta blanket with rampart structure similar to Martian DLE craters.

2. Methods

We used digital elevation data from the TanDEM-X mission (TerraSAR-X add-on for Digital Elevation Measurements) with a mesh width of 0.4 arc-second (~12 m at the equator) as base data to create a DEM mosaic of the Bosumtwi crater and the surrounding area. A stream network was delineated and watersheds and catchment areas were determined by combining the derived flow directions with defined outlet points of the watersheds. We compared the results of the Bosumtwi crater with a Martian rampart crater of similar size. The Martian crater Steinheim (190.65°E 54.57°N), a well-preserved and young 11.2 km diameter double-layered ejecta (DLE) [6], was selected. We used the Ames Stereo Pipeline to build a high-resolution digital elevation model [7]. A hypothetical drainage network and catchment areas were derived using the same approach as for Bosumtwi crater. In order to test the hypothesis whether the current morphology of Bosumtwi crater can be the result of erosion of a Martian-type or lunar-type impact crater we used landscape evolution modeling on the basis of DEMs. The main approach hereby is to use the current morphology of fresh Martian and lunar impact craters as starting point for the erosion modeling. The model combines the stream power approach for fluvial incision with a linear diffusion equation mimicking hillslope processes. The stream power approach dates back to empirical studies of Hack (1957) and Flint (1974) and is used in all contemporary large-scale models of fluvial erosion. The diffusion equation was introduced in the context of landform evolution by Culling (1960). Both processes can be summarized in a parabolic differential equation, as reviewed by Robl et al. (2017).

3. Results

The drainage network of Bosumtwi crater forms a circular pattern in the slightly depressed annular zone beyond the crater rim. Consequently, the crater rim and the crest line of the morphological ring are building concentrically oriented watersheds over more than 80% of the impact structure (Fig. 1).

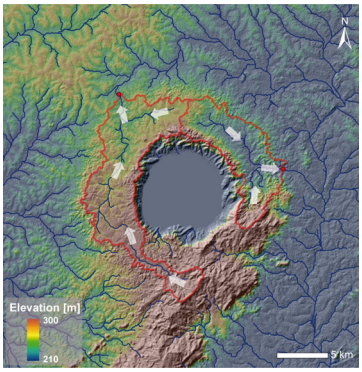

Figure 1: Derived drainage pattern and accordant catchment areas for Bosumtwi crater.

To test the hypothesis that the morphological ring of Bosumtwi crater is the result of partly eroded ejecta deposits, we used landscape evolution modeling on the basis of typical Martian (Steinheim) and lunar (Harpalus) impact craters. In the process, we derived surface models after an assumed erosion period of 1 Ma, comparable to the current age of Bosumtwi (1.07 Ma). The drainage pattern of Steinheim crater shows a local watershed along the crest line of the rampart and a concentric discharge pattern in the moat area (Fig. 2 a,b), comparable to Bosumtwi crater. The modeling results clearly show that a lunar-like impact crater, represented by Harpalus crater, generates mainly radially oriented drainage networks (Fig. 2 c,d). Neither an annular depression beyond the crater rim nor a concentric morphological ring is recognizable in the initial state as well as the eroded states of the impact crater.

4. Summary and Conclusions

With the help of landscape evolution modeling it could be demonstrated that the current morphology of the terrestrial Bosumtwi crater cannot be explained by erosional processes of a lunar-like impact crater. Instead, our results show that the morphological and spectral characteristics of Bosumtwi crater possess striking similarities to those of Martian rampart craters, especially to DLE craters. We therefore suggest that Bosumtwi crater was originally built as a Mars-like rampart crater and as a consequence that the current morphology is the result of a weakly eroded ejecta rampart.

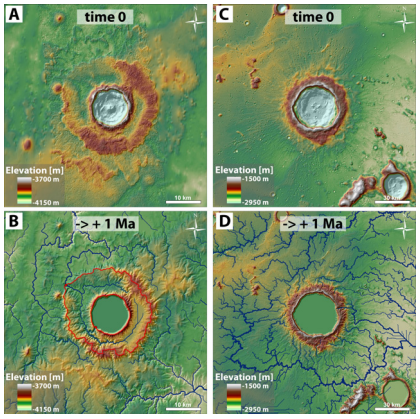

Figure 2: Landscape evolution modeling results for a typical Martian (Steinheim, A/B) and lunar (Harpalus, C/D) impact crater.

References

[1] Koeberl, C. and Reimold, W.U.: Jahrbuch der Geologischen Bundesanstalt, vol. 145, pp. 31–70, 2005.

[2] Koeberl, C. et al.: Geochim. Cosmochim. Acta, vol. 61, pp. 1745–1772, 1997.

[3] Reimold, W.U. and Koeberl, C.: Journal of African Earth Sciences, vol. 93, pp. 57-175, 2014.

[4] Jones, W.B. et al.: Ghana. Geol. Soc. Am. Bull., vol. 92, pp. 342–349, 1981.

[5] Wagner, R. et al.: In Meteorite Impacts in Precambrian Shields. Impact Studies, vol. 2: Plado, J., Pesonen, L.J. (Eds.), Springer, Berlin, Heidelberg, pp. 189–210, 2002.

[6] Wulf G. and Kenkmann T.: Meteoritics & Planetary Science, vol. 50, pp. 173–203, 2015.

[7] Moratto Z.M. et al.: 41st Lunar and Planetary Science Conference, abstract #2364, 2010.

[8] Hack, J.T.: USGS Professional Paper 294B, 45–97, 1957.

[9] Flint, J.J.: Water Resour. Res. 10, 969–973, 1974.

[10] Culling, W.E.H.: J. Geol. 68, 336–344, 1960.

[11] Robl, J., Hergarten, S., Prasicek, G.: Earth-Science Rev. 168, 190–217, 2017.

EPSC Abstracts
Vol. 12, EPSC2018-299, 2018
European Planetary Science Congress 2018

Impact flashes on the Moon.

C. Avdellidou (1,2)
(1) Science Support Office, Directorate of Science, European Space Research and Technology Centre (ESA/ESTEC), The Netherlands, (2) Laboratoire Lagrange, Observatoire de la Côte d'Azur, Nice, France (chavdell@gmail.com)

Abstract

Using telescopic observations in R and I band, for a first time impact flash temperatures are derived. Flash temperatures can now be used to calculate, with better accuracy, the luminous energy of the events. The masses are found to range between a few grams to kilograms and the derived sizes are just a few centimetres.

1. Introduction

The idea to monitor the lunar surface using photomultipliers was already introduced since the beginning of 90s, when it was modelled that impact flash events can be recorded on the lunar surface using modest telescopes [1]. However, it was not until the 2000 when the first impact flash was recorded [2]. The initial purpose of this research was to measure the flux of impactors on Earth. The advantage is that the lunar surface provides an extended area for numerous detections, whereas the Earth-based sky monitoring systems searching for bolides does not have such a large detection area. Additionally, the Moon represents a better impact target as it lacks atmosphere, therefore an impact occurs without the influence and the filter of an atmospheric medium. Several surveys have been started monitoring the lunar surface, however all are equipped with one camera detector operating in the visible wavelength [3]. Here, will be presented the analysis of observations that were performed for a first time in two different wavelengths, in the framework of NELIOTA project.

2. Data

The project up to now has released 33 publicly available validated flashes. The link of an impact event with a specific meteor shower or the sporadic population has a fundamental role in the further analysis of the impact characteristics. The assumption of the impact speed, together with the measurement of the flash temperature, is essential in the calculation of the mass of the impacting body and, moreover, the assignment to a meteor shower (or not) provides an estimate of the impactor's bulk density which enables the calculation of their sizes.

3. Method and Results

Here is followed a numerical way, advanced from the previous version [4], to calculate the temperatures of the impact flashes which were observed in two different wavelength ranges, under the assumption that it is a black body radiation. The theoretical expression of the colour index $R-I$ of a flash is given by:

$$R-I = 2.5log\frac{F_I(T)}{F_R(T)} \quad (1)$$

where the fluxes $F_I(T)$ and $F_R(T)$ are calculated using:

$$F(T) = \frac{\int_{\lambda_1}^{\lambda_2} B(\lambda,T)f(\lambda)d\lambda}{\int_{\lambda_1}^{\lambda_2} f(\lambda)d\lambda} \quad (2)$$

where λ_1 and λ_2 the initial and final transmitted wavelength from each system and $f(\lambda)$ the filter response curve for a wavelength λ as it is provided by the quality tests. The calculated temperatures range between 1,770 and 3,730 K which is in agreement with the aforementioned estimated range for the Moon between the melting point of the lunar regolith at 1,725 K and the vaporization at 3,776 K [5].

Assuming that the impact flash forms a spherical surface, the photon flux f that is received at the telescope corresponds to the radiation of a projected area. The radius r of the radiating area can be easily then calculated from:

$$f = \frac{B(\lambda,T)\epsilon\pi r^2}{D^2} \quad (3)$$

where D the Earth-Moon distance when the flash was recorded and $\epsilon = 1$ the emissivity assuming, as a first

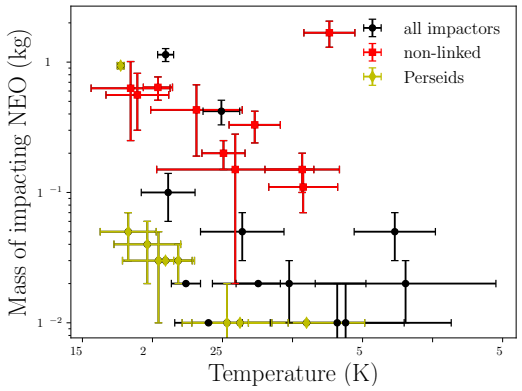

Figure 1: For a given mass of the impactors the temperature appears to have a large dispersion in values and therefore there is no obvious correlation. However, for a given impact speed and material density there is an anti-correlation between temperature and mass.

approximation, a black body radiation. During the partitioning of the impactor's kinetic energy, KE, a fraction η (luminous efficiency) is transformed to luminous energy L. With the help of the measured T, L is estimated and thus the impactor's mass is derived from the KE. Masses are found to be between a few grams and a few kilograms and are strongly affected by the selection of η, by an order of magnitude.

Having a measurement for the impacting mass and assuming spherical-shaped objects it is also possible to estimate their size. The important parameter in this calculation is the choice of the impactor's bulk density which is determined by the origin of the impactor. In our sample the bulk densities are 0.9-2.9 g/cc. The combination of the derived mass with the appropriate density results in small impactor sizes which are between 1-15 cm.

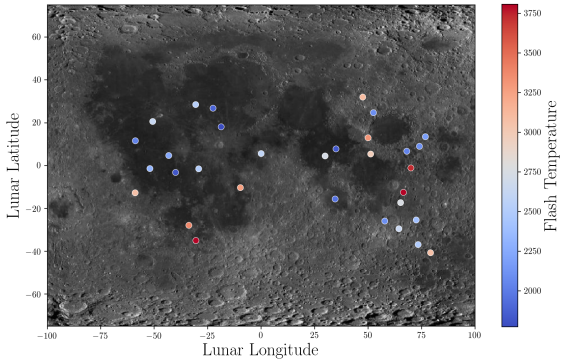

Figure 2: Locations where the impact flashes were detected along with the measured temperature.

References

[1] Melosh H. J., Artemjeva N. A., Golub A. P., Nemchinov I. V., Shuvalov V. V., Trubetskaya I. A.: Remote visual detection of impacts on the lunar surface, Lunar and Planetary Science Conference, 1993.

[2] Ortiz, J. L., Sada, P. V., Bellot Rubio, L. R., Aceituno, F. J., Aceituno, J., Gutierrez, P. J., Thiele, U.: Optical detection of meteoroidal impacts on the Moon, Nature, 405, 921, 2000

[3] Suggs, R. M., Moser, D. E., Cooke, W. J., and Suggs, R. J.: The flux of kilogram-sized meteoroids from lunar impact monitoring, Icarus 238, Supplement C, pp. 23–36, 2014.

[4] Bonanos, A. Z., Avdellidou, C., Liakos, A., Xilouris, E.M., Dapergolas, A., Koschny, D., Bellas-Velidis, I., Boumis, P., Charmandaris, V., Fytsilis, A., Maroussis, A.: NELIOTA: First Temperature Measurement of Lunar Impact Flashes, A&A, 612, 2018.

[5] Cintala, M.: Impact-Induced Thermal Effects in the Lunar and Mercurian Regoliths, Journal of Geophysical Research, vol. 97, p. 947-973, 1992.

EPSC Abstracts
Vol. 12, EPSC2018-316-2, 2018
European Planetary Science Congress 2018

(S)TEM analysis of quartz-coesite relations in impact ejecta from the Australasian tektite strewn field

Fabrizio Campanale (1) (fabrizio.campanale2@gmail.com), Enrico Mugnaioli (2), Mauro Gemmi (2), Martin R. Lee (3), Billy P. Glass (4) and Luigi Folco (1)

(1) Dipartimento di Scienze della Terra, Università di Pisa, Italy (2) Center for Nanotechnology Innovation@NEST, Pisa, Italy (3) Department of Geographical and Earth Sciences, University of Glasgow, UK (4) Department of Geosciences, University of Delaware, Newark, DE, USA

Abstract

Scanning and transmission electron microscopy observations on shocked silica mineral grains from the Australasian tektite/microtektite strewn field suggest that coesite crystals form directly in contact with quartz grains through a subsolidus reconstructive transformation. This finding is in contrast with the current mainstream view, which considers coesite as the product of a rapid crystallization from a dense silica melt or glass during shock unloading.

1. Introduction

Quartz is one of the most common mineral in Earth's continental crust. The study of shock metamorphic features in quartz and its shock induced silica polymorphs, i.e., coesite and stishovite, is thus relevant for defining the physical conditions attained during the majority of hypervelocity impacts of cometary or asteroidal bodies on Earth.
In endogenic geological processes, which typically involve equilibrium reactions and time-frames from years to thousands of years, coesite forms from quartz at pressures between ~3 and ~10 GPa. In impactites, coesite is preserved as a metastable phase in non-porous crystalline rocks that experienced peak shock pressures above ~30-40 GPa [*e.g.* 1], and in porous sedimentary rocks shocked at pressures as low as ~10 GPa [2]. There is however a general consensus that the characteristic twinned impact coesite [3] is the result of crystallisation from a dense amorphous phase, either from a silica shock melt [*e.g.* 1, 4] or from a highly densified diaplectic silica glass [5], during shock unloading, when the pressure release path passes through the coesite stability field.
Conversely, we show here STEM and TEM/EDT evidence of direct quartz-to-coesite transformation in microscopic shocked coesite-bearing quartz ejecta from the Australasian tektite/microtektite strewn field - the largest (~15% of Earth's surface) and the youngest one (~0.8 Myr old) on Earth.

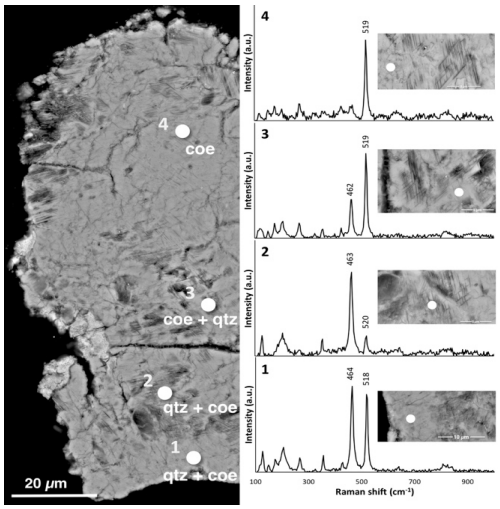

Figure 1: Microscopic shocked ejecta composed by coesite and PDF-bearing quartz.

2. Samples and methods

The samples studied in this work consist of ~400 μm in size shocked silica ejecta found in the Australasian microtektite layer from two cores located within 2000 km from a hypothetical impact location in Indochina (~17°N, 107°E). They were first studied with field emission gun - scanning electron microscopy (FEG-SEM) and Raman spectroscopy. Then, electron-transparent thin sections were prepared for transmission electron microscopy (TEM) and scanning-TEM (STEM) using focused ion beam (FIB) micromachining. Additionally, electron diffraction

tomography (EDT) and ASTAR (EBSD-like) analyses via (S)TEM are currently in progress.

3. Results and discussion

FEG-SEM coupled with μRaman analyses revealed that shocked silica grains are composed by coesite including domains of quartz, with at least two diffuse cross-cutting sets of planar deformation features (PDFs) (Fig. 1).

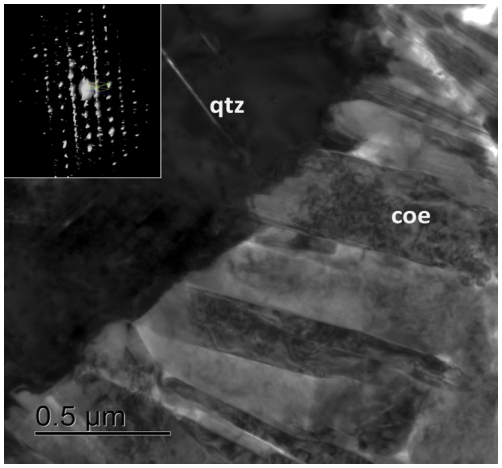

Figure 2: TEM image showing twinned elongated coesite grains growing at the expense of a single quartz grain. Inset: typical 3D diffraction pattern of a twinned coesite along 111.

The direct quartz-coesite contact is apparent at the nanometer scale (Fig. 2). Several intensely twinned coesite grains nucleate and grow without a specific orientation (EDT and ASTAR data) at the expense of quartz. This is strong evidence of direct quartz-to-coesite subsolidus transformation in contrast to what has been suggested for impact-produced coesite in crystalline targets [*e.g.* 1, 4, 5].
The ongoing investigation of key features like the quartz-coesite mutual crystallographic orientations and the twinning in coesite is expected to provide clues for better understanding formation mechanisms and the kinetic of impact-produced coesite - a crucial issue for the correct definition of P-T-t shock metamorphic conditions in impactites.

4. Conclusion

The shocked coesite-bearing quartz grains studied in this work represent an excellent opportunity to investigate the mechanism and the kinetics of the direct subsolidus quartz-to-coesite transformation in shock metamorphic events. Supposedly this could be the dominant mechanism of coesite formation in porous quartz-bearing target rocks, like at Barringer [5] and Kamil craters [6].

References

[1] Stöffler, D., and Langenhorst, F.: Shock metamorphism of quartz in nature and experiment: I. Basic observation and theory, Meteoritics and Planetary Science, v. 29, p. 155-181, 1994.

[2] Kowitz, A., Güldemeister N., Schmitt, R.T., Reimold W-U., Wünnemann, K., and Holzwarth A.: Revision and recalibration of existing shock classifications for quartzose rocks using low-shock pressure (2.5–20 GPa) recovery experiments and mesoscale numerical modeling: Meteoritics and Planetary Science, v. 51, p. 1741-1761, 2016.

[3] Bourret, A., Hinze, E., Hochheimer, H. D.: Twin structure in coesite studied by high resolution electron microscopy, Physics and Chemistry of Minerals, v. 13, p. 206-212, 1986.

[4] Fazio, A., Mansfeld, U., and Langenhorst F.: Coesite in suevite from the Ries impact structure (Germany): from formation to postshock evolution, Meteoritics and Planetary Science, v. 52, p. 1437-1448, 2017.

[5] Stäle, V., Altherr, R., Koch, M., Nasdala, L.: Shock-induced growth and metastability of stishovite and coesite in lithic clasts from suevite of the Ries impact crater (Germany), Contributions to Mineralogy and Petrology, v. 155, p. 457-472, 2008.

[5] Kieffer, S. W., Phakey, P. P. and Christie, J. M.: Shock processes in porous quartzite: Transmission electron microscope observations and theory, Contribution to Mineralogy and Petrology, v. 59, p. 41-93, 1976.

[6] Folco, L., Mugnaioli, E., Gemelli, M., Masotta, M., Campanale, F.: Direct quartz-coesite transformation in shocked porous sandstones from Kamil crater (Egypt), Geology (under review), 2018.

EPSC Abstracts
Vol. 12, EPSC2018-327, 2018
European Planetary Science Congress 2018

Sulfide globules in Muong Nong-type tektites from Laos

Šárka Křížová (1,2), Roman Skála (1,2), Lukáš Ackerman (1), Karel Žák (1) and Tomáš Magna (3)
(1) The Czech Academy of Sciences, Institute of Geology, Rozvojová 269, CZ-165 00, Prague 6, Czech Republic (2) Institute of Geochemistry, Mineralogy and Mineral Resources, Faculty of Science, Charles University, Albertov 6, 128 43 Prague 2, Czech Republic (3) Czech Geological Survey, Klárov 3, CZ-118 21 Prague 1, Czech Republic; (krizova@gli.cas.cz)

1. Introduction

Muong Nong-type (MN-type) Australasian tektites have blocky, layered structures, larger sizes and petrographic evidence indicates a lower temperature origin than envisaged for other tektites [e.g., 1–3]. Their largest known examples are known from Laos, Thailand, Cambodia and the Hainan Island (China) within the Australasian tektite (AAT) strewn field. Microinclusions in tektites may provide invaluable information about the nature of their formation, but can also shed some light on the type of impactor. Coesite, corundum, [e.g., 1, 4] zircon, reidite and ZrO_2 inclusions [e.g., 5] were described from the MN-type tektites. However, as far as we aware, sulfide microinclusions in MN-type tektites have not been observed previously.

2. Materials and methods

Forty-nine polished thin sections from 31 samples of AA tektites sampled in Laos were studied in detail by optical (transmitted and reflected light) and electron microscopy (BSE). Major element compositions of tektites and sulfide inclusions were determined using EPMA. The inclusions were also investigated by Raman microspectroscopy.

3. Results

Rare round-shaped sulfidic spherules with a diameter of ca. <5–20 μm occur in tektite glass domains with numerous small vesicles. Sulfide inclusions were found in several tektite fragments from the same locality possibly belonging to a single larger tektite body. Along the perimeter of the inclusions, there are sometimes cracks but no radial fractures have been observed, whereas within the inclusions, many irregular internal cracks and bubbles occur. The chemical composition of the sulfide blebs is heterogeneous, but their chemical composition determined by EPMA analysis corresponds to phases of Fe-Ni-S ternary system with subordinate amounts of Cu and Co.

4. Discussion

The BSE images reveal that the spherules are inhomogeneous and some display the features, which can be ascribed to the unmixed monosulfide solid solution/intermediate solid solution (Fig. 1). This is confirmed by the different Raman spectra measured at different places within a single spherule. The glass with the direct contact with sulfide blebs is not enriched in any of the elements found in spherules and is chemically identical to the composition of glass more distant from inclusions. In the same samples where the sulfide inclusions were found, the presence of coesite was revealed by Raman microspectroscopy. Coesite as the high-pressure silica polymorph, has been previously reported from AA tektites and microtektites [e.g., 6].

A plausible scenario for the origin of sulfides is that during tektite formation, under high temperature and pressure conditions at extremely low oxygen fugacities (i.e., in highly reducing environment) followed by subsequent rapid cooling, the sulfur-rich droplets of melt were separated from the silicate-rich glass to form an immiscible sulfide melt/liquid that was immediately encapsulated in a silicate glass matrix. Another possible origin of these sulfidic blebs may potentially be tracked back to the sulfidic phases that were originally present in the target materials parental to AAT.

5. Summary and Conclusions

Since these sulfide inclusions are deeply included within the tektite glass, they do not show signs of elemental transfer with the outside environment. Consequently, they can preserve their original

composition reflecting the state at which they were entrapped. The question remains on the origin of the sulfide inclusions. The blebs can be derived from a wide range of the assumed target rocks or can bear an extraterrestrial component of a projectile. Indeed, because the spherules contain Ni and minor amounts of Co and Cu, it is probable that this can be a captured meteoritic component. Resolving of this issue will be the subject of further study.

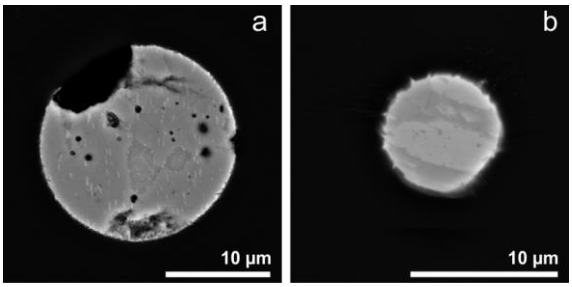

Figure 1: BSE images of typical sulfide blebs hosted by Muong Nong-type AA tektites

Acknowledgements

This research was funded by the Czech Science Foundation project 17-27099S and conducted within the institutional support RVO 67985831 of the Institute of Geology of the Czech Academy of Sciences.

References

[1] Glass B. P. and Barlow R. A.: Mineral inclusions in Muong Nong-type indochinites: Implications concerning parent material and process of formation. Meteoritics, Vol. 14, pp. 55-67, 1979.

[2] Barnes V. E.: Origin of tektites. Texas Journal of Science, Vol. 41, pp. 5-33, 1989.

[3] Koeberl C.: Geochemistry and origin of Muong Nong-type tektites. Geochimica et Cosmochimica Acta, Vol. 56, pp. 1033-1064, 1992.

[4] Walter, L.S.: Coesite discovered in tektites. Science, Vol. 147, pp. 1029-1032, 1965.

[5] Cavosie A. J., Timms N. E., Erickson T. M. and Koeberl C.: New clues from Earth's most elusive impact crater: Evidence of reidite in Australasian tektites from Thailand. Geology, Vol. 46, pp. 203-206, 2018.

[6] Glass B. P. and Wu J.: Coesite and shocked quartz discovered in the Australasian and North American microtektite layers. Geology, Vol. 21, pp. 435-438, 1993.

EPSC Abstracts
Vol. 12, EPSC2018-709-1, 2018
European Planetary Science Congress 2018

Spherical shock experiments with Chelyabinsk meteorite: the experiment and textural gradient

Evgeniya V. Petrova (1), Victor I. Grokhovsky (1), Tomas Kohout (2), Razilia F. Muftakhetdinova (1), and Grigoriy A. Yakovlev (1)
(1) Institute of Physics and Technology, Ural Federal University, Ekaterinburg, Russia (evgeniya.petrova@urfu.ru)
(2) Faculty of Science, University of Helsinki, Finland (tomas.kohout@helsinki.fi)

Abstract

Shock experiment with loading by spherically converted shock waves on the Chelyabinsk meteorite sample was performed. A shock pressure and temperature have been increased from the outer to the inner part of the shocked sphere. As the result, a wide range of textural changes in the material from the surface to the center of the sphere was revealed from the microscopic observations.

1. Introduction

The Chelyabinsk chondrite (fall, 2013, Russia) was classified as LL5 S4 W0. Its complex structure with different lithologies was described before in [1-4]. Light-colored and dark-colored lithologies of Chelyabinsk LL5 are supposed to be of identical LL5 composition mostly [1], but they are slightly different. There are few explanations of different lithologies formation from the initial substance [5].

Different lithologies could be observed in the large samples and in the main mass fragments recovered from Chebarkul Lake. However, small samples mostly possessed a single type of lithology. Relatively large sections (up to the 150 cm^2) of the massive Chelyabinsk meteorite fragments look like impact melt breccia from the impact craters described in [6]. It was supposed that Chelyabinsk meteoroid was formed at the similar mechanism as suevite because it appears as the fragments of the host rock were mixed with the impact melt and were partly re-heated. [5, 7]. In this study, the intensive shock impact on the initial material of the light-colored lithology of Chelyabinsk LL5 meteorite was experimentally performed.

2. Samples and Methods

The method of spherically converging shock waves is a useful technique for modeling of the effect of wide ranges of pressure and temperature on studied materials. Several meteorites (the Saratov chondrite; the Chinga ataxite; Sikhote-Alin octahedrite) were affected by the spherically converging shock waves previously [8, 9]. In the current experiment, the individual fragment with light-colored lithology was used. A sample was prepared in the shape of the sphere of 40 mm in diameter. This sphere was put into vacuumed steel container and loaded by the spherically converted shock waves. Details of the spherical shock experiments were reported in [8]. The peak pressures and temperatures reached in the center of the ball can be estimated to be about 100 GPa and more than 2000°C, respectively. Changes in reflectance spectra of shocked Chelyabinsk LL5 for the four textural zones are presented in [10].

After the shock loading of the ball sample, it was cut in half and then removed from the steel container. The diametric section was polished, while the thin section was prepared from another. An optical observation was performed using AxioVert 40 MAT (Carl Zeiss) and Laboval 2 (Carl Zeiss Jena), electron microscopy was done by using of scanning electron microscope ΣIGMA VP (Carl Zeiss) with an X-max energy dispersive spectroscopy device (Oxford Inst.).

3. Results and Discussion

From the naked eye observation of the diameter section of the experimentally shocked Chelyabinsk sample four visually different zones were distinguished (fig.1 in [10]). Under the microscope, the outer region of the circle section showed light-colored lithology material, which resembles initial material with a number of thick impact veins in the material texture. Some of the troilite inclusions were found partly melted. In the transmitted light weak

mosaicism of olivine grains was noted, that corresponds to the shock stage S4. This zone spreads from the sample edge to the 0.45 of the ball sample radius (R).

The second zone is situated from the 0.45R to the 0.4R. It looks like a dark-colored ring. Moreover, its texture appears to have the same features as found in the dark-colored lithology of Chelyabinsk [4]. For example, troilite melt is filling in small cracks within silicates. There was not found pristine troilite grains in this region, while large metal grains and moderate chromite grains are still present. This zone corresponds to the shock stage S5. Silicate grains have smooth edges and they are almost opaque under the transmitted light microscope.

The third zone is sulfide melt-rich zone corresponds to the S6. It situated from the 0.4 R to 0.25 R. Its texture contains clasts of heated material embedded into the melt, where abundant vesicles with the small metal and troilite particles were observed. A few newly formed silicate crystals were found in this region.

The fours zone is an entirely molten phase in the sample interior, which corresponds to the impact melt. It appears as entirely melted and recrystallized material in the inner region. There are presented newly grown crystals of olivine in the shape of cross-oriented bars, which intersperse with a rich of vesicles glass. New crystals show a sharp extinction in the polarized transmitted light. Several metal-troilite eutectic grains were observed in the central region. Some of them was relatively large. It was noted that every metal+troitite droplet were associated with a vesicle. Only a few small chromite grains were oed in melted material sample center.

4. Summary and Conclusions

A possibility of various lithologies formation in one sample has been demonstrated during converging shock waves experiment. The four visually different zones obtained from the spherical shock experiment on the light-colored lithology of Chelyabinsk LL5 were studied by optical and electron microscopy: shock melt, dark-colored, brighter-dark-colored and light-colored material. All possible higher shock stages were revealed in the experimentally shocked sample: from the S4 of the initial material up to the impact melt, which presented a completely melted material.

Acknowledgements

This work was supported by the Ministry of Education and Science of the Russian Federation (Projects 5.4825.2017/6.7, 5.3451.2017/4.6); the Act 211 of the Government of the Russian Federation, Agr.# 02.A03.21.0006, and the Academy of Finland.

References

[1] Galimov, E.M. et al.: Analytical results for the material of the Chelyabinsk meteorite, Geochemistry International, Vol. 51, pp. 522-539, 2013.

[2] Badyukov D.D. et al.: Chelyabinsk meteorite: Shock metamorphism, black veins and impact melt dikes, and the Hugoniot, Petrology, Vol. 23, pp. 103-115, 2015.

[3] Righter, K. et al.: Mineralogy, petrology, chronology, and exposure history of the Chelyabinsk meteorite and parent body, Meteoritics & Planetary Science, Vol. 50, pp. 1790-1819, 2015.

[4] Kohout, T. et al.: Mineralogy, reflectance spectra, and physical properties of the Chelyabinsk LL5 chondrite – Insight into shock-induced changes in asteroid regoliths, carus, Vol. pp. 228:78-85, 2014.

[5] Petrova E.V. and Grokhovsky V.I.: Impact cratering model of the Chelyabinsk meteoroid formation, 32nd Nordic Geological Winter Meeting, 13-15 January 2016, Helsinki, Finland. pp. 282-283.

[6] Stoffler, D. et al.: Ries crater and suevite revisited—Observations and modeling Part I: Observations, Meteoritics & Planetary Science, Vol. 48, pp. 515-589, 2013.

[7] Trieloff M. et al.: The Chelyabinsk meteorite: Thermal history and variable shock effects recorded by the 40Ar-39Ar system, Meteoritics & Planetary Science, Vol. 53, pp. 343-358, 2018.

[8] Kozlov E.A. et al.: Physical and chemical transformations in Saratov chondrite exposed to spherical shock waves, Physics – Doklady, Vol. 42, No.3. pp. 128-131, 1997.

[9] Grokhovsky V.I. et al.: Shock experiment in spherical waves with iron meteorites, Meteoritics & Planetary Science, Vol. 34, A48, 1999.

[10] Kohout T. et al.: Spherical shock experiments with Chelyabinsk meteorite: reflectance spectra changes with increasing shock, EPSC 2018, 16–21 September 2018, Berlin, Germany, 2018.

EPSC Abstracts
Vol. 12, EPSC2018-755, 2018
European Planetary Science Congress 2018

The South-Pole Aitken basin formation and its effects on the melting activity in the lunar mantle

Sebastiano Padovan (1), Doris Breuer (1), Lukas Manske (2), Elena Martellato (2), Ana-Catalina Plesa (1), Thomas Ruedas (1,2), Sabrina Schwinger (1), and Nicola Tosi (1,3)
(1) Institute of Planetary Research, German Aerospace Center (DLR), Berlin, Germany, (2) Museum für Naturkunde, Berlin, Germany (3) Technische Universität, Berlin, Germany (sebastiano.padovan@dlr.de)

Abstract

Several large lunar impact basins have basaltic infillings, indicating a possible causal link between impacts and subsequent volcanic eruptions [1]. However, the majority of lunar basalts are located in the nearside, in a region known as the Procellarum-KREEP terrane (PKT), an observation explained by invoking the presence of a layer enriched in heat producing elements below or within the crust in the PKT region [2]. Furthermore, the South-Pole Aitken basin (SPA), the largest lunar basin, lacks any significant basaltic infilling. We perform thermal evolution simulations of the Moon that include the effects of the formation of the SPA, and show that any volcanic activity following the formation of a large impact basin depends on the interaction of the impact-induced thermal perturbation with the underlying mantle convection.

1. Introduction

Many large impact basins on the nearside of the Moon are filled with volcanic material that has been emplaced after (in a geological sense) the basins' formation. Thus, these volcanic infillings are not solidified impact melt. This observation led to the hypothesis that large impacts may induce long-term volcanism (e.g., [1]). The causal link between impacts and volcanic activity has been criticised on the basis of numerical models and statistical arguments [3]. However, a recent investigation of the effects of large impacts on the volcanic activity in the mantle of Mercury showed that it is possible to reproduce the observed properties (volume and time of emplacement) of the volcanic infillings of young large basins on the surface of the planet by an impact-induced modification of the melting activity in the mantle [4]. We apply the model developed in [4] to investigate how the formation of large impacts on the Moon may induce and/or modify volcanic activity in the lunar mantle.

2. Methods

2.1. Mantle convection: GAIA

We simulate the thermal evolution of the Moon using the GAIA convection code [5]. We adopt a setup where heat producing elements (HPE) are distributed homogeneously in the mantle and are enriched in the crust (enrichment factor $\Lambda \simeq 15$) and in the KREEP layer ($\Lambda \simeq 350$), a $\sim$ 10-km-thick layer placed under or within the crust in a 40 to 80 degree-wide spherical cap corresponding to the location of the PKT. We track melt production as a function of time and location in order to compare the results with the inferred volume and emplacement history of lunar volcanic units (e.g., [6, 7]). The thermal perturbations caused by large impacts are simulated with iSALE.

2.2. Basin formation: iSALE

Impact simulations are performed with the iSALE shock physics code (e.g., [8]). We assume a 40 km basaltic crust overlying a dunite mantle and an iron core. We use the ANEOS equation of state to describe the thermodynamic behaviour of materials. The mechanical response of the basaltic crust and the dunite mantle under deformation is described by a pressure- and damage-dependent strength model [9], while for the iron core we use the von Mises strength model, more suitable for ductile materials. We also include the Acoustic Fluidization model (e.g., [10]), a transient weakening mechanism required to explain fluid-like behaviour of matter during crater collapse.

3. Results

The adopted distribution of the HPE induces melting activity in the nearside lasting more than a billion years. The stagnant lid, the cold upper layer of the mantle that does not participate in convective motions,

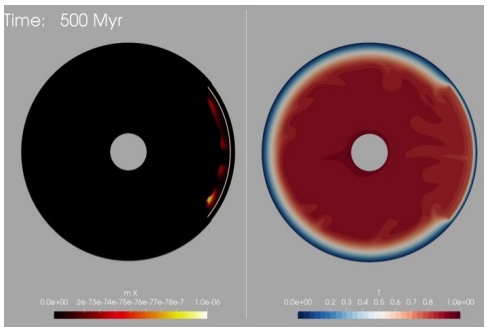

Figure 1: Melting (left) and temperature (right) fields at $t = 500$ Myr in a simulation of the lunar thermal evolution without impacts. The KREEP layer is identified with the thin white line on the right side of the melting field. Color units are dimensionless.

is thinner where the KREEP layer is located. Correspondingly, hot convecting material can reach temperatures locally in excess of the solidus and generate melt (Figure 1). This configuration is consistent with the observation that volcanic provinces are observed mostly on the nearside of the Moon [2].

The 2500-km-wide South-Pole Aitken basin is the largest basin on the Moon. It is located on the farside and shows almost no sign of volcanic activity following its formation, unlike basins on the nearside like Imbrium. We simulated an impact forming an SPA-sized basin and tracked convection and melting activity under the newly formed basin. When the impact occurs away from the KREEP layer the impact-induced thermal perturbation locally thins the stagnant lid, but without producing any post-impact long-term melting activity. This result is a direct consequence of the location of the enriched KREEP layer in our model, which focuses most of the mantle melting activity on the near side.

4. Summary and Conclusions

We investigated the thermal evolution of the Moon in the presence of a layer enriched in heat producing elements (KREEP layer) located under the crust on the nearside. The resulting melting activity is localised on the nearside, consistent with the presence there of the most extensive volcanic units, as already noted in [2]. The formation of an SPA-sized basin does not induce any long-term melting activity in the mantle, as long as it occurs far from the KREEP layer. These results are consistent with the lack of large volcanic units in the SPA basin and support the interpretation of volcanic infillings of large basins as the result of an interaction of the impact-induced thermal anomaly with the convective activity in the mantle [4].

Acknowledgements

Funding from the Helmholtz-Gemeinschaft (project VH-NG-1017) is gratefully acknowledged.

References

[1] Elkins-Tanton, L.T., et al.: Magmatic effects of the lunar late heavy bombardment, Earth Planet. Sci. Lett., Vol. 222, 17-27, 2002.

[2] Laneuville, M., et al.: Asymmetric thermal evolution of the Moon, J. Geophys. Res. Planets, Vol. 118, 1-18, 2013.

[3] Ivanov, B.A. and Melosh, H.J.: Impacts do not initiate volcanic eruptions, Geology, Vol. 31, 869-872, 2003.

[4] Padovan, S., et al.: Impact-induced changes in source depths and volume of magmatism on Mercury and their observational signatures, Nature Comm., 8, 1-10, 2017.

[5] Hüttig, C., Tosi, N., and Moore, W.B.: An improved formulation of the incompressible Navier-Stokes equations with variable viscosity, Phys. Earth Planet. Int., Vol. 220, 11-18, 2013.

[6] Hiesinger, H., et al.: Ages and stratigraphy of lunar mare basalts: A synthesis, doi: 10.1130/2011.2477(01), 2011.

[7] Shearer, C., et al.: Thermal and magmatic evolution of the Moon, Rev. Mineral. Geochem., Vol. 60, 365-518, 2006.

[8] Wünnemann K., et al.: A strain-based porosity model for use in hydrocode simulations of impacts and implications for transient-crater growth in porous targets, Icarus, Vol. 180, 514-527, 2004.

[9] Collins, G.S., et al.: Modeling damage and deformation in impact simulations, Meteorit. Planet. Sci., Vol. 39, 217-231, 2004.

[10] Melosh, H.J., and Ivanov, B.A.: Impact crater collapse, Ann. Rev. Earth Planet. Sci., Vol. 27, 385-415, 1999.

EPSC Abstracts
Vol. 12, EPSC2018-776, 2018
European Planetary Science Congress 2018

Numerical modelling of giant collisions – The Moon-forming impact event

Nicole Güldemeister (1), Lukas Manske (1) and Kai Wünnemann (1,2)
(1) Museum für Naturkunde, Leibniz Institute for Evolution and Biodiversity Science Berlin, Germany (nicole.gueldemeister@mfn-berlin.de), (2) Freie Universität Berlin, Institute for Geological Science, Germany

1. Introduction

Planetary collisions (e.g. the impact of a mars-size object impacting onto proto-earth) play an important role in the evolution of the planetary system. In particular the late phase of planet formation is characterized by collisions of large bodies (giant impact phase). The Moon-forming impact event is thought to be Earth's last giant collision event, marking the end of the accretion of the Earth. This large event (re)set the conditions for the subsequent thermochemical evolution of both bodies, Earth and Moon. Large parts of proto-earth and, presumably, the entire impactor are thought to melt as a consequence of the impact.
To quantify the volume of melt production and to constrain the initial conditions for the subsequent thermochemical evolution of Earth and Moon, we carried out numerical simulations in 2D and 3D of giant collisions including the Moon-forming impact event.

2. Methods

Previously, the Moon-forming giant impact has mostly been modelled with mesh-free so-called smoothed particle hydrodynamics (SPH [1]). In contrast to previous work, we have used an Eulerian shock physics code and fixed grid in space, the two-dimensional (2D) and three-dimensional (3D) iSALE code [2,3,4], to model the giant collision of a mars-sized object with proto-earth. iSALE accounts for multi-material and strength and is expected to provide more accurate results on shock wave propagation. In 2D, we account for a differentiated impactor and target. We assume a structure of the colliding bodies both having a core and mantle. For simplification we neglect the effect of the crust in those models. We take into account an initial thermal profile for the impacted body. The core of both bodies is represented by the Analytical Equation of State (ANEOS, [5]) for iron and the mantle by an ANEOS for dunite. Further, we account for the lithostatic pressure inside the planet as a consequence of the gravitational field using either central or self-gravity. Simulations in 2D allow for self-gravity, which is also planned for 3D in future simulations. In 2D head-on collisions are simulated. In 3D we also carry out a series of oblique impacts with different impact angles. In order to quantify the amount of melt that is produced by such a large impact, we use an approach introduced by [6] calculating the local final temperatures by using the peak shock pressure method. To record the peak pressures we use langrangian tracers.

3. Preliminary Results

Preliminary results carried out in 2D (head-on collisions) with differentiated impactor and target, taking into account self-gravity show that the volume that is fully or partially molten after the impact event is about 4 times the impactor volume.

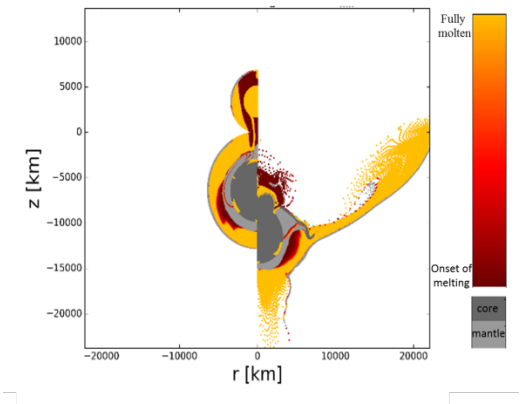

Figure 1: Melt distribution including the degree of melting one hour after the impact. On the left, the used tracers have been mapped back to the initial position. On the right, the final positions of the tracers are shown.

The degree of melt is shown in Figure 1 presenting partially and fully molten areas of the impactor and impacted body. It can be seen that the impactor is completely molten, the iron core of the impacted body is not molten where the entire mantle is almost fully molten. First 3D tests allow for simulations of an oblique impact. Figure 2 shows the temperature and pressure as it develops during a giant collision for an oblique impact of 45 degree angle considering central-gravity where a dunitic impactor strikes a differentiated proto-earth (mantle and core) with an initial temperature profile.

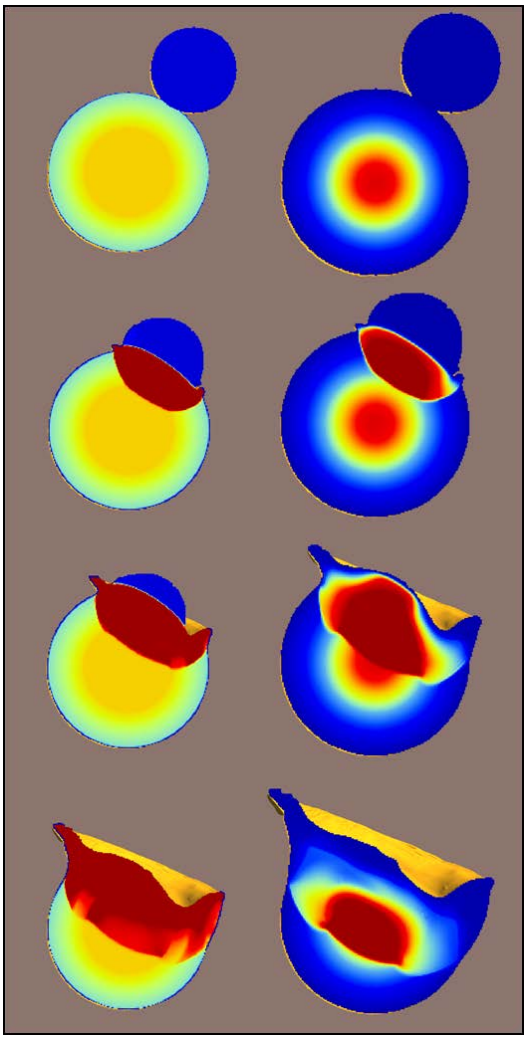

Figure 2: Sequence of the qualitative development of temperature (left) and pressure (right) with time (top to bottom) during a 45 degree impact of a mars-size impactor onto proto-earth with a differentiated target body (mantle and core) and initial temperature profile.

3. Conclusions and Future Work

First numerical simulations of the Moon-forming event in 2D provide estimates about the melt production during such an impact event. First simulations in 3D of oblique impacts show the qualitative distribution of pressure and temperature during the impact event. Future work will include the implementation of a self-gravity routine in iSALE3D incorporating a Barnes and Hut approach [8] similar as in SPH codes. The upcoming simulations will mainly be carried out in 3D to consider more realistic and relevant impact scenarios of the oblique impact of a mars-size object onto proto-earth. In addition we will include differentiated bodies for 3D simulations which will require further code developments. We intend to quantify melt production and to estimate the possible mixing of core material of the impactor with the mantle and core material of the proto-earth.

Acknowledgements

We gratefully thank the iSALE developers, including Gareth Collins, Kai Wünnemann, Dirk Elbeshausen, Boris Ivanov and Jay Melosh. We also thank the Deutsche Forschungsgemeinschaft (SFB-TRR 170, subproject C2 and C4) for funding.

References

[1] Monaghan, J.J.: Smoothed particle hydrodynamics, Annu. Rev. Astron. Astrophys. 30, 543–574, 1992.

[2] Collins, G. S., Melosh, H. J., and Ivanov, B. A.: Modeling damage and deformation in impact simulations. Meteoritics & Planetary Science, 39, 217–231, 2004.

[3] Wünnemann, K., Collins, G. S., and Melosh, H. J.: A strain-based porosity model for use in hydrocode simulations of impacts and implications for transient crater growth in porous targets. Icarus, 180, 514–527, 2006.

[4] Elbeshausen, D.: Dreidimensionale numerische Modellierung schräger Meteoriteneinschläge - Strategien und Anwendungen - Dissertation, Freie Universität Berlin, Fachbereich Geowissenschaften. 283 pages, 2012.

[5] Thompson, S. L.: ANEOS Analytical Equation of State for Shock Physics Codes Input Manual. Technical Report SAND89-2951 UC-404, Sandia National Laboratories.76 pages, 1990.

[6] ManskeL., Wünnemann K., Nakajima M., Plesa A.-C.: Impact-Induced Melting by Giant Impact Events. 49th LPSC, abstact# 2269, 2018.

[7] Barnes, J., Hut, P.: A hierarchical O (N log N) force-calculation algorithm, 1986.

EPSC Abstracts
Vol. 12, EPSC2018-791, 2018
European Planetary Science Congress 2018

Summanen, the twelfth meteorite impact structure in Finland

Lauri J. Pesonen (1), Timmu Kreitsmann (2), Satu Hietala (3), Jouni Lerssi (3) Jari Nenonen (3) and **Jüri Plado** (2)

(1) Solid Earth Geophysics Laboratory, Physics Department, University of Helsinki, Finland (lauri.pesonen@helsinki.fi), (2) Department of Geology, University of Tartu, Estonia (timmu.kreitsmann@ut.ee, juri.plado@ut.ee), (3) Geological Survey of Finland, Kuopio, Finland (satu.hietala@gtk.fi, jouni.lerssi@gtk.fi, jari.nenonen@gtk.fi)

Abstract

The Summanen structure (62°39’00’’N, 25°22’30’’E) is located within the Paleoproterozoic Central Finland Granite Belt, Fennoscandian Shield. The structure is hidden under the Lake Summanen and is not directly observable. It owes its discovery to low altitude airborne geophysical data, which revealed a circular ~2.6 km wide electromagnetic anomaly. Two field campaigns were conducted in 2017 to search for rocks with impact signatures. The field-work concentrated on the south-eastern side of the lake following the ice flow direction by the latest (Weichselian) glaciation. A few tens of erratic boulders with shatter cones and striated features along with brecciated rocks were discovered. The microscopic shock metamorphic features out of two shatter cone-bearing samples include up to two sets of planar deformation features (PDFs) in quartz and kink bands in biotite. Based on geological, and petrographic results we conclude that Lake Summanen hides a relatively small, meteorite impact structure, so far of unknown age.

1. Introduction

The Summanen geophysical feature was first identified in the early 2000’s by Jouko Vanne [2]. The observation was based on low altitude aeroelectromagnetic data which revealed circular electromagnetic anomalies. The meteorite impact origin of the Summanen structure has been now proven by [3]. Lake Summanen is located 275 km north from Helsinki (Fig. 1). It is elliptical (8 × 4 km) in shape where the longest axis is in the NW-SE direction due to erosional influence of the Weichselian glaciation. The area deglaciated about 10,700 years ago [4]. Presently, the water level of Lake Summanen is located at 108.5 m a.s.l. and the lake is connected to several other surrounding lakes.

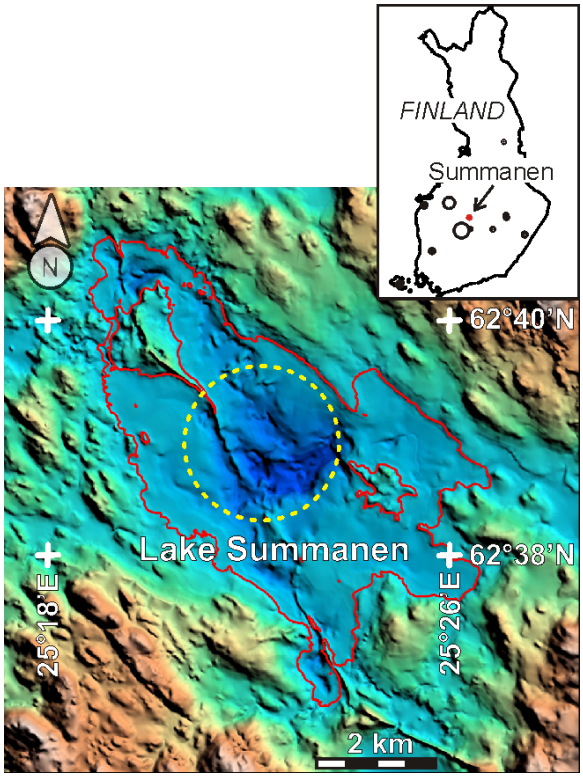

Figure 1: Topographic and bathymetric shaded relief map of the Lake Summanen area. The red line outlines Lake Summanen at the average water level of 108.5 m a.s.l. Max. and min. elevation levels are 231 and 67 m a.s.l., respectively. The maximum depth of the lake is 41 m. The dashed ring with a diameter of ~2.6 km indicates the outline of the proposed crater structure as derived from aeroelectromagnetic data. Inset shows location of the Summanen structure in respect to other Finnish meteorite impact structures.

2. Methods

In 2017, we carried out field campaigns to collect geological data [3], aiming to clarify the origin of the geophysical anomalies. We searched mainly for impact rocks occurring as erratic boulders. Boulder findings were GPS-referenced, lithology was described, photographs were taken and hand samples collected. Seventeen thin sections were prepared. Measurements of PDF orientations were done with the LOMO FS universal-stage (U-stage) mounted on a polarizing microscope. A standard technique described by [1] was followed in measuring the orientation of the c-axis, and poles to PDFs relative to the orientation of the thin section.

3. Results

In two shatter-cone-bearing samples PDFs were identified (Fig. 2). Altogether sixty four measurements of the angle between host quartz c-axes and poles to PDFs were made in 60 quartz grains. In most cases, there was one set of PDFs per grain, usually penetrating the entire grain. Four grains with two sets were found. Eighty three percent of the measured angles between c-axis and poles to PDF are between 20-35°, which with 5° error would correspond to $\{10\bar{1}3\}$ (22.95°) or $\{10\bar{1}2\}$ (32.42°) in most cases. No PDFs with basal (0001) orientation were identified. All PDFs are decorated. Spacings between neighboring lamellae are between 5 and 8 µm. In addition to PDFs, planar features are common, and in rare cases, feather features occur.

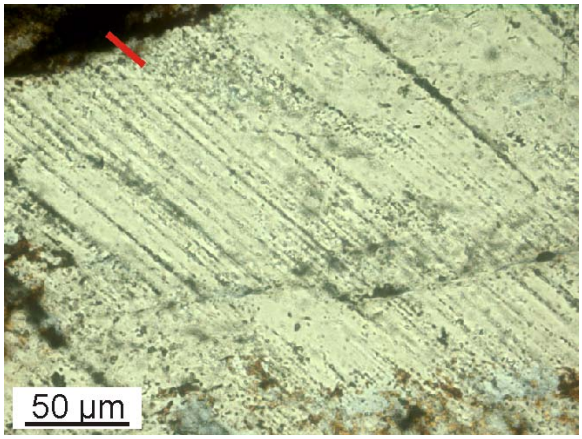

Figure 2: Example of thin section microphotograph of one set of decorated PDFs, taken in cross polarized light.

4. Conclusions

The Summanen impact structure in central Finland, located in a Paleoproterozoic granitic terrain of the Fennoscandian Shield, was discovered due to pronounced aeroelectromagnetic anomalies. The anomalies coincide with the central part of Lake Summanen and are circular, unlike the lake's shoreline that was sculptured by the Weichselian glaciation. The identification of shatter cones in glacially derived erratic boulders, and multiple sets of planar deformation features in quartz prove that the structure is of impact origin. The Summanen structure is the twelfth confirmed impact structure in Finland.

Acknowledgements

M. Lingadevaru and Mohd. Aslam (Central University of Karnataka, India) are acknowledged for their assistance in the field. Juho Kirs contributed to the study with helpful discussions. Grant # IUT20-34 by the Estonian Research Council provided support for this study.

References

[1] Langenhorst F.: Shock metamorphism of some minerals: Basic introduction and microstructural observations, Bulletin of the Czech Geological Survey, Vol. 77, pp. 265–282, 2002.

[2] Lerssi J., Mursu J., Niskanen M., and Pajunen H.: Summasjärven johtavuusanomalian tutkimukset vuosina 2005 ja 2006. Report Q19/2243,2244/2007/1,. Geological Survey of Finland, 2007. In Finnish.

[3] Plado J., Hietala S., Kreitsmann T., Lerssi J., Nenonen J. and Pesonen L.J.: Summanen, a new meteorite impact structure in Central Finland, Meteoritics & Planetary Science, Vol. 53, accepted, 2018.

[4] Stroeven A.P., Hättestrand C., Kleman J., Heyman J., Fabel D., Fredin O., Goodfellow B.W., Harbor J.M., Jansen J.D., Olsen L., Caffee M.W., Fink D., Lundqvist J., Rosqvist G.C., Strömberg B., and Jansson K.N.: Declaciation of Fennoscandia. Quaternary Science Reviews, Vol. 147, pp. 91-121, 2016.

EPSC Abstracts
Vol. 12, EPSC2018-827, 2018
European Planetary Science Congress 2018

Spherical shock experiments with Chelyabinsk meteorite: reflectance spectra changes with increasing shock

Tomas Kohout (1), Evgeniya V. Petrova (2), Grigoriy A. Yakovlev (2), Victor I. Grokhovsky (2), Antti Penttilä (1) and Alessandro Maturilli (3)

(1) Faculty of Science, University of Helsinki, Finland (tomas.kohout@helsinki.fi)
(2) Ural Federal University, Ekaterinburg, Russia (evgeniya.petrova@urfu.ru)
(3) Institute of Planetary Research, DLR, Berlin, Germany

Abstract

Spherical shock experiments produced gradual pressure changes from S4 level up to complete melting. At ~50 GPa peak pressure shock darkening of silicates is observed due to troilite melt penetrating silicate grains associated with reduction in intensity of silicate 1 and 2 μm absorptions. This process stops at higher pressures as partial melting of silicates along grain boundaries isolates troilite melt. Darkening occurs again upon material complete melting. In MIR region, spectral trends are similar, however the reststrahlen silicate bands are still resolved in shock-darkened or impact melt zones.

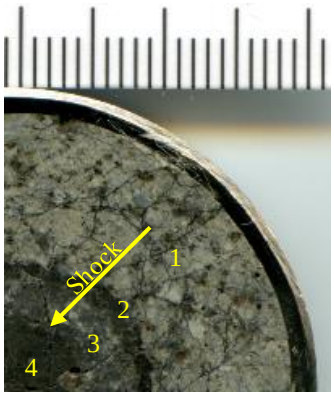

Figure 1: Section of the shocked Chelyabinsk samples with four shock zones. Scale unit is 1 mm.

1. Introduction

Spherical shock experiments with Chelyabinsk meteorite were done at RFNC - VNIITF [1]. The experiment setup allows gradual shock increase from sample rim towards the interior. Altogether 4 zones were observed, corresponding to (1) shock levels S4 at the rim, followed with a (2) sulfide melt rich zone (S5), a (3) zone with extensive silicate melting (S6) and (4) entirely molten phase in the sample interior (Fig. 1).

2. VIS-NIR spectra

The four above mentioned zones are clearly macroscopically distinguishable. The first outer zone resembles original Chelyabinsk light-colored lithology. The light-colored lithology was already shocked up to S3-4 level prior encounter with Earth and thus the experiment-induced shock in this zone is within this initial level. Reflectance spectra (Fig. 2) of this zone resemble also original Chelyabinsk light-colored lithology with prominent silicate absorption bands at 1 and 2 μm [3].

The following second zone is prominent with a sudden and sharp onset of optical darkening. Under the microscope, this zone resembles dark-colored Chelyabinsk lithology with a web of molten troilite veins penetrating silicate grains [2] and acting as darkening agent [3]. The reflected light spectra of this zone are dark and rather flat with only weak silicate absorptions similarly to dark-colored lithology. The corresponding shock stage of this zone is S5 with roughly 50 GPa peak pressure.

The third zone associated with S6 shock level or pressure roughly between 50 and 90 GPa show partial gradual optical brightening compared to dark-colored lithology. Detailed observations under the microscope reveal the onset of extensive silicate crushing and melting along mineral grain boundaries [2]. The extent of the melt increases towards sample interior. The silicate melt along grain boundaries prevents molten

troilite to penetrate silicate grains. Troilite is, thus, contained outside silicate grains, and often forms a eutectic mixture with metal. As the silicates are free of troilite melt the material does not darken and its reflected spectra are intermediate between the ones of the first and second zone. The spectra are slightly darker compared to that of light-colored lithology, but silicate absorptions are clearly visible.

The fourth zone is characterized by complete melting and rapid crystallization [2]. This zone is optically dark due to a mixing of silicate, troilite, and metal melts. The reflected light is flat with subdued silicate absorptions. It resembles Chelyabinsk impact-melt lithology [3].

3. MIR spectra

In MIR region, similar darkening trends to VIS-NIR region are observed in the shocked lithologies. The reststrahlen silicate bands, however, are not significantly attenuated and are still clearly distinguishable. No strong shock-induced wavelength shift in the MIR spectra features is observed.

4. Summary and Conclusions

The spherical shock experiments reproduced Chelyabinsk light-colored, dark-colored, and impact-melt lithologies. Surprisingly, new lithology was observed at pressures intermediate between dark-colored and impact melt lithologies. Within this zone, silicate melting along crystal boundaries isolates troilite melt and prevents silicate darkening. This observation implies on narrow pressure conditions responsible for shock darkening of ordinary chondrites. At the onset of silicate melting, shock darkening effects in ordinary chondrites cease and reappear again only upon complete melting.

Acknowledgements

This work was supported by the Ministry of Education and Science of the Russian Federation (The projects 5.4825.2017/6.7, 5.3451.2017/4.6), the Act 211 of the Government of the Russian Federation, agreement no. 02.A03.21.0006, and the Academy of Finland.

References

[1] Petrova E. V. et al.: Spherical shock experiments with Chelyabinsk meteorite: the experiment and textural gradient, EPSC 2018, 16–21 September 2018, Berlin, Germany, 2018.

[2] Kohout T. et al.: Mineralogy, reflectance spectra, and physical properties of the Chelyabinsk LL5 chondrite – Insight into shock-induced changes in asteroid regoliths, Icarus, Vol. 228, pp. 78-85, 2014.

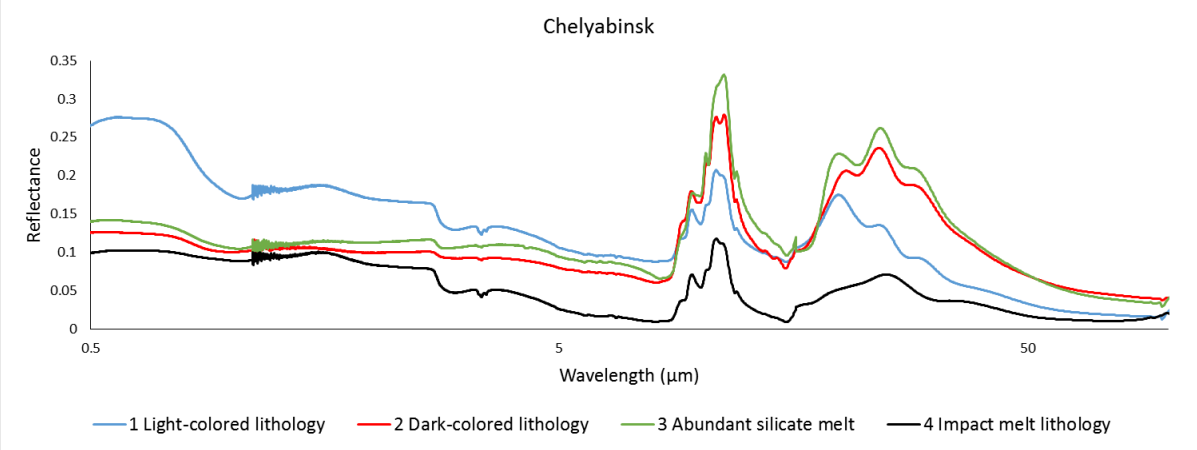

Figure 2: Reflected light spectra of shocked Chelyabinsk meteorite form 0.4 to 100 µm.

EPSC Abstracts
Vol. 12, EPSC2018-833, 2018
European Planetary Science Congress 2018

Impact melt boulder from northern Sweden from an unknown source

Timmu Kreitsmann (1), Satu Hietala (2), Tapio Soukka (3), **Jüri Plado** (1), Jari Nenonen (2) and Lauri J. Pesonen (4)

(1) Department of Geology, University of Tartu, Estonia (timmu.kreitsmann@ut.ee, juri.plado@ut.ee), (2) Geological Survey of Finland, Finland (satu.hietala@gtk.fi, jari.nenonen@gtk.fi), (3) Oulu Mining School, University of Oulu, Finland (soukka.tapio@gmail.com) (4) Solid Earth Geophysics Laboratory, Physics Department, University of Helsinki, Finland (lauri.pesonen@helsinki.fi)

Abstract

We report an impact melt rock finding from northern Sweden, near the village of Kitkiöjärvi. There is no confirmed meteorite impact structure nearby, thus, the source is currently undiscovered. The impact origin of the finding was confirmed by the presence of planar deformation features (PDFs) in quartz.

1. Introduction

Impact cratering is a common and frequent process that affects the planetary surfaces across the solar system throughout geologic time. On Earth, there are 191 confirmed impact structures which are distributed unevenly around the globe. The Fennoscandian Shield houses around 10% of them. Here, we report an impact melt rock finding that originates from an unknown structure in northern Sweden. The semi-rounded impactite boulder, sized 10 × 7 cm, was found by Tapio Soukka in 2017 from a gravel pit at the western side of village Kitkiöjärvi (67°46'16"N 23°03'06"E; Fig. 1).

2. Methods

Mineralogical composition of the whole rock sample was studied by X-ray diffractometry (XRD) and modelled using the Rietveld algorithm-based program Siroquant in the University of Tartu. Two thin sections were prepared and characterized using a standard polarizing microscope with universal-stage (LOMO FS) mounted on it. In addition, thin sections were studied using a ZEISS EVO MA15 scanning electron microscope (SEM) with Oxford AZTEC-MAX energy-dispersive detector (EDS) attached to the SEM.

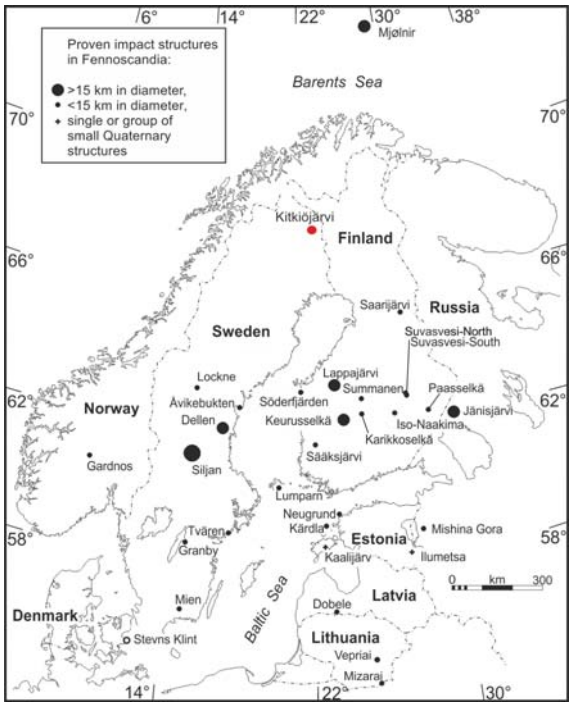

Figure 1: Proven impact structures in Fennoscandia. Location of Kitkiöjärvi impactite is marked by red circle (modified after [1]).

3. Results and discussion

XRD shows that the sample is composed of K-feldspar (66.3 wt%), plagioclase (12.3 wt%), quartz (11.7 wt%), and clay minerals (9.8 wt%). Mineral grains and lithoclasts are rounded to angular (Fig. 2A), mostly composed of feldspar and quartz. Rare biotite is chloritized and shows kink banding. Planar deformation features (PDFs) are common in quartz (Fig. 2B). PDFs are decorated and appear mostly as one or two sets. Quartz also exhibits

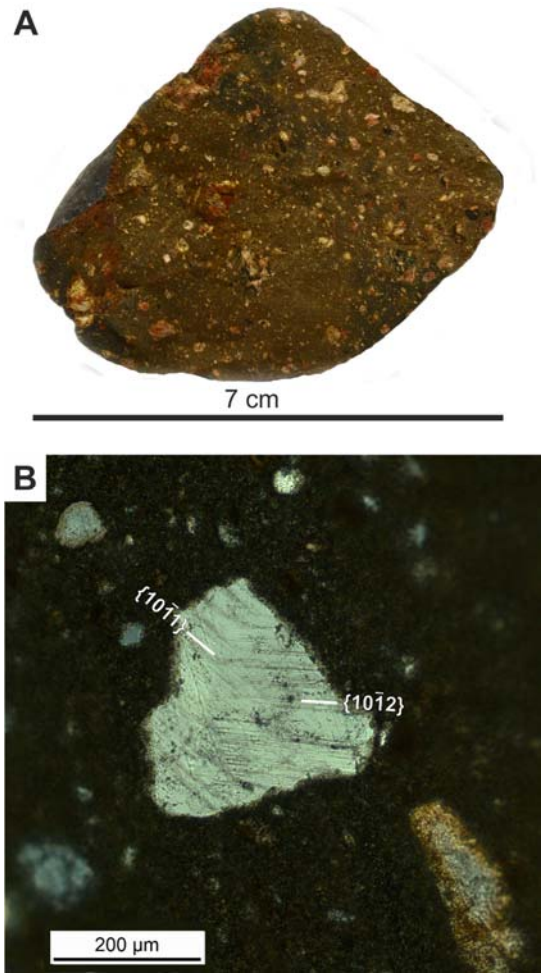

Figure 2: (A) clast-poor impact melt boulder. (B) two sets of PDFs in anhedral quartz grain, XPL.

structure similar to chert-like ballen quartz. Groundmass is aphanitic (recrystallized) and consists of cryptocrystalline K-feldspar.

3.1 Origin of the Kitkiöjärvi impactite

With the identification of PDFs in the Kitkiöjärvi sample, we have proven its impact origin since the PDFs in quartz are the most commonly used indicator to prove an impact origin of the rock sample/structure. The PDFs are formed in pressure range from 5 to 35 GPa [2], which are experienced only in the impact cratering process. There are, however, no known meteorite impact craters nearby that could serve as source structures for the present finding.

We note that Kitkiöjärvi is just a few kilometres apart from the Muonionalusta octahedrite field [3] but the meteorites from the latter and the Kitkiöjärvi impactite unlikely result from the same event. First, impact glass in Kitkiöjärvi impactite has recrystallized to cryptocrystalline K-feldspar hinting for the significantly greater age than the terrestrial age of Muonionalusta is >0.8 Ma [4]. Second, formation of the PDFs in Kitkiöjärvi impactite required pressures >5 GPa, which hints for a cratering process. On the contrary, large size (25 × 15 km) of the present Mounionalusta strewn field and the undisturbed nature of the saprolite of the area [5] suggest that the Mounionalusta meteoroid was not a cratering one.

4. Conclusions

We report an impactite (melt) finding from northern Sweden. Impact origin of the melt rock sample was confirmed by the identification of planar deformation features in quartz. The source of this boulder has to be a currently unknown meteorite impact structure, as the nearest known impact structure (Saarijärvi) is 350 km away. Hence, further geological studies of the area are required to find a source of this impactite.

References

[1] Abels, A., Plado, J., Pesonen L.J., and Lehtinen, M.: The Impact Cratering Record of Fennoscandia – A Close Look at the Database in. Impacts in Precambrian Shields, edited by Plado, J and Pesonen, L.J, Springer-Verlag, Berlin, pp. 1-58, 2002.

[2] Stöffler D. and Langenhorst F.: Shock metamorphism of quartz in nature and experiment: I. Basic observation and theory. Meteoritics, Vol. 29, pp. 155–181, 1994.

[3] Holtstam D., Broman C., Söderhielm J and Zetterqvist A.: First discovery of stishovite in an iron meteorite. Meteoritics & Planetary Science, Vol. 38, pp. 1579-1583, 2003.

[4] Chang C.T. and Wänke H.: Beryllium-10 in iron meteorites, their cosmic ray exposure and terrestrial ages. In Meteorite Research, edited by Millman P.M.D. Dordrecht, Riedel Publication Company, pp. 397-406, 1969.

[5] Lagerbäck R. and Wickman F.E.: A new iron meteorite from Muonionalusta, northernmost Sweden. GFF, Vol. 119, pp. 193-198, 1997.

EPSC Abstracts
Vol. 12, EPSC2018-835, 2018
European Planetary Science Congress 2018

Variability within and between large bodies of Muong Nong-type tektites in Laos

Roman Skála (1,2), Šárka Křížová (1,2), Šárka Matoušková (1), Milan Trnka (3), Karel Žák (1)

(1) The Czech Academy of Sciences, Institute of Geology, Rozvojová 269, CZ-165 00, Prague 6, Czech Republic (2) Institute of Geochemistry, Mineralogy and Mineral Resources, Faculty of Science, Charles University, Albertov 6, 128 43 Prague 2, Czech Republic (3) Lithos Ltd., Durďákova 41, 613 00 Brno, Czech Republic (skala@gli.cas.cz)

1. Introduction

Basic features characterizing Muong Nong-type (MN) tektites include their irregular shape, blocky and layered appearance, structural and chemical inhomogeneity, and generally larger sizes than splash or ablated forms [4]. The MN tektites are most widely distributed in Australasian tektite (AAT) strewn field. Presence of zircon, quartz, rutile, monazite and decomposed Al_2SiO_5 in MN AAT indicates, according to [3], that their parent material is of detrital sedimentary origin with a metamorphic component. Two largest single fragments of MN tektites reported in literature weigh 24 kg each [2]. However, mass of the largest known MN is much higher: large fragmented bodies may have been as large as 1,000 kg [1]. Since only a limited number of chemical analyses evaluating the compositional variability within and between these large tektite bodies are available [5], we decided to analyze fragments of MN AAT from them.

2. Results

We sampled three MN AAT bodies in Laos labeled here as DB-5, DB-115 and DB-118. The body DB-5 is located close to Ban Tako at 16.37315° N, 106.45483° E, and is identical to the object reported by [1] weighing ca. 1,000 kg. The location of the DB-115 body is 16.46150° N, 106.48917° E and expected weight is 200 kg. The object DB-118 is situated close to Muong Nong at 16.39509° N, 106.49630° E and its weight is ~200 kg. All the bodies are fractured and sizes of excavated shards varies in broad range from grams to hundreds of grams. Polished thin sections were manufactured from the fragments and chemical composition measured with electron probe microanalyzer (EPMA) and laser ablation inductively coupled plasma mass spectrometer (LA-ICP-MS). Major, minor and trace element compositions of all fragments show that there is a high compositional variability between individual bodies as well as within them (Figs. 1 and 2). The magnitude of this variability is larger than that reported in [5]. Tight negative correlations between all major element oxides vs. silica observed generally in tektites [4] is not found for Na_2O and K_2O in this dataset. Major element contents indicate presence of mutually compositionally different domains/layers within individual fragments (samples 3 and 23 of DB-118). Nickel content in fragments of the DB-115 body is extremely variable and some of excavated shards are highly enriched in this element. Such high Ni concentrations accompanied by elevated contents of Co and Cr may already be considered indicative of low contents of projectile material. Concentrations of volatile (Pb, Zn, Cu) as well as refractory (W) elements are more or less invariant in fragments of DB-115 whereas it varies in remaining samples. Strong positive correlation of otherwise lithophile elements (Cr and Mn) with siderophile Ni may support high temperature origin of MN AAT as long as this change of chemical behavior is known only at elevated T.

3. Summary and Conclusions

Three large MN AAT bodies display compositional variability on regional, local as well as individual fragment scales. Correlation of contents of siderophile and lithophile elements provides a support for high-T origin of tektites. Elevated concentrations of Ni, Co and Cr can be interpreted as a potential admixture of meteoritic component though further studies (e.g., contents HSE, Os or Cr isotope systematics) are required to resolve this issue.

Acknowledgements

This research was funded by the Czech Science Foundation project 17-27099S and conducted within the institutional support RVO 67985831 of the Institute of Geology of the Czech Academy of Sciences.

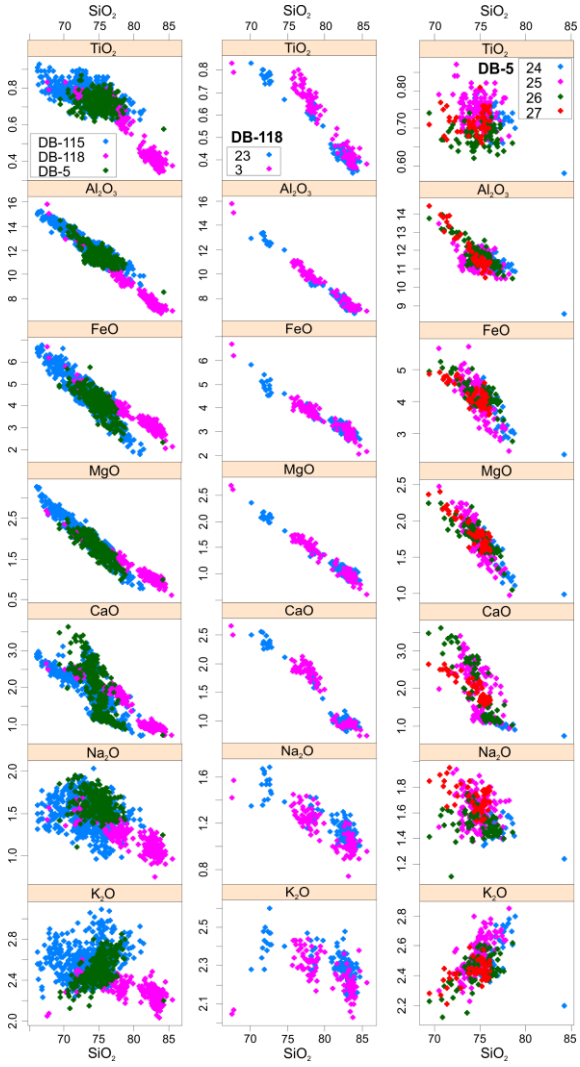

Figure 1: Major element compositions (in wt.%) determined by EPMA in fragments excavated from three large MN AAT bodies in Laos.

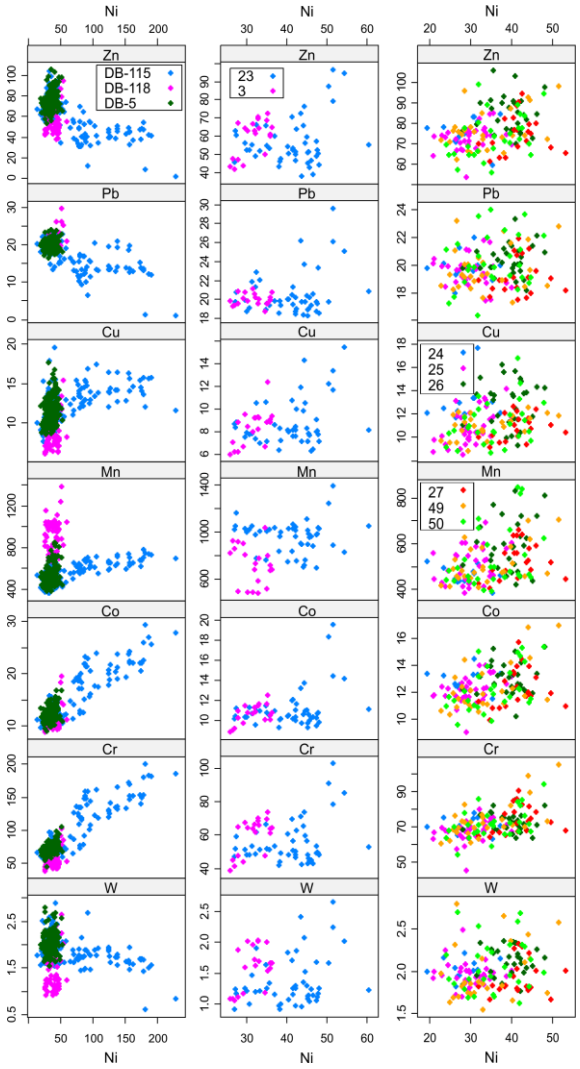

Figure 2: Selected minor and trace element compositions (in ppm) determined by LA-ICP-MS in fragments excavated from three large MN AAT bodies in Laos.

References

[1] Fiske, P.S., Schnetzler, C.C., McHone, J. , Chanthavaichith, K.K., Homsombath, I. , Phouthakayalat, T. , Khenthavong, B. and Xuan, P. T.: Layered tektites of southeast Asia: Field studies in central Laos and Vietnam, Meteoritics & Planetary Science, Vol. 34, pp. 757-761, 1999.

[2] Futrell, D.S. and Wasson, J.T.: A 10.8 - kg layered (Muong - Nong - type) tektite from Wenchang, Hainan, China, Meteoritics, Vol. 28, pp. 136-137, 1993.

[3] Glass B.P.: Crystalline inclusions in a Muong Nong-type indochinite, Earth and Planetary Science Letters, Vol. 16, pp. 23-26, 1972.

[4] Koeberl, C.: Geochemistry and origin of Muong Nong-type tektites, Geochimica et Cosmochimica Acta, Vol. 56, pp. 1033-1064, 1992.

[5] Schnetzler, C.C.: Mechanism of Muong Nong-type tektite formation and speculation on the source of Australasian tektites, Meteoritics, Vol. 27, pp. 154-165, 1992.

EPSC Abstracts
Vol. 12, EPSC2018-871, 2018
European Planetary Science Congress 2018

Impact-Induced Melting by Giant Collision Events

L. Manske[1,2], K. Wünnemann[1,2], M. Nakajima[3], C. Burger[4] and A.-C. Plesa[5], [1]Museum für Naturkunde, Leibniz Institut for Evolution and Biodiversity Science, 10115 Berlin, Germany, lukas.manske@mfn-berlin.de, [2]Institute for Geological Sciences, Planetary Sciences and Remote Sensing, Freie Universität 12249 Berlin, Germany [3]Department of Terrestrial Magnetism, Carnegie Institution for Science Washington, DC 20005, USA, [4]Department of Astrophysics, University of Vienna, 1180 Vienna, Austria. [5]German Aerospace Center (DLR), 12489 Berlin, Germany.

1. Introduction

We revisited the long-standing problem of the generation of melt as a consequence of giant impact events, which may not be accurately addressed by classical scaling-laws [1,2]. During the accretion phase, the thermochemical evolution of the terrestrial planets was heavily influenced by giant collisions with other cosmic bodies such as the Moon-forming event on the young Earth [3]. Besides variations in the compositional budged, such impacts transfer a significant amount of energy to heat up the planet and cause the formation of local magma ponds or even global magma oceans. For smaller impact events (smaller than basin-forming), the amount of impact-induced melting can be predicted by scaling-laws [1,2]. But on a larger scale they might not be accurate as they do not account for the initial temperature or lithostatic pressure of planets interior, especially where the initial temperatures are close to the solidus (especially for younger planet). To better understand and quantify the mechanism of heat production and melting during large-scale impact events we conducted a series of numerical models and determined the volume of melt production.

2. Methods

We use the iSALE Eulerian shock physics code [4,5] (Version *Dellen*) and two different Smooth-Particle-Hydrocodes (SPH) [6,7] to model large-scale hypervelocity impact events. The thermodynamic state (EoS) is calculated by ANEOS [8] for basalt, dunite, and iron representing the planetary crust, mantle and core, respectively.

To locate and quantify the volume of the impact-induced melt we measure the material's (post-impact) final temperature (or entropy) T_f and compare it with the pressure-dependent melt temperature [9] (or entropy) for incipient T_{M1} and complete melting T_{M2}. To bypass diffusion-based inaccuracies of the temperature field calculated by iSALE, we use massless Lagrangian tracers to record the material's highest shock pressure P_{peak} (peak shock pressure), which is proportional to the raise of the temperature [2]: $P_{peak} \propto \Delta T$. Using ANEOS, the temperature increase ΔT is then worked out via the thermodynamic release path from the peak shock pressure P_{Peak} state to the final (post-impact) pressure P_f state and can be added to the initial temperature T_{Ini} to derive the final temperature $T_f = \Delta T + T_{Ini}$. It should be noted, that ΔT is not only a function of the peak shock and final pressure, but also of the initial pressure and temperature P_{Ini}, T_{Ini} conditions. The final temperature (or entropy) T_f can then be compared to the melt temperatures (or entropies) $T_{M1,2}(P_f)$ to determine whether the material is (partially) molten or not. Tracers also record the material's displacement, which allows for taking decompression melting into account. Decompression is a consequence of the stratigraphic uplift of the material in the course of crater formation resulting in a lower lithostatic pressure and hence lower melting temperatures $T_{M1,2}(P_f)$ than before impact $T_{M1,2}(P_{Ini})$. To measure the influence of decompression melting, we compare the temperature increase caused by the shock ΔT with the change of the melt temperature caused by the stratigraphic uplift: $\Delta T_M = T_{M1,2}(P_f) - T_{M1,2}(P_{Ini})$ (cf. Fig. 2, left).

We carried out a series of numerical models for Mars and the Earth's Moon assuming individual initial composition and temperature distributions, impact velocities, and gravity. While neglecting differentiated bodies at this stage, the projectiles consists of a dunitic composition and their radii were resolved by 50 cells (50 CPPR) in all iSALE models. In the SPH models we used about 1 million particles. The initial thermal profiles ($T_i = f(P)$) differ from hot to cold setups, representing earlier to more recent stages of the planets' thermal evolution, respectively [10].

3. Results

In each model series we choose an initial temperature T_{Ini} (planet's age) and vary the impactor diameter L and velocity v_i. We calculate reference models, which are based on simplified assumptions corresponding to the scaling-laws but with a planet-like layered target. These models match the scaling-laws well, while they indicate a crust or mantle melt regime depending on penetration depth (L,v_i) and planet structure (cf. Fig. 1).

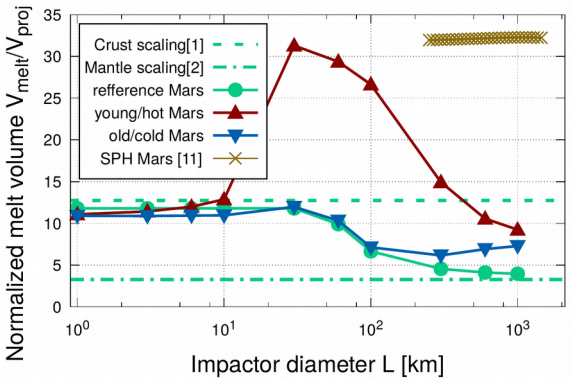

Fig. 1. : Normalized melt production for Mars-like parameters with v_i = 15km/s. Scaling laws [1,2] compared to a reference model (green). More realistic models based on temperature profiles corresponding to different ages after planet formation (red: 40 Myr/ blue: 4500 Myr) [10] are shown by triangles. Preliminary SPH code simulations are presented in ocher [11].

Fig. 1 indicates, that the more realistic models (triangles) are approximately in agreement with classic scaling for smaller impacts; however, larger events are not. In particular, the normalized melt production (V_{melt} /$V_{projectile}$) shows large variations that are caused by the depth dependent distribution of the initial temperature T_i and thus the evolutionary state of the planet. This leads to a depth dependence of the threshold temperature increase to cause melting $\Delta T_{Melt}(z) = \Delta T_{M1,2}(P(z)) - \Delta T_{Ini}(z)$. It can be shown that the maximum normalized melt production occurs at impactor sizes, where the main melt body is located in the area, which requires the lowest ΔT_{Melt}. This area is often located at the bottom of the lithosphere.

For even bigger impactor sizes, SPH code simulations have been added [11] (ocher crosses). Those simulations are based on a temperature profile, where T_i is equal to the solidus T_{M1}. This relation also holds true for a certain depth range of the young Mars model. Using a impactor diameter of L = 30 km, most of the melt is produced in this range, which makes the normalized melt volumes comparable to the SPH model. One can see, that the differently derived melt volumes are almost equal in this case.

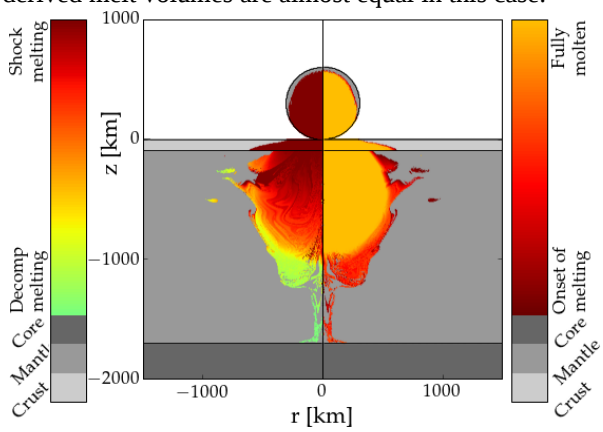

Fig. 2.: Melt distribution mapped back to the initial Position. Colors indicate molten material. Left: Influence of decompression melting. Right: Degree of partial melt.

Fig. 2 implies, that the more the material can rise and the closer the temperature and melt temperatures are, the more decompression melting contribute to melt production. Thus decompression melting is sensitive to the chosen initial temperature T_i, melt temperature $T_{M1,2}$ and impactor.

Our goal is to derive a lookup table for impact-induced melt volumes V_m as a function of impact parameters V_m = f(L, v_i, T_i, P_f) based on merged SPH and mesh based simulations.

Acknowledgements

We gratefully acknowledge the developers of iSALE, including Gareth Collins, Dirk Elbeshauesn, Boris Ivanov and Jay Melosh. This work was funded by the Deutsche Forschungsgemeinschaft (SFB-TRR 170, Subproj. C2, C4).

References

[1] Abramov O. et al. (2012) Icarus 218, 906-916. [2] Pierazzo et al. (1997) Icarus 127, 408-423, 1997. [3] Marchi S. et al. (2014) Nature 511, 578-582. [4] Collins. G. S. et al. (2004) MPS. 39, 217-231. [5] Wünnemann K. et al. (2006) Icarus 180, 514–527. [6] Schäfer C. et al., (2016) Astronomy & Astrophysics 590, A19. [7] Nakajima & Stevenson, (2015) EPSL 427, 286-295. [8] Thompson and Lauson (1972) Report SC-RR-71 0714, Sandia Natailonal Lab. [9] Ruedas, T. and Breuer, D. (2017) JGR, 122, 1554-1579 [10] Plesa, A.-C. et al. (2016) JGR 121, 2386-2403. [11] Nakajima et al. (2016) AGU, P51A-2118.

EPSC Abstracts
Vol. 12, EPSC2018-889, 2018
European Planetary Science Congress 2018

Testing impact numerical model setups for simple craters

Prieur Nils (1), Tobias Rolf (1) and Stephanie Werner (1)
(1) University of Oslo, Dept. of Geosciences, Centre for Earth Evolution and Dynamics CEED, Norway, (nilscp@geo.uio.no)

Abstract

To investigate the challenges in testing impact numerical model setups we selected three of the most common setups used in the impact cratering community. For each of these setups, we carried out simulations where the projectile diameters are varied. We focus only on simple craters on the lunar surface (i.e., craters with diameters smaller than 14-31 km [1]). Preliminary results are presented and discussed in the second part of this abstract.

1. Introduction

A crucial step in impact numerical modeling is to directly compare results with observations in order to test and quantify how well a model reproduces the processes and products generated through a natural impact. In most studies, this step is conducted with the help of a single observation, as they often focus on reproducing a particular impact structure on a certain planetary body. A problem that arises from such act is that single crater geometry (depth, diameter, wall slope and rim height, generally simplified to depth and diameter) can be reproduced by several numerical model setups. Numerical results may therefore be non-unique. The fact that neither the projectile diameter, composition, impact velocity nor angle that produces a particular impact structure are known adds another level of complexity in the testing of a model setup, as an impact with the same energy but different impact velocity may result in different geometry [e.g., 2]. The goal of this study is not only to test existing setups but to ultimately develop a single (or several) model setup(s) that will match the lunar observations over a large crater diameter interval.

2. Method

The iSALE-2D numerical impact code is here used [3-5]. This code gives us the versatility to choose in between routines (e.g., strength, porosity and dilatancy) to describe the material model, allowing us to test easily different model setups. The impact velocity is here held constant to a value of U = 12.7 km/s, which is a rather reasonable average impact velocity for the Moon (including the vertical component of a 45^o impact angle).

The three setups investigated are relatively different, the first one (#1) describes best granular or brecciated target [6], while the second [7] (#2) and third (#3) describes best the behavior of rocks [8]. Model parameters which might affect the most the final crater geometry and morphology are listed below. In addition, we list two other important factors: the crater diameter interval over which the setups have been used, and the datasets against which the setup have been tested. Readers are recommended to the references for a full description of each of those models. Note that the setups are sorted in increasing degree of complexities (from top to bottom, #1-3), and that strength model parameters in #2 and #3 have different values.

#1: **strength model:** completely damaged material, **initial porosity:** yes, **dilatancy:** no, **crater diameter interval:** 1 - 15 km (Moon); **tested against:** transient crater diameter scaling laws derived at laboratory-scale [6].

#2: **strength model:** intact and damaged material [9], **initial porosity:** no, **dilatancy:** no, **crater diameter:** 2.2 km (Moon); **tested against:** crater geometry of Linne crater [7].

#3: **strength model:** intact and damaged material [9], **initial porosity:** no, **dilatancy:** yes. **crater diameter:** 4.0 km (Earth); **tested against:** crater geometry, porosity gradient and gravity anomaly beneath Brent crater [8].

As computational resources increase considerably with decreasing projectile diameters, only simulations resulting in final rim-to-rim crater diameter D_r> 8 km have so far been investigated. Results are here compared against “fresh” simple impact craters on the lunar surface compiled in [10]. We compare the three different model setups not

only to a single observation but to several observations with different crater diameters (Figure 1). By doing so, we also test whether a model setup performs well over a crater diameter interval. The three model setups are compared to elevation points obtained from the Lunar Orbiter Laser Altimeter data on-board the Lunar Reconnaissance Orbiter [11]. Both x- and y-axes are normalized with D_r (Figure 1).

3. Results and discussion

Of the three setups, model setup #1 fits the best the different observations for D_r> 8 km on the lunar surface, with both a good representation of the depth, wall slope and crater diameter (Figure 1). We note that the rim heights seem to be more sensitive to asymmetries probably due to pre-existing topography. For setup #2, the wall slope is well reproduced, but the observed depth-diameter ratio d_r/D_r is often underestimates by about 10% (depicted by the y-axis on Figure 1). In #3, d_r/D_r is underestimated by 25%, certainly due to the fact that #3 is calibrated against Brent crater which have a d_r/D_r~0.15. The collapse observed at Brent crater seems to be larger than the collapse for craters with D_r> 8 km on the Moon. At last, we found that for a similar projectile diameter L = 1000 m, different D_r is obtained: $D_{r\#1}$ = 13.38, $D_{r\#2}$ = 17.28 and $D_{r\#3}$= 13.63 km. The largest difference is about 4 km, likely due to the fact that the effect of porosity is neglected in #2. All of these results clearly show that more work is required to develop a numerical model setup which will fit a larger crater diameter interval of observations.

4. Future work

Additional results will be presented at the conference, including the comparison to fresh impact craters with 100 m < D_r < 8 km, and models including both strength and porosity gradients. In addition, different dilatancy and strength model parameters will be tested in model setups #2 and #3.

Acknowledgements

We thank the developers of iSALE and pySALEPlot. This work was funded by the Centre for Evolution and Dynamics (CEED, 223272), the Norwegian Research Council (235058) and ESA (690477).

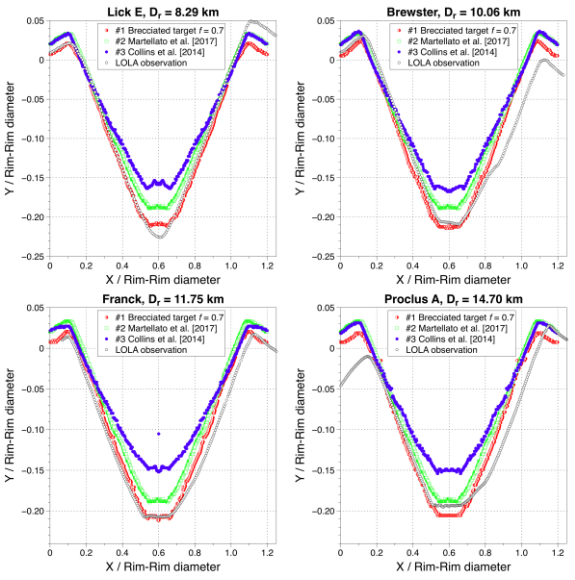

Figure 1: Craters from the three model setups are compared to four fresh simple impact craters on the Moon (Lick E, Brewster, Franck and Proclus A). LOLA altimeter elevation points are depicted in black and white circles.

References

[1] Pike, R. J.: Control of crater morphology by gravity and target type: Mars, Earth, Moon. LPSC, 1980.

[2] Watters, W., et al.: Dependence of secondary crater characteristics on downrange distance: high-resolution morphometry and simulations. JGR Planets, 2017.

[3] Amsden et al.: SALE : A Simplified ALE Computer program for Fluid Flow at All Speeds, LANL, LA-8095, 101, 1980.

[4] Collins, G. S., Melosh, H. J., and Ivanov, B. A.: Modeling damage and deformation in impact simulations, MPS, 2004.

[5] Wünnemann, K., Collins, G. S., and Melosh, H. J.: A strain-based porosity model for use in hydrocode simulations of impacts and implications for transient crater growth in porous targets, Icarus, 2006

[6] Prieur, N. C., et al.: The effect of target properties on transient crater scaling for simple craters, JGR Planets. 2017.

[7] Martellato, E., et al: Is the Linn e impact crater morphology influenced by the rheological layering on the Moon's surface? Insights from numerical modeling, MPS. 2017.

[8] Collins, G. S: Numerical simulations of impact crater formation with dilatancy. JGR Planets. 2014.

[9] Collins, G. S., Melosh, H. J., Ivanov, B. A.: Modeling damage and deformation in impact simulations. MPS. 2004.

[10] Pike, R. J.: Depth/diameter relations of fresh lunar craters: Revision from spacecraft data. GRL. 1974.

[11] Smith, D., et al.: Initial observations from the Lunar Orbiter Laser Altimeter (LOLA). GRL. 2010.

EPSC Abstracts
Vol. 12, EPSC2018-955, 2018
European Planetary Science Congress 2018

Crater depth statistics: constraining obliteration rates from secondary clusters of Mojave crater

Sylvain Breton[1], Cathy Quantin-Nataf[1], Lu Pan[1], Thomas Bodin[1] and Erwan Bras[1]
[1] Université de Lyon, Observatoire de Lyon, France (sylvain.breton@univ-lyon1.fr)

Abstract

Crater statistics based on size frequency distribution have been correlated with the age of planets' surfaces. We propose to widen statistical analysis of craters using not only diameter but also crater depths. We briefly present a calibrated method that quickly measures the depth of craters and provide a dataset that is large enough to perform statistical analyses. We use this method to study the evolution for depth of several secondary clusters of the Martian crater Mojave. Our method shows that the depth to diameter ratio (D/d) is not constant but varies with the diameter. This brings a new perspective on crater depth distribution.

1. Introduction

Impact craters are found on all terrestrial bodies. Their wide repartition have made them a key to understand planetary surfaces evolution. The most common use of craters is to date planetary surfaces. The known influx of impactors acts as a clock that adds craters as time is going. Since Apollo sample-return missions, a correlation has been established between the crater size-frequency distribution and absolute ages of the terrestrial planets surfaces. However, size-frequency distribution can be influenced by surface processes. Hence the idea that crater size-frequency distributions can be used to constrain surface processes. But increasing the complexity of the models requires new parameters. Crater morphology can be used to do so, especially crater depth as it is closely linked with crater infilling and erosion. Crater D/d has been widely exploited to tackle issues such as characterizing the depth of fresh craters and estimating obliteration of craters. Most of the time those studies interpret small datasets. Morphology measures are time consuming and there is no established method to interpret crater depths statistically. Here, we propose a workflow that allows systematic extraction of depth in a crater map. Secondary clusters are formed

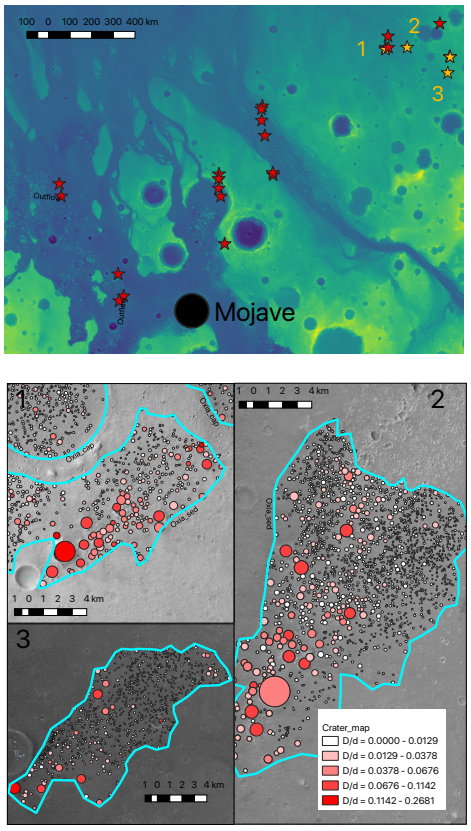

Figure 1: Map of Mojave and its surroundings, stars represent the mapped clusters. Yellow stars locate cluster represented in figure 2 (top). Details of mapped clusters (1,2 and 3).

simultaneously after a huge impact. Studying their depth in different regions may provide key clues on the evolution of craters under different climatic conditions [1].

2. Crater mapping and depth measures

Mojave is a crater of about 58 km diameter located at the outlet of Valles Marineris. We look for secondary

clusters in a radius of 1000 km around Mojave on CTX. Secondary clusters that are oriented toward the primary source and with a CTX stereo-pair coverage, are selected for mapping. The depth of each crater is measured from the crater map and a co-registered DEM using GRASS raster statistics-tool. This tool retrieve 95th and 4th percentiles, depth is measured as the difference between those two values. Craters depth are plotted relative to their diameter. In order to clearly display crater density, we convoluted each crater by a gaussian function corresponding to the error [2][3].

3. Results

Figure 2 represents the crater distribution on three clusters located on a sedimentary layer on Oxia Planum [4]. Crater diameters range from 100 m to km scale. We clearly note that D/d strongly depends on crater diameter and on the studied cluster. Small craters present wider range of depths. In cluster 2 we observe a shallower trend than on site 1 and 3. We still need to investigate if this depletion can be linked to local characteristics. Our measure of D/d shows no trend relative to the distance to the source primary. However significant differences can be observed when looking at different geologic units. In our range of distance to the primary, the mean D/d seems to change according to the local geology and/or climate more than according to the distance to the source.

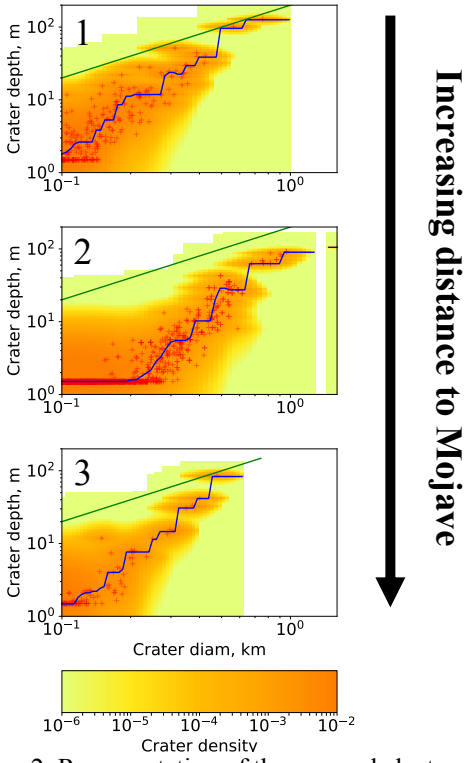

Figure 2: Representation of the mapped clusters in the depth/diameter space. Each red cross represent a measured crater. The colormap represent the crater frequency. Blue line is the mean depth value. Green line represent a D/d = 0.2 which is expected for pristine secondary craters above 160 km [1].

4. Summary and Conclusions

We identified and mapped secondary clusters originating from Mojave. We extensively measured the depth of the craters within these clusters. We represent our data in an original formalism that emphasize crater frequency variations on a depth-diameter space. We identified differences between mapped clusters, although we still need to interpret those differences in term of surface properties and processes. This multiparameter statistical approach can better constrain age of a planetary surface and surface processes. We are developing other usage of this data such as characterisation of fresh crater depth.

Acknowledgements

All image processing are done using MarsSI Web facility [5].

References

[1] W. A. Watters *et al.*, "Dependence of secondary crater characteristics on downrange distance: High-resolution morphometry and simulations," *J. Geophys. Res. Planets*, vol. 122, no. 8, pp. 1773-1800, 2017.

[2] S. J. Robbins *et al.*, "Revised recommended methods for analyzing crater size-frequency distributions," *Meteorit. Planet. Sci.*, vol. 41, 2018.

[3] S. Breton *et al.*, "Automatic crater morphometry extraction," *submited*

[4] Quantin *et al.*, "Oxia Planum",*4th Landing site selection workshop Exomars200, ESTEC, Netherland,* march 2017

[5] C. Quantin-Nataf *et al.*, "MarsSI: Martian surface data processing information system," *Planet. Space Sci.*, vol. 150, pp. 157–170, 2018.

EPSC Abstracts
Vol. 12, EPSC2018-957, 2018
European Planetary Science Congress 2018

Identification of kerogen by SCA device in materials produced by the impact of an extraterrestrial body on Earth

Leticia Gómez-Nubla, Julene Aramendia, Imanol Torre-Fdez, Patricia Ruiz-Galende, Silvia Fdez-Ortiz de Vallejuelo, Juan Manuel Madariaga
University of the Basque Country (UPV/EHU), Barrio Sarriena, s/n, 48940 Leioa, Spain (leticia.gomez@ehu.eus)

Abstract

Libyan Desert Glasses (LDGs) are materials formed at high pressures and temperatures by the impact of an extraterrestrial body on Earth 28.5 million years ago. Therefore, the identification of organic matter in them can be an evidence of early life on Earth. In this work, SCA (Structural and chemical analyser) device (SEM-EDS (Scanning Electron Microscopy/Energy Dispersive X-Ray Spectroscopy) plus Raman spectroscopy) was used to search kerogen, which is formed from the maturation of sedimentary reduced organic carbon. In this manner, black shale (kerogen and calcites) was identified in the inner part of the LDGs. This fact could suppose the presence of biological organic material by the time of LDG formation. Moreover, the Raman bands of the black shale spectra were shifted, which could be because of an effect of high pressure and temperature in the formation of the LDGs.

1. Introduction

LDGs are impact glasses formed at high pressures (between 6 and more than 30GPa) and temperatures (between 300 and 1470ºC) after the impact of an extraterrestrial material (meteorite, asteroid or comet) on Earth 28.5 million years ago [1]. Concretely, they have been found in the Western Desert of Egypt (near the Libyan border). They consist of a siliceous matrix with embedded inclusions, which can contain different minerals such as calcite ($CaCO_3$), hematite (Fe_2O_3), quartz (SiO_2), rutile (TiO_2), magnesite ($MgCO_3$), etc. [1]. Apart from inorganic compounds, LDGs could contain organic ones, which could be the key for the search of life in the Solar System. Despite this fact, organic matter in LDGs has been rarely mentioned. The main source of organic matter on Earth is sedimentary reduced organic carbon, which matures to kerogen [2]. Kerogen is the insoluble macromolecular fraction of sedimentary organic matter and is the precursor of oil and gas resources [3]. Therefore, the aim of this work was to identify organic matter in form of kerogen in the LDGs using non-destructive analytical techniques and, thus, to complete and deepen the conditions of formation of the LDGs.

2. Material and methods

2.1 Materials

LDGs from the Meteorites Collection of the Basque Country University (UPV/EHU) were studied. Some of the samples were sliced and thin sections were prepared to make the analysis of the inner part of the LDGs easier. This work was focused on the inner side to avoid possible interferences with the atmosphere.

2.2 Methods

SCA, Raman spectroscopy plus SEM-EDS, was employed. SCA allowed us to merge SEM images, EDS analysis and Raman spectroscopy analysis in the same micrometrical point. For that purpose, an EVO 40 Scanning Electron Microscope (Carl Zeiss NTS GmbH, Germany) coupled to an X-Max Energy-Dispersive X-Ray spectroscopy equipment (Oxford Instruments, United Kingdom) and a Renishaw inVia Raman micro spectrometer with a 514 nm argon ion excitation laser (Renishaw, United Kingdom) were used.

3. Results and discussion

Firstly, SEM-EDS analysis was performed in several parts of the LDGs. Thus, C, a possible indicator of presence of organic matter, could be located (see Figure 1). As can be observed in the Figure 1, C together with Ca, S, Si, Mg, Na and O were distinguished in certain cavities of the inner part of the LDGs. It was remarkable the differences of the C

percentage in several points. For example, the analysis performed in the point 1 had less C and more elements than in the point 2. Once these results were observed, Raman spectroscopy was used to determine the molecular composition in those points with higher presence of C according to SEM-EDS.

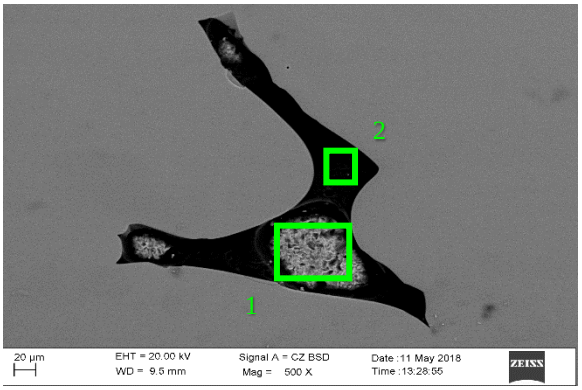

	Atomic%	
	1	2
C	52.42	84.74
O	30.86	15.14
Na	2.72	
Mg	0.79	
Si	11.39	0.12
S	0.05	
Ca	1.77	

Figure 1: SEM image and atomic percentage of the elements found in the selected areas by EDS.

Thus, it was possible to identify kerogen in the point 2 of the Figure 1. However, in order to improve the Raman spectra obtained by SCA, a point-by-point Raman analysis was carried out in the same area. In this way, black shale was detected, not only in that area, but also in different cavities of the sample (see Figure 2). Black shale consists of kerogen trapped in the pores of silicate based on sedimentary rocks and calcites. It is as fossilized organic matter and consists mostly of carbon [4]. Therefore, its identification could reveal the presence of biological organic material by the time of LDG formation. Moreover, it is remarkable that the Raman bands of the black shale were shifted. According to bibliography, high pressures and temperatures can shift their Raman bands [5].

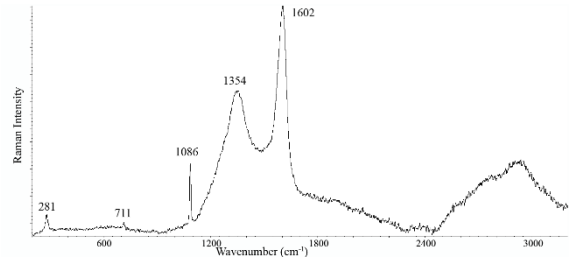

Figure 2: Raman spectrum of black shale (kerogen plus calcite over a silicate matrix).

4. Conclusions

SCA device allowed us to discern areas in the inner part of the LDGs where there was presence of black shale, which could be a signature of previous biological material. Moreover, Raman spectroscopy allowed us to observe that the kerogen could have been subjected to high pressures and temperatures.

Acknowledgements

This work has been financially supported through the Exomars-Raman project (ref. ESP2017-87690-C3-1-R), funded by the Spanish Agency for Research AEI (MINEICO-FEDER/UE). Technical and human support provided by the Raman-LASPEA Laboratory of the SGIker (UPV/EHU, MICINN, GV/EJ, ERDF and ESF) is gratefully acknowledged.

References

[1] Gomez Nubla, L., Aramendia, J., Fdez-Ortiz de Vallejuelo, S., Alonso-Olazabal, A., et al.: Multispectroscopic methodology to study Libyan desert glass and its formation conditions, Analytical and Bioanalytical Chemistry, Vol. 409, pp. 3597-3610, 2017.

[2] Shkolyar, S., Eshelman, E.J., Farmer, J.D., Hamilton, D., Daly, M. G., Youngbull, C.: Detecting Kerogen as a BiosignatureUsing Colocated UV Time-Gated Raman and Fluorescence Spectroscopy, Astrobiology, Vol.18, pp. 431-453, 2018.

[3] Schito, A., Romano, C., Corrado, S., Grigo, D., Poe, B.: Diagenetic thermal evolution of organic matter by Raman spectroscopy, Organic Geochemistry, Vol. 106, pp. 57-67, 2017.

[4] Tuschel, D.: Raman spectroscopy of oil shale, Spesctroscopy, Vol. 28 (3), 2013.

[5] Childress, L.B., Jacobsen, S.D.: High-pressure high-temperature Raman spectroscopy of kerogen: Relevance to subducted organic carbon, American Mineralogist, Vol.102, pp. 391-403, 2017.

EPSC Abstracts
Vol. 12, EPSC2018-986, 2018
European Planetary Science Congress 2018

Impact vaporization and condensation of planetary materials in laser irradiation experiments

Christopher Hamann (1), Lutz Hecht (1,2), Sebastian Schäffer (3), Dominic Heunoske (3), Tobias Salge (4), Ansgar Greshake (2), Amin Garbout (4), and Jens Osterholz (3)
(1) Museum für Naturkunde Berlin, Germany, (2) Freie Universität Berlin, Germany, (3) Fraunhofer Ernst-Mach-Institut, Freiburg, Germany, (4) The Natural History Museum, London, UK (christopher.hamann@mfn.berlin)

Abstract

Petrologic investigation of laser-generated vapor condensates suggests that impact vapors formed in small-scale (decimeter-size) impact scenarios deposit upon cooling fluffy, fine-grained mixtures of condensate nanoparticles and crystallites. In keeping with findings from lunar condensates and previous experiments, condensate deposits are compositionally complementary to residual melts, and individual condensate sequences evolve from more refractory to more volatile compositions.

1. Introduction

Hypervelocity impacts of asteroids and comets typically induce melting and vaporization of materials close to the point of impact, and may result in a vapor plume that subsequently condenses after reaching the liquid–vapor coexistence curve [1]. Due to their rarity and susceptibility to alteration, products of impact vaporization and condensation have rarely been studied in nature (e.g. [2]), and, with some exceptions (e.g., [3]), most previous experiments have focused on thermodynamics of vaporized materials (e.g., [4]) Here, we investigate mineralogy and composition of laser-generated condensates formed from chondritic, basaltic, dioritic, and granitic compositions to constrain mineralogy and composition of impact-generated condensates formed from similar materials.

2. Methods

We used a continuous-wave (CW) fiber laser (1.07 µm, 2.2×10^5 W cm^{-2}) and similar methods as described in [5] to melt and vaporize natural planetary rocks (Hammadah al Hamra 077 chondrite, basalt, diorite, gabbro, and granite) at 1 bar and room temperature. The resulting condensates precipitated by the vapor plumes were sampled by witness plates (aluminium metal or ceramics) positioned opposite–parallel to the target surface at distances of 1–3 cm. Textural and compositional characterization of the condensates and melts employed field-emission scanning electron microscopy (SEM), low-voltage energy dispersive spectroscopy (EDX), and 3D X-ray microscopy (CT).

3. Results and discussion

Laser irradiation of the samples resulted in formation of self-luminous vapor plumes that precipitated onto the witness plates macroscopically white (silicate starting materials) or tan to dark brown (HaH 077 starting material), fine-grained, fluffy coatings or layers. The laser also excavated melt droplets of sub-micrometer to millimeter diameters that were subsequently also coated by condensate layers. SEM and CT imaging reveals that the condensate coatings consist of fluffy, dust-like, globular, ~100-nm-diameter nanoparticles that accreted to continuous, chemically alternating sequences or layers. SEM-EDX point analyses and X-ray maps indicate that with decreasing depth, individual condensate sub-layers evolve from more refractory to more volatile (e.g., from Si-rich to Na-rich) compositions. In terms of bulk composition, the condensate layers are depleted in refractory elements (e.g., Ca, Al, Mg) and enriched in volatile elements (e.g., P, K, Na), whereas the residual melts are enriched in refractory elements and depleted in volatile elements. Moreover, we detected platy to acicular, idiomorphic crystallites—presumably sodium sulfate and Cr-spinel—of 2–5 µm size interbedded into rod-shaped aggregations of nanoparticles in some experiments (e.g., gabbroic starting composition).

Following methods outlined in [5], we estimate that the irradiation intensities used in our study result in

entropy increases that correspond to impact velocities in the range of 10 to some 25 km/s. The condensate deposits produced here share similarities to materials formed in previous experiments that used pulsed laser irradiation [3], and the major element chemistry of our condensate deposits as well as our residual melts are consistent with trends encountered in the lunar HASP and GASP [2] glasses as well as in Joule melting experiments [6]. These findings confirm that condensates and residual melts are compositionally complementary, and that impact vaporization, even in small-scale (decimeter-size) impact scenarios, results in significant element fractionation.

Figure 1 (right): CT (a) and SEM-BSE (b, c) images of vapor deposits and residual melts; (d) vapor deposits in thin section; (e) X-ray map of several condensate sequences deposited onto residual melts; (f) bulk compositions of condensates and melts compared to residual melts of [6].

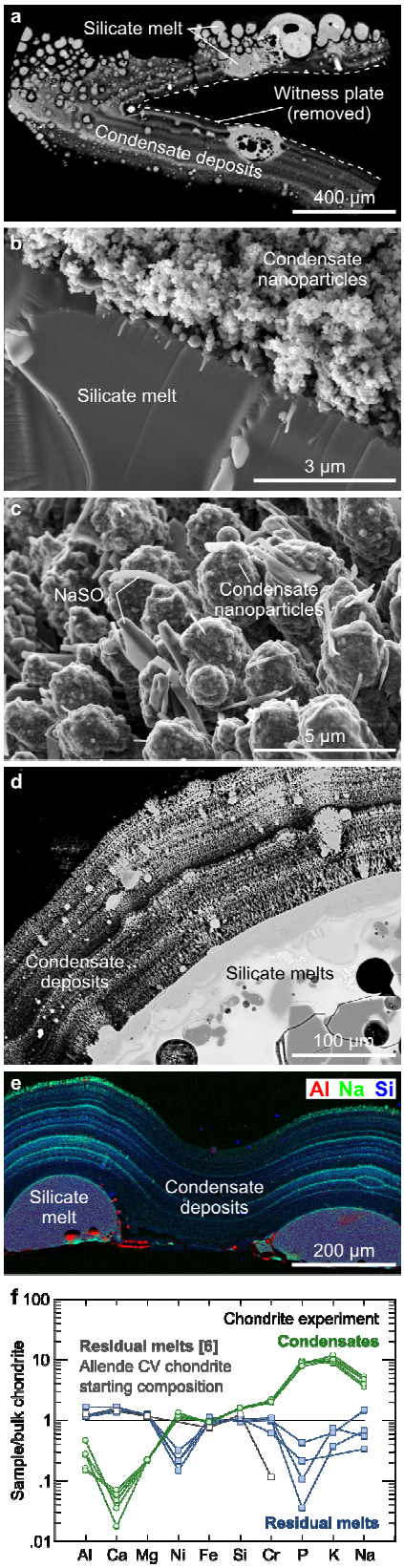

Acknowledgements

This work was supported by a Europlanet 2020 RI TA Grant to CH and LH and a MfN Innovation Funds Grant to CH. Europlanet 2020 RI has received funding from the European Union's Horizon 2020 research and innovation program under grant agreement No 654208.

References

[1] Svetsov, V. V. and Shuvalov, V.: Silicate impact-vapor condensate on the Moon: Theoretical estimates versus geochemical data, Geochim. Cosmochim. Acta, Vol. 173, pp. 50–63, 2016.
[2] Warren, P. H.: Lunar rock-rain: Diverse silicate impact-vapor condensates in an Apollo-14 regolith breccia, Geochim. Cosmochim. Acta, Vol. 72, pp. 3562–3585, 2008.
[3] Gerasimov, M. B. V., Ivanov, B. A., Yakovlev, O. I., and Yu, P.: Physics and chemistry of impacts, Earth Moon Planets, Vol. 80, pp. 209–259, 1998.
[4] Kadono, T., Sugita, S., Mitani, N. K., Fuyuki, M., Ohno, S., Sekine, Y., and Matsui, T.: Vapor clouds generated by laser ablation and hypervelocity impact, Geophys. Res. Lett., Vol. 29, pp. 40-1–40-4, 2002.
[5] Hamann, C., Luther, R., Ebert, M., Hecht, L., Deutsch, A., Wünnemann, K., Schäffer, S., Osterholz, J., and Lexow, B.: Correlating laser-generated melts with impact-generated melts: An integrated thermodynamic–petrologic approach, Geophys. Res. Lett., Vol. 43, pp. 10602–10610, 2016.
[6] Floss, C., El Goresy, A., Zinner, E., Kransel, G., Rammensee, W., and Palme, H.: Elemental and isotopic fractionations produced through evaporation of the Allende CV chondrite: Implications for the origin of HAL-type hibonite inclusions, Geochim. Cosmochim. Acta, Vol. 60, pp. 1975–1999, 1996.

EPSC Abstracts
Vol. 12, EPSC2018-1040, 2018
European Planetary Science Congress 2018

Formation of nanoscopic Lingunite and alternating augite-plagioclase wedges at Lockne impact crater, Sweden

Amar Agarwal 1, Boris Reznik 2 and Agnes Kontny 3
[1]Institut für Geo- und Umweltnaturwissenschaften, Albert-Ludwigs-Universität Freiburg, Albertstraße 23b, 79104 Freiburg, Germany (amar@daad-alumni.de)
[2]Division of Structural Geology and Tectonophysics, Institute of Applied Geosciences, Karlsruhe Institute of Technology, Karlsruhe 76131, Germany.

Abstract

The study reports peculiar alternating augite-plagioclase wedges, Lingunite nanocrystals and amorphous plagioclase (maskelynite) in basement dolerites of Lockne impact structure, Sweden. Classical optical microscopy is coupled with spectroscopy and high resolution electron microscopy. The results reveal that the wedges develop from the {110} prismatic cleavage of augite, as they are filled with molten labradorite pushed from the neighboring bulk labradorite grain. The occurrence of lingunite suggests that the local pressure was above 19 GPa and the local temperature overwhelmed 1000 °C. These values are up to 10 times higher than previous values estimated numerically for bulk pressure and temperature.

1. Introduction

This study investigates wedges developed at the augite-plagioclase grain boundary in the doleritic in situ basement rocks of the Lockne impact structure, Sweden. The combined microscopic and spectroscopic studies of the micro/nanoscale wedges reveal that these are deformation-induced features. Further investigations lead to identification of Lingunite nanocrystals and amorphous plagioclase (maskelynite) at the wedge boundaries. The samples showing wedges, 12 out of 18 studied, are distributed in the impact structure within a radius of up to 10 km from the crater center. The margins between the augite and labradorite wedges are sharp and the {110} prismatic cleavage of augite develops into fractures and thereafter into wedges. The fractures are filled with molten labradorite pushed from the neighboring bulk labradorite grain. Compared to the bulk labradorite, the dislocation density and the residual strain in the labradorite wedges are significantly higher. Furthermore, the occurrence of lingunite suggests that the local pressure was above 19 GPa and the local temperature overwhelmed 1000 °C. High shock-induced temperatures are manifested by maskelynite injections into microfractures in augite located next to the wedges. We discuss a possible model of shock heterogeneity at mineral interfaces, which formed the wedges and may lead to longer duration of the same shock pressure and a concentration of high temperature thus triggering the kinetics of labradorite transformation into lingunite and maskelynite.

2. Figures

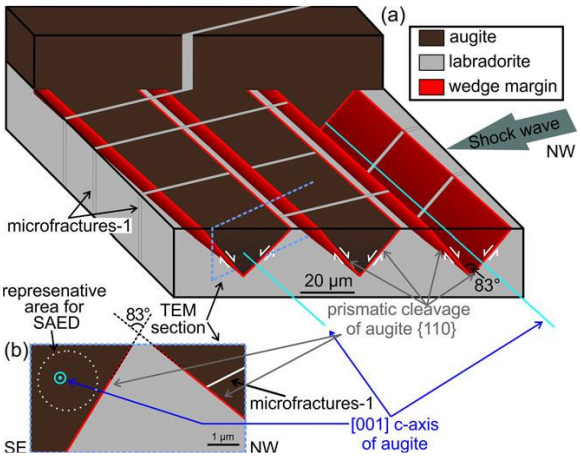

Schematics of the wedges and crystallographic features of augite. The microfractures-1, the {110} prismatic cleavage developing into planar fractures, and the c-axis [001] of augite are shown. The blue dashed line represents orientation and position of the TEM section. Note that the figure reconstructs the geometry of the wedges at the augite-labradorite grain boundary. In nature, augite covers the entire

wedges. However, if the figure shows a complete augite grain, it would be impossible to visualize the microstructure of the wedges. Therefore, for proper visualization of the wedges, augite is shown only as a thin layer and is not covering the wedges [1].

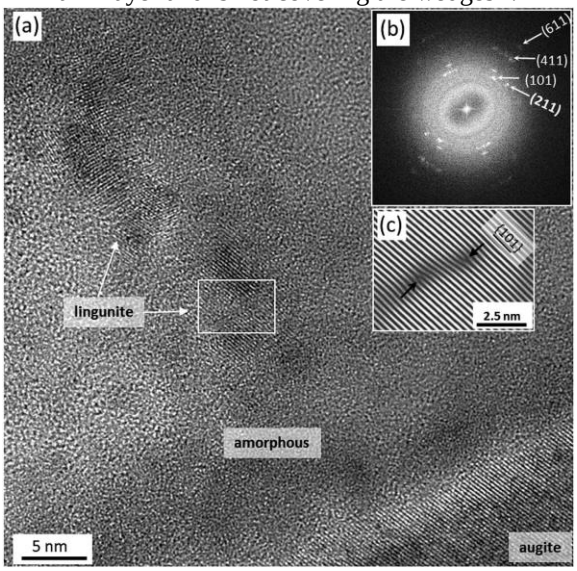

Figure 2: HRTEM analysis of the augite-labradorite wedge interface. (a) Well-crystallized augite (rightdown)and amorphous matrix containing lingunite nanocrystals. (b) FFT pattern from a lingunite area. Numbers indicate indices of Bragg reflection planes. (c) IFFT pattern of the area in the white frame displaying two edge dislocations (s. black arrows) in {101} planes[2].

3. Summary and Conclusions

The shock waves caused fracturing of the augite grain along its prismatic cleavage planes and motored injection of the melt labradorite into the fractures. We infer that the shock waves may induce deformation structures with complex geometries, such as alternating wedges. Transformation of plagioclase into lingunite is accompanied by amorphization of the plagioclase. It is noteworthy that, even though there are 188 confirmed impact structures on Earth[3], many with feldspar bearing target rocks, there is only one short report on silicate-hollandite in a target rock of the Manicougan impact structure[4]. To our knowledge, transformation of plagioclase into high pressure polymorphs, due to reverberations of shock-wave at heterogeneous mineral interfaces has not been reported so far.

Acknowledgements

We thank E. Sturkell, E. Müller and H. Strömer. Alexander von Humboldt s thanked for the financial support of the first author (file number: A/11/76052). TEM and SEM investigations were funded from DFG project KO1514/8.

References

[1] Agarwal, A., Reznik, B., Alva-Valdivia, L. M. and Srivastava, D. C: Alternating augite-plagioclase wedges in basement dolerites of Lockne impact structure, Sweden: A new shock wave-induced deformation feature. Meteoritics & Planetary Science. Vol. 52**,** pp. 458–470, 2016.

[2] Agarwal, A., Reznik, B., Kontny, A., Heissler, S. and Schilling, F.: Lingunite-a high-pressure plagioclase polymorph at mineral interfaces in doleritic rock of the Lockne impact structure (Sweden). Scientific Reports. 6, 25991, 2016.

[3] Spray, J. and Hines, J. Earth impact database. Planetary and Space Science Centre, University of New Brunswick, Canada. Available at: http://www.passc.net/EarthImpactDatabase/.

[4] Langenhorst, F. and Dressler, B. First observation of silicate hollandite in a terrestrial rock. in Large Meteorite Impacts III (eds. Kenkmann, T., Hörz, F. & Deutsch, A.) 4046–4047 (Geological Society of America, 2005)

EPSC Abstracts
Vol. 12, EPSC2018-1049, 2018
European Planetary Science Congress 2018

Origin of melt heterogeneities in Ries impact breccia

Susann Siegert (1,2) and Lutz Hecht (1,2)
(1) Museum für Naturkunde, Leibniz-Institut für Evolutions- und Biodiversitätsforschung, Invalidenstr. 43, 10115 Berlin, Germany (2) Freie Universität Berlin, Institut für Geologische Wissenschaften, Malteserstr. 74-100, 12249 Berlin, Germany (susann.siegert@mfn.berlin)

Abstract

New detailed textural and chemical investigation of melt-bearing impact breccias (suevites) reveal that they contain three melt types which represent the sequence of successively decreasing shock pressure: whole-rock melting, partial melting of a certain volume of rocks, with variations of mixing of monomineralic melts. Trace element analysis of melts allow to distinguish between melts from different regions of the crater recording primary heterogeneities in the target. This improves our understanding of the origin and emplacement of melt-bearing impact breccias.

Introduction

Suevites in the Ries impact structure were in focus of many previous studies [7, and references therein]. In particular melt particle in suevite were used for genetic statements of the origin and emplacement of suevite, and for estimation of involved lithologies at impact melt formation. Despite noted heterogeneities at the sub-centimeter scale, the conclusions are very similar from homogeneous to nearly homogeneous in terms of major element composition [e.g., 6, 8] by melting of ca. 20% to 40% amphibolite and 60% to 80% granites [2, 4, 8]. This has been considered consistent with findings at other impact structures where impact melt often displays chemical homogeneity [1].

However, trace element studies have shown that there may be variabilities in impact melts [3]. The Ries suevite melt particles have been revisited in consideration of major and trace element chemistry. The results provide information about their origin and subsequent emplacement processes [5].

Results and Discussion

Three melt types have been identified based on petrographic, geochemical information, and degree of rock melting. The most common and volumetrically abundant melt is the whole rock melt 1.

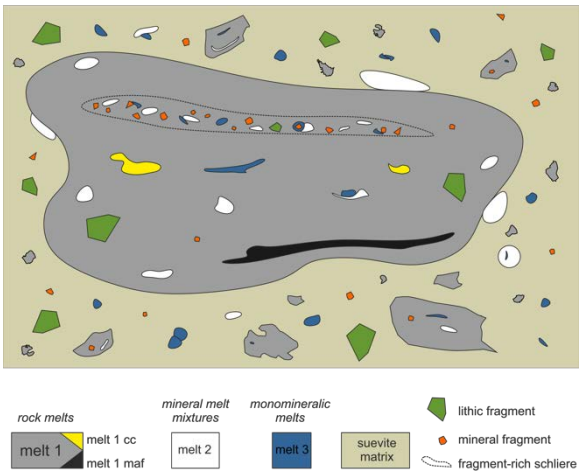

Figure 1: Sketch of suevite with identified melt types.

Characteristically are schlieren in melt 1 by mafic rock melts and occasionally occurring of in emulsion carbonate melts. Mineralic melt mixtures (melt 2) and monomineralic melts (melt 3) occurs attached to or within melt 1 particles or embedded in the suevite matrix (Fig. 1). Melt 1 types represents whole rock melting and therefore is much more homogeneous in composition than melt 2 and 3 (Fig. 2). Hydrothermal activity and/or weathering led to alteration of all melt types at many suevite deposits. Using isocon method show that there was significantly mass transfer in most major and many trace elements. However, the high field strength elements Zr, Nb, Hf, Th, Ta, V, and Ti were mostly immobile. These elements are most suitable to study the origin and emplacement of the impact melt-bearing breccias. Significant

differences exist mainly in trace element composition between melt 1 particles of suevite locations in the East and West of the crater. This reflects probing of chemically different target lithologies during cratering [5]. The consideration of trace elements and the separate evaluation of melts from suevite from two different regions of the crater allow a more precise estimation of the relative amount of various crystalline basement rocks involved in the formation of the major melt particles (melt 1). In the western area gneisses and granitoids represent 91%, schist 1%, and mafic rocks 8%. In the eastern area gneisses and granitoids represent 89%, schist 3%, and mafic rocks 8%.

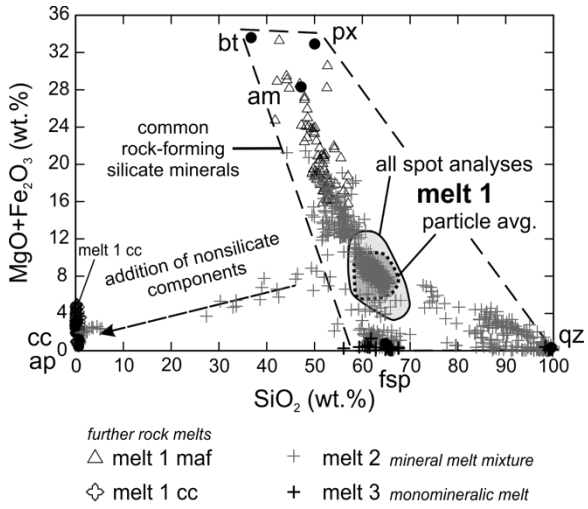

Figure 2: Major element geochemistry of melt types.

Acknowledgements

We thank G. Pösges and M. Branney for discussion in the field, and S. Sindern (LA-ICP-MS) for laboratory assistance.

References

[1] Dressler, B. O., and Reimold, W. U.: Terrestrial impact melt rocks and glasses, Earth-Science Reviews, Vol. 56, pp. 205-284, 2001.

[2] Engelhardt, W. v.: Shock produced rock glasses from the Ries crater, Contributions to Mineralogy and Petrology, Vol. 36, pp. 265-292, 1972.

[3] Marion, C. L., and Sylvester, P. J.: Composition and heterogeneity of anorthositic impact melt at Mistastin Lake crater, Labrador, Planetary and Space Science, Vol. 58, pp. 552-573, 2010.

[4] Osinski, G. R.: Impact glasses in fallout suevites from the Ries impact structure, Meteoritics & Planetary Science, Vol. 38, pp. 1641-1667, 2003.

[5] Siegert, S., Branney, M. J., and Hecht, L.: Density current origin of a melt-bearing impact ejecta blanket (Ries suevite, Germany), Geology, Vol. 45, pp.855-858, 2017.

[6] Stähle, V.: Impact glasses from the suevite of the Nördlinger Ries, Earth and Planetary Science Letters, Vol. 17, pp. 275-293, 1972.

[7] Stöffler, D., Artemieva, N. A., Wünnemann, K., Reimold, W. U., Jacob, J., Hansen, B. K., and Summerson, I. A.: Ries crater and suevite revisited – Observations and modeling Part I: Observations, Meteoritics & Planetary Science, Vol. 48, pp. 515-589, 2013.

[8] Vennemann, T. W., Morlok, A., von Engelhardt, W., and Kyser, K.: Stable isotope composition of impact glasses from the Nördlinger Ries impact crater, Germany, Geochimica et Cosmochimica Acta, Vol. 65, pp. 1325-1336, 2001.

EPSC Abstracts
Vol. 12, EPSC2018-1087, 2018
European Planetary Science Congress 2018

Kärdla impact crater – transitional from simple to complex based on reflection seismics

Argo Jõeleht, **Jüri Plado**, Kaidi Sarv
Department of Geology, University of Tartu, Estonia (argo.joeleht@ut.ee, juri.plado@ut.ee, kaidisarv@gmail.com)

Abstract

Based on drillings, the 4 km Kärdla impact crater is considered as one of the smallest complex craters on Earth in crystalline target. We present results of reflection seismic profiling indicating only a small hill near the crater center. Weakly developed central uplift is likely related to incomplete collapse of crater cavity.

1. Introduction

Kärdla impact crater, Estonia, is known as one of the smallest complex craters on Earth that was formed in crystalline rocks. The crater, rim-to-rim diameter about 4 km, was formed in shallow marine environment [3]. Crater rim was partly eroded by resurging sea, but in general it is well preserved. The complex nature of the Kärdla crater is based on three boreholes inside of the crater. A drillhole K18, located near its center (Fig. 1), revealed existence of the central uplift as suevitic breccia and strongly fractured crystalline basement rocks lie more than 150 m higher in comparison to boreholes K1 and K12 in the annular moat. We present results of reflection seismic survey that provides more information on the size and location of the central uplift.

2. Methods

Internal structure of the Kärdla crater was studied using 24-channel system. In total about 20 km of profiles covered both central part and rim area of the crater (Fig 1). Geophone spacing was 10 m. Limited number of channels available (relatively short receiver line) and variable burial depth (<100 m at rim, >300 m at central part) created acquisition configuration challenges in order to illuminate both rim and central areas of the crater. In the rim area, where the crystalline rocks were not deep, the source (8 kg sledge hammer) was applied in-line at 10 m spacing with maximum near-offsets ranging 10-120 m, after which receiver line was moved by 12 channels. In the central part and some parts with lower crystalline rim, the source was applied every 20 m at near-offset range 10(20) to 230(240) m. Thus, the maximum offsets were 350 or 470 m.

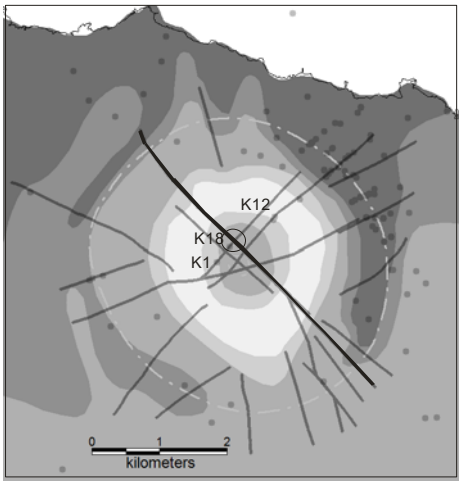

Figure 1: Location of seismic profiles (gray lines) and boreholes (dots). Crater rim and its small projection in the center are marked by dot-dash line. Central mound on Fig 2 is marked with black circle. Black line marks the profile on Fig 2. Background is bedrock geology map.

Data were processed using SeismicUnix package [1]. Apart of typical reflection seismic processing flow, the Kirchhoff pre-stack depth migration was applied.

3. Results

Seismic profiles suggest that the crater is not quite symmetric in many aspects. The central uplift is laterally rather small feature that is located 300–400 m northward from its expected location at the center of the crater (Fig. 2). This mound is visible only on two crossing profiles near borehole K18 whereas other profiles in the central part of the crater show no

uplifted basement rocks or bending of overlaying strata. Small central uplift is in agreement with gravity data. The lack of positive gravity anomaly in the center was attributed to small density contrast between uplifted rocks and surrounding crater fill [2].

The crater is also asymmetric in the shape and height of the rim. The rim is slightly elongated in NW-SE direction (diameter 4.5 km in NW direction versus 4.1 km in NE). A high rim occurs extensively only in the (north)eastern side whereas there are some smaller peaks in southwest and northwest. Low rim in northern and southern parts have been interpreted as resurge gullies [3]. Drillings at western rim show also erosional features, but no gully-like cut-in features which might suggest that the rim has never been high there. Rim height variations might be related to changes in rock types as amphibolitic and granitic rocks prevail in the western and eastern rims, respectively.

4. Summary and Conclusions

Seismic reflection profiles indicate only a small central uplift in the Kärdla crater. The uplift is 300–400 m off the center. It is interpreted as result of partial collapse of crater resulting in under-developed central uplift. Variable collapse of crater cavity might have been controlled by lithological changes in crystalline basement.

Acknowledgements

We are greatful to all who participated in field works. This research was funded grant 5851 by ETF and grant IUT20-34 by Estonian Research Council.

References

[1] Cohen, J.K. and Stockwell, Jr. J.W.: CWP/SU: Seismic Unix Release 36: a free package for seismic research and processing. Center for Wave Phenomena, Colorado School of Mines, 2002.

[2] Plado, J., Pesonen, L.J., Elo, S., Puura, V. and Suuroja, K.; Geophysical research on the Kardla impact structure, Hiiumaa Island, Estonia, Meteoritics & Planetary Science, Vol. 31, pp. 289–298, 1996.

[3] Puura, V. and Suuroja, K.: Ordovician impact crater at Kärdla, Hiiumaa island, Estonia, Tectonophysics, Vol. 216, pp. 143-156, 1992.

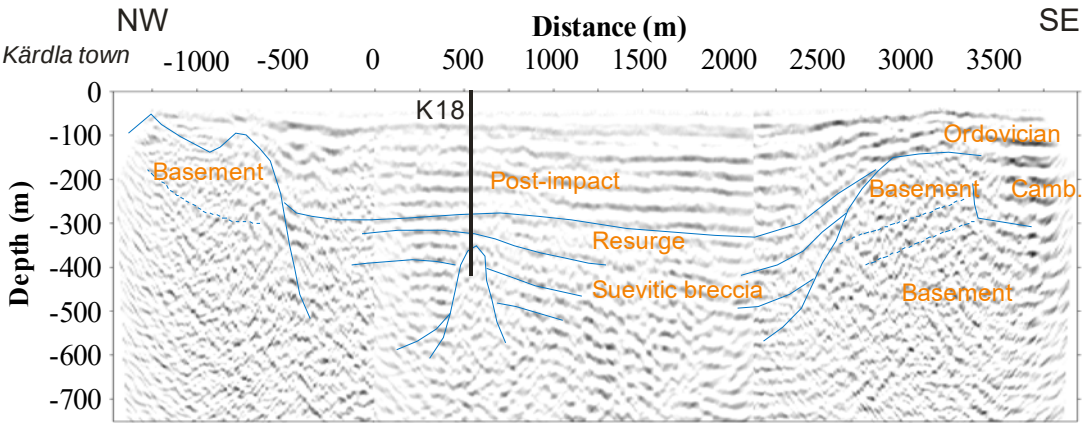

Figure 2: Reflection seismics profile with interpretations. Location is shown in Fig. 1.

EPSC Abstracts
Vol. 12, EPSC2018-1111-2, 2018
European Planetary Science Congress 2018

An integrated CL, SEM, and optical microscopy study of carbonate impact melts in the Ries suevites

Christopher Hamann (1), Lutz Hecht (1,2), Saskia Bläsing (2), and Sanni Siegert (1,2)
(1) Museum für Naturkunde Berlin, Germany, (2) Freie Universität Berlin, Germany (christopher.hamann@mfn.berlin)

Abstract

We present a petrographic study of fluidal-shaped carbonate blebs disseminated in pristine silicate glasses in the suevites of the Ries crater, Germany, to contribute to the ongoing discussion on the nature of such textures. In particular, cathodoluminescence imaging reveals potential nucleation sites and crystallization histories of fluidal-shaped carbonates, suggesting that they indeed represent quenched primary impact melts.

1. Introduction

One of the unique consequences of hypervelocity impacts of asteroids and comets is the production of impact melts that form during pressure release from both the projectile and specific parts of the target. While the response of silicate rocks and minerals to shock compression and decompression are well understood, the question of whether carbonates melt or decompose if released from high shock pressures (>50–70 GPa, i.e., sufficiently high to melt coexisting silicates) remains contentious [1,2]. Specifically, the canonical view that carbonates decompose upon impact has been challenged in recent years by observations on terrestrial impactites [3–5] and results from numerical modeling [6] which cumulatively suggest that calcite impact melts may indeed readily form in typical impact scenarios.

Several studies have characterized potential impact-generated carbonate melts by means of optical or scanning electron microscopy (SEM) [3–5]. The salient point of these studies is the observation of textures indicative of liquid immiscibility between carbonate and silicate melts. Here, we return to the original description of potential carbonate impact melts by [3,5] and present a cathodoluminescence (CL), SEM, and optical microscopy characterization of fluidal-shaped carbonates in the suevites of the Ries crater, Germany.

2. Results and discussion

Carbonate-bearing suevite specimen were collected by S. Siegert during several field trips to the Ries. In the present study we focus on the suevites from Aufhausen, Bollstadt, and Otting, which are known to typically and abundantly bear fluidal-shaped or globular calcite disseminated in pristine silicate impact glass [3,5]. Following thin sectioning, the suevite samples were investigated using a combination of optical microscopy, CL, and SEM methods at Museum für Naturkunde Berlin.

Textures indicative of liquid immiscibility between primary carbonate and silicate impact melts were frequently encountered in all our samples. They are similar to the textures described by [3–5] and comprise carbonate (generally calcite) globules, blebs, and schlieren in pristine silicate glass (Fig. 1a–c). Often, the carbonate shows distinct amounts of Si and Al in SEM-EDX analyses; the surrounding silicate glass is, in some cases, complementarily and locally enriched in Ca. The interfaces between the two phases are always sharp compositional and mineralogical boundaries (Fig. 1d), reminiscent of menisci formed by silicate–silicate liquid immiscibility. Interestingly, the carbonate is almost always separated from the silicate by thin rims of phyllosilicate (presumably montmorillonite; cf. [3,5]). Furthermore, sub-micrometer size crystallites of presumably Ca,Mg-rich composition have nucleated in the silicate glass close to the phase boundary (Fig. 1d). Often, pristine silicate glass exists in the form of droplets and blebs in large carbonate bodies (Fig. 1b, c); the interface between these two phases is again sharp but decorated by rims of phyllosilicate (Fig. 1e). Occasionally, textures indicative of carbonate degassing (i.e., vesicles, fading grain boundaries) were observed that are similar to those recently described by [7]; in other cases, fluidal-shaped carbonate entrained in silicate glass contains fossils similar to those encountered in the pre-impact

limestone of the Ries target. The fluidal-shaped carbonate blebs often show feathery crystals habits (Fig. 2a) indicative of rapid quenching [3], and likewise feathery, predominantly orange luminescence patterns that originate from round, concentric, poorly luminescing spots that are localized close to the coexisting silicate glass (Fig. 2b). Together with the feathery crystal habit, we interpret such CL patterns as nucleation seeds from which crystallization of the material started. In the case of large carbonate blebs, we observed several of these sites, suggesting that nucleation of large volumes of carbonate started simultaneously at multiple locations. In agreement with previous studies [3,5], these findings suggest that the fluidal-shaped, feathery carbonates in the Ries suevites indeed represent quenched primary impact melts.

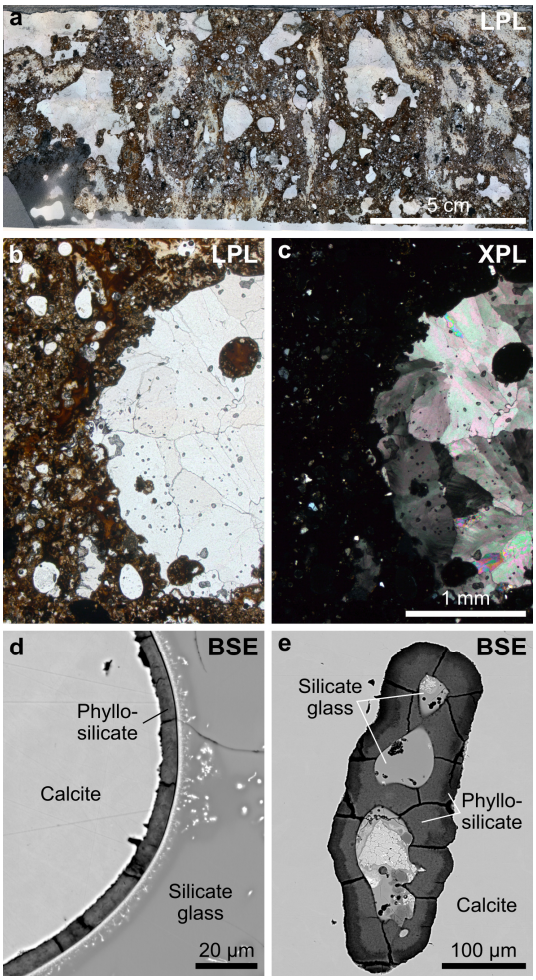

Figure 1: Optical photomicrographs (a–c) and BSE images (d, e) of carbonate impact melts in the Aufhausen suevite.

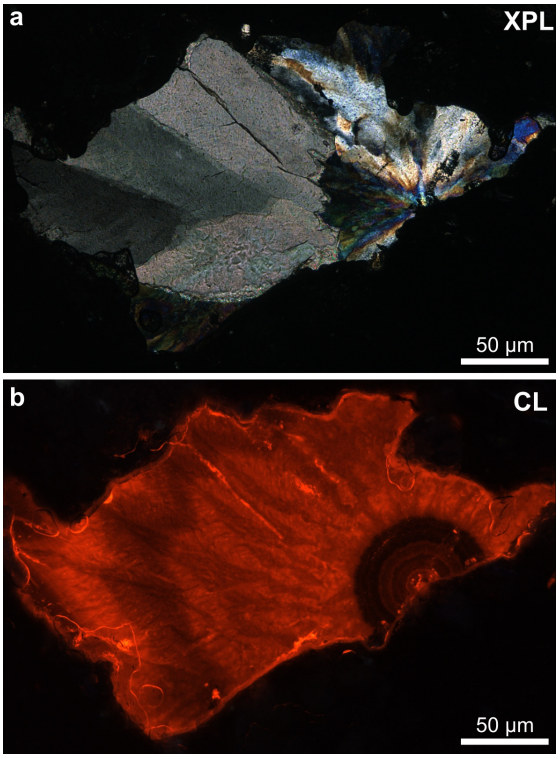

Figure 2: Optical photomicrograph (a) and corresponding CL image (b) of rapidly quenched carbonate impact melt in the Aufhausen suevite.

References

[1] Hörz, F., Archer, P. D. Jr., Niles, P. B., Zolensky, M. E., and Evans, M.: Devolatilization or melting of carbonates at Meteor Crater, AZ? Meteorit. Planet. Sci., Vol. 50, pp. 1050–1070, 2015. [2] Osinski, G. R., Bunch, T. E., Flemming, R. L., Buitenhuis, E., and Wittke, J. H.: Impact melt- and projectile bearing ejecta at Barringer Crater, Arizona, Earth Planet. Sci. Lett., Vol. 432, pp. 283–292, 2015. [3] Graup, G.: Carbonate–silicate liquid immiscibility upon impact melting: Ries Crater, Germany, Meteorit. Planet. Sci., Vol. 34, pp. 425–438, 1999. [4] Osinski, G. R., Spray, J. G., and Grieve, R. A. F.: Impact melting in sedimentary target rocks: an assessment, Geological Society of America Special Paper, Vol. 437, pp. 1–17, 2008. [5] Osinski, G. R.: Impact glasses in fallout suevites from the Ries impact structure, Germany: An analytical SEM study, Meteorit. Planet. Sci., Vol. 38, pp. 1641–1667, 2010. [6] Ivanov, B. A. and Deutsch, A.: The phase diagram of $CaCO_3$ in relation to shock compression and decomposition, Phys. Earth Planet. Inter., Vol. 129, pp. 131–143, 2002. [7] Walton, E. L., Timms, N. E., Hauck, T. E., MAcLagan, E. A., and Herd, C. K. D.: Evidence for melting and decomposition of sedimentary target rocks from the Steen River impact structure, Alberta, Canada, 49th LPSC, Abstract #2330.

EPSC Abstracts
Vol. 12, EPSC2018-1175-1, 2018
European Planetary Science Congress 2018

Post Impact Hydrothermal Activity. Thermodynamic Simulations on the Chicxulub Crater & Habitability Assessment.

Evangelos Christou (1), Wolfgang Bach (2)

(**1**,2) MARUM - Center for Marine Environmental Sciences and Faculty of Geosciences, University of Bremen, Germany (christev@uni-bremen.de)

Abstract

Large asteroid and comet impacts on terrestrial planets and moons deliver vast amounts of heat that drive hydrothermal activity. Such hydrothermal processes subsequently raise probabilities for life evolution beneath planetary surfaces in the Solar System. We use the Chicxulub crater setting to model the thermodynamic evolution of the impact induced hydrothermal system. Data from the recent M0077A borehole samples of the IODP 364 Expedition and other seismic, magnetic and gravity surveys constrain our model inputs. As the impact induced central melt sheet gradually cools and crystallizes, it allows fluids to flow through it. Rock permeability is the determining factor of fluid circulation and lifetimes of hydrothermal systems. According to the assumed permeability, we found that the hydrothermal upwellings at Chicxulub were active for more than 2 Myr. Furthermore, the distributions of temperature and water mass flux along the Chicxulub crater and its annular trough allow us to proceed with the thermodynamic modelling of the geochemical reaction paths and to investigate potential energy metabolism pathways. Through this model, we assess habitability at the Chicxulub crater by (hyper) thermophiles / thermoacidophiles for the period of the impact-induced hydrothermal activity. As a result, we favor the application of the suggested model to habitability scenarios of fresh impact craters in the Solar System.

1. Introduction

Large impacts into planetary crusts, like the one that formed the Chicxulub crater, deliver vast amount of energy, some of which is converted into heat. Sufficient heat is deposited by the shock wave to induce phase changes, melting and vaporization of target rocks. As a consequence, such impacts can produce even km3 of liquid melt that take a long time to cool. The impact induced melt pools in the topographically lowest regions of the crater basin, forming a melt sheet. The final heat source is the central uplift, or material that has been uplifted from warmer regions of the crust during the crater formation process. The importance of the melt sheet and the central uplift, relative to shock emplaced heat, increases with crater diameter [6]. If water or ice is present in the crust, the resulting temperature increase provides a thermal driver for the circulation of water and the emission of steam, initiating a hydrothermal system [3].

Studies of terrestrial craters reveal three important features of impact-generated hydrothermal systems:

1. The volume affected by hydrothermal activity extends laterally across the entire diameter of a crater (more than 200 km in the Chicxulub Crater) and to depths of several kilometers [7].

2. Impact induced hydrothermal systems have the capacity to significantly redistribute chemical elements and create chemical gradients throughout equally large volumes of the Earth's crust.

3. In these systems we observe the same biogeochemical features as in volcanically driven hydrothermal systems and hence, may have influenced the biological evolution of Earth [3].

1.1 Sub-section: Modelling the Impact Induced Hydrothermal Activity at the Chicxulub Crater

The Chicxulub crater has been extensively studied through seismic, magnetic and gravity surveys, more significantly through several drilling expeditions for research or industrial purposes. Especially, borehole data and previously collected samples of the Chicxulub Scientific Drilling Project and the most recent joint IODP/ICDP 364 Expedition allow us to construct an enhanced numerical model of the post impact generated hydrothermal activity. Modelling the post impact water and heat flow at Chicxulub crater required formulation of the numerical code HYDROTHERM, which is a three dimensional finite difference model developed by the U.S. Geological Survey. It is mainly used to simulate water and heat transport in a porous medium [4] and has been previously applied to hydrothermal systems of volcanic origin [5] and hydrothermal systems at several Martian impact craters [2], [8] and impact craters on Earth eg. Sudbury impact [1] and Chicxulub [3].

2. Preliminary Results

Subsequently, after setting the boundary conditions, model inputs and physical parameters, according to [3], feasibility tests via HYDROTHERM simulations took place and are presented as follows. Our simulations (Figures 1 and 2) are in compliance with previous results presented in [3] and prove that we can rely on this model. After constructing the 3D physical model of the temperature, pressure and water mass flux distributions versus time for the Chicxulub crater, a homogenous data catalogue of the physical properties of the simulated hydrothermal system is produced. These data are used anew to provide geochemical reaction paths and to investigate the metabolic energy potential across the entire diameter of the crater and its annular trough.

3. Figures

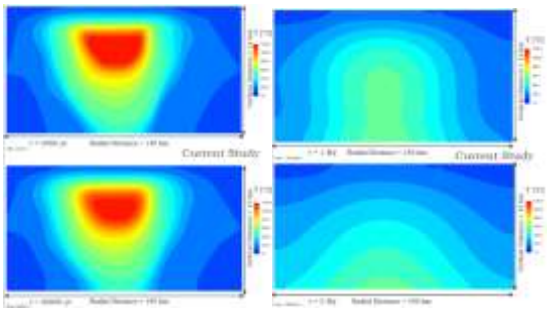

Figure 1: Temperature distributions at the Chicxulub Crater (2000yr, 20.000yr, 1My and 2My after the impact). Red colours represent isotherms of T > 1200°C, yellow of T = 800°C, dark blue of T = 50°C.

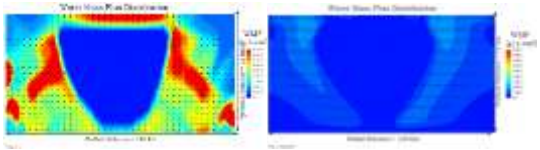

Figure 2: Water Mass Flux distributions at the Chicxulub Crater (2000yr and 2My after the impact). Red colours represent Water Mass Flux WMF > 7.0E-6 kg/s×m2, dark blue of WMF < 0.5E-6 kg/s×m2.

4. Summary and Conclusions

The cutting edge of this research work is to simulate via deterministic modelling the thermodynamics, lifetimes and mechanics of impact induced hydrothermal systems and essentially, to provide geochemical constraints and suggest potential energy metabolism pathways. Several studies provide models of impact induced hydrothermal systems on Earth [1], [3] and on Mars [2], [8] focusing on the lifetimes of such systems, the temperature and water/vapor mass flux distributions. Nevertheless, the geochemical constraints and the biological potential of impact induced hydrothermal systems still remain unknown. Through this study, we use data deriving from our constructed 3D thermodynamic model of the impact induced hydrothermal system at Chicxulub to examine the geochemical reaction paths that took place. These geochemical constraints should also explain the mineralogical distribution and hydrothermal alteration observed at samples of the Chicxulub crater. We continue by exploring specific regions of the simulated hydrothermal setting of the

Chicxulub crater, where the thermodynamic conditions (temperature, pressure) and water flows would allow (hyper) thermophilic life to thrive. Consequently, we use the physical conditions and geochemical compositions of these areas of particular interest to define the metabolic energy potential therein. Hence, through modelling the thermodynamics and the biogeochemical reaction paths of the impact induced hydrothermal system at the Chicxulub crater, we expect to shed new light on the metabolic energy potential and the astrobiological implications of fresh impact craters in the Solar System.

References

[1] Abramov O. and Kring D.A.: Numerical modeling of an impact-induced hydrothermal system at the Sudbury crater, Journal of Geophysical Research, 109, 2004.

[2] Abramov O. and Kring D.A.: Impact-induced hydrothermal activity on early Mars, Journal of Geophysical Research, 110, 2005.

[3] Abramov O. and Kring D.A.: Numerical modeling of impact-induced hydrothermal activity at the Chicxulub crater. Meteoritics & Planetary Science 42; 1, 93–112, 2007.

[4] Hayba D.O. and Ingebritsen S.E.: The computer model HYDROTHERM, a three-dimensional finite-difference model to simulate ground-water flow and heat transport in the temperature range of 0 to 1,200 degrees Celsius. U.S. Geological Survey Water-Resources Investigations Report 94-4045. Reston, Virginia: U.S. Geological Survey. 85 p. 1994.

[5] Hayba D.O. and Ingebritsen S.E.: Multiphase groundwater flow near cooling plutons. Journal of Geophysical Research 102: 12,235–12,252, 1997.

[6] Kring D. A.: Impact events and their effect on the origin, evolution, and distribution of life. GSA Today 10:1–7, 2000.

[7] Naumov M. V.: Impact-generated hydrothermal systems: Data from Popigai, Kara, and Puchezh-Katunki impact structures, In Impacts in Precambrian shields, edited by Plado J. and Pesonen L. J. New York: Springer. pp. 117–171., 2002.

[8] Rathbun J. A. and Squyres S. W. 2002. Hydrothermal systems associated with Martian impact craters. Icarus 157:362–372.

EPSC Abstracts
Vol. 12, EPSC2018-1248, 2018
European Planetary Science Congress 2018

Impactor material in new lunar meteorite NWA 10989

Zoe Morland, Katherine Joy
School of Earth and Environmental Sciences, University of Manchester, Williamson Building, Oxford Road, Manchester, M13 9PL, UK. (**zoe.morland@hotmail.co.uk**, Katherine.joy@manchester.ac.uk)

1. Introduction

Lunar meteorites derive from material ejected at escape velocity from impact events on the Moon. The ejected material is subsequently caught by Earth's gravitational field and falls as a meteorite [1].

Analysis of lunar meteorites improves understanding of the whole surface of the Moon, not just areas visited by the Apollo missions [2]. Moreover, they unlock crucial insight into dynamical processes that have affected the inner Solar System [3]. Despite recent investigation, the impact flux and composition of impactor material delivered to the inner Solar System throughout history still remains mysterious [4]. A key time period still yet to be fully understood is the basin forming epoch. Preserved meteoritic material in lunar samples constitute a vital resource to answer these outstanding questions [5]. Here we investigate these records in a newly discovered lunar meteorite.

2. Samples and Methods

North West Africa (NWA) 10989 is a lunar regolith breccia, which means it formed within a few meters of the lunar surface, in a region highly affected by impact reprocessing. It represents the fusion of an ancient regolith soil that was composed of highland and/or mare rocks. The 1 cm sized fragment of NWA 10989 we investigated specifically contains highland granulites, glassy impact melt breccias (GIMBs), clastic impact melt breccias (CIMBs), monomineralic pyroxene and mare basalt within a clastic glassy matrix that includes impact melt spherules and Fe-Ni metal which are indicative regolith components. The Fe-Ni metal is dominantly contained within a single 1.90 × 0.85 mm grain along with several other smaller grains and abundant fine particles in the matrix (Fig. 1a).

At the University of Manchester, the following instruments were used to investigate the sample's mineralogy and chemistry: EDAX environmental scanning electron microscope to obtain close-up back scattered electron (BSE) and whole sample BSE merger images, qualitative compositional energy-dispersive X-ray spectroscopy point spectra and whole sample elemental map; Raman spectrometer to identify cohenite and goethite; and electron probe micro-analyzer to quantitatively measure major element concentrations.

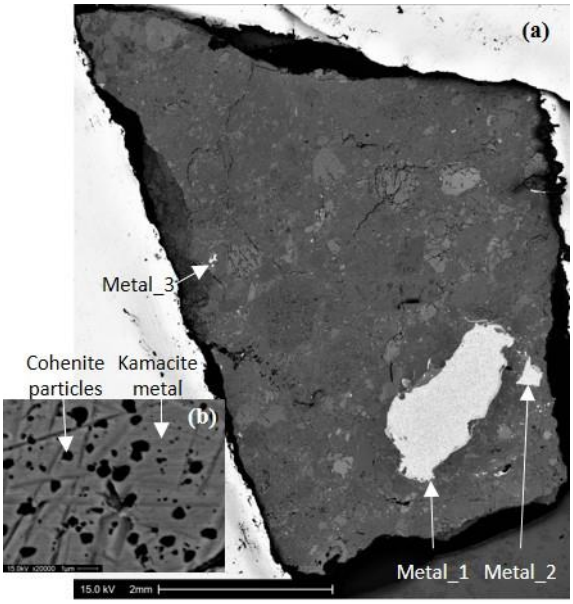

Figure 1: (a) Whole sample BSE image – metallic grains clearly distinguishable as white grains. (b) close-up BSE image of carbon particles found consistently throughout all Fe-Ni metal in the sample.

3. Results and Discussion

Quantitative analysis has confirmed that the metallic grain is composed of predominantly kamacite (low-Ni) with minor amounts of taenitic (high-Ni) material and K-rich schreibersite (Fig. 2a). Comparing the composition of this metal to the meteoritic field (Fig. 2a) suggests that the metal was delivered to the Moon as a meteorite [6]. However, the silicates (olivine, pyroxene and plagioclase) surrounding the metal fragment reflect endogenous lunar compositions (Fig. 2b). The texture and compositional difference between silicates and metal suggest that the

meteoritic metal has undergone multiple stages of reprocessing, reheating and recrystallisation since impacting the lunar surface.

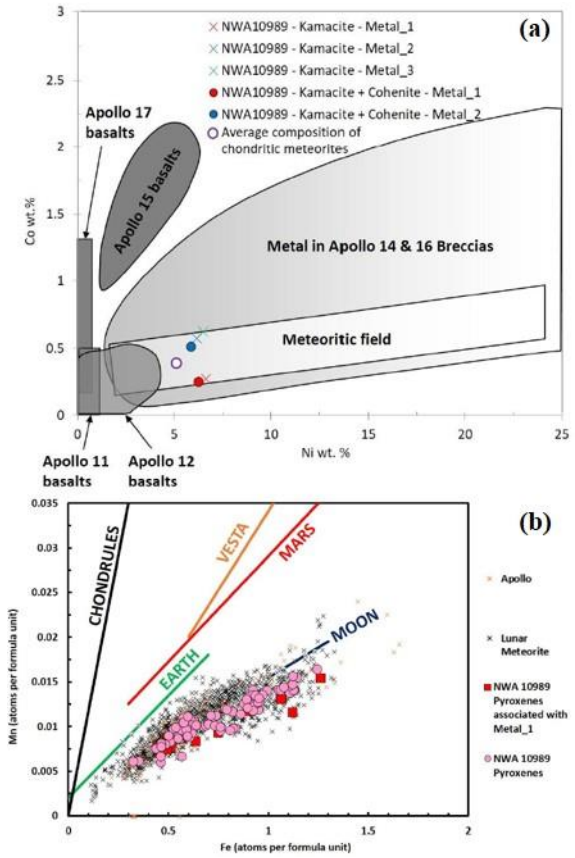

Figure 2: (a) NWA 10989 metallic grain plotting within the meteoritic field, (b) pyroxene grains in contact with the metallic grain showing native lunar composition rather than meteoritic.

Carbon particles were identified across all Fe-Ni metal within this sample (Fig. 1b). Raman analysis lead to identifying them as cohenite. Their presence in the Fe-Ni metal and not softer phases such as troilite, suggest they are not a polishing artefact.

Further 3D analysis of the metal grains is underway to possibly reconstruct the shock, pressure and temperature deformation history of the metal grains. Moreover, it aims to discern whether carbon particles, thought to be cohenite, are intrinsic to the metal. If so, they may provide important information indicative of source material and mechanism and conditions of crystallization. Results from this analysis will enable more accurate and informative inferences to be made about the conditions of formation of this regolith breccia. The source material of the meteoritic metal will be explored in more detail, providing insight into the materials delivered to the Moon at different times in its history [4] and hence the dynamical processes that have affected the inner Solar System [7]. Study of this material will improve our understanding of the nature and budgets of lunar metal in the lunar regolith. This will aid in forthcoming assessments of the Moon's potential as a resource [8], which is important for future lunar exploration plans and *in situ* resource utilization (ISRU) of the lunar surface.

Acknowledgements

Thank you, Martin Goff, for donating the sample.

References

[1] Korotev, R. L.: Lunar geochemistry as told by lunar meteorites, Chemie der Erde – Geochemistry, Vol. 65(4), pp. 297-346, 2005.

[2] Jolliff, B. L., Gillis, J. J., Haskin, L. A., Korotev, R. L., Wieczorek, M. A.: Major lunar crustal terranes: Surface expressions and crust - mantle origins, J. Geophys. Res, Vol. 105, pp. 4197-4216, 2000.

[3] Calzada-Diaz, A., Joy, K. H., Crawford, I. A. and Nordheim, T. A.: Constraining the source regions of lunar meteorites using orbital geochemical data, Meteoritics & Planetary Science, Vol. 50, pp. 214-228, 2015.

[4] Hartmann, W. K., Ryder, G., Dones, L. and Grinspoon, D.: Origin of the Earth and Moon. In: R. Canup & K. Righter, eds. Tuscon: University of Arizona Press, pp. 805-826, 2000.

[5] Joy, K. H., Zolensky, M. E., Nagashima, K., Huss, G. R., Ross, D. K., McKay, D. S., and Kring, D. A.: Direct Detection of Projectile Relics from the End of the Lunar Basin–Forming Epoch, Science Express. 2012.

[6] Goldstein, J. I. and Yakowitz, H., Metallic inclusions and metal particles in the Apollo 12 lunar soils, Proceedings of the Lunar Science Conference II, 11-14 January 1971, Houston, M.I.T Press, Vol. 2, pp. 177-191, 1971.

[7] Joy, K. H., Crawford, I. A., Curran, N. M., Zolensky, M., Fagan, A. F., and Kring, D. A.: The Moon: An Archive of Small Body Migration in the Solar System, Earth Moon Planets, Vol. 118, pp. 133-158, 2016.

[8] Crawford, I. A.: Lunar resources: A review, Progress in Physical Geography, Vol. 39(2), pp. 137-167, 2015.